UNIVERSITY COLLEGE LONDON

Department of Medical Physics and Biomedical Engineering

Doctorate Programme in Medical Physics

Multimodality characterization of tissue microstructure with Magnetic Resonance and Optical Spectroscopy

First Supervisor: Dr Adam P. Gibson

Second Supervisor: Prof Daniel C. Alexander

Ph.D. thesis of:

Alessandro Proverbio

2016

I, Alessandro Proverbio confirm that the work presented in this thesis is my own. Where information has been derived from other sources, I confirm that this has been indicated in the thesis.

Abstract

Cancer introduces changes in the microstructure of tissues, and different modalities can characterise specific features. Diffusion Magnetic Resonance investigates the diffusion of water molecules within the microstructure, providing contrast to describe the confinement of water in the different cytological compartments. The migration of photons and their polarisation status in a medium is conditioned by scattering and absorption where scattering is related to the micro and nanostructure. For the first time, we demonstrate the use of two modalities to inform a combined model describing microstructural features non-invasively. Diffusion MR and Optical Spectroscopy provide complementary information about the tissue, and a common model can be used to provide bio-markers indicating presence and staging a cancerous lesion. Here, the common model is fitted to the signals from each modality to inform a collective characterisation of the microstructure. A proof of concept on a sample (oil in water emulsion) is proposed to test the approach, where time-domain optical spectra have been combined with diffusion NMR echoes. To demonstrate the first steps towards clinical feasibility, a diffusion MR imaging, based on Oscillating Gradient Spin Echoes (OGSE), has been implemented to investigate the smallest elements of the microstructure of fixed samples obtained from two human colorectal cell lines. Diffusion OGSE MR imaging was then combined with polarised light spectroscopy. The ultimate aim is to provide an implementable method for clinical practice, where the optical modality can be acquired in gastroscopy, independently from the MRI imaging. The target is to diagnose colorectal cancer and stage the grade non-invasively. Furthermore, this work provides a method that can be extended to other modalities with minor changes.

Contents

List of Tables

List of Figures

Publications

Journal articles

"Multimodality characterization of microstructure by the combination of diffusion NMR and time-domain diffuse optical data"; A. Proverbio, B.M. Siow, M.F. Lythgoe , A.P. Gibson, D.C. Alexander; Physics in Medicine and Biology, 59.11 (2014): 2639.

Conference proceedings

"Multimodality investigation of microstructures by the combination of diffusion NMR and diffuse optical spectroscopy "; A. Proverbio, B. Siow, A. Gibson, D. Alexander; International Society for Magnetic Resonance in Medicine Meeting, Salt Lake City 2013.

"Multimodality characterization of microstructure by the combination of diffusion NMR and time domain diffuse scattering spectroscopy"; A. Proverbio, B. Siow, A. Gibson, D. Alexander; International Conference in Magnetic Resonance Microscopy, Cambridge 2013.

"Combined diffuse scatter spectroscopy and diffusion NMR for quantitative characterization of microstructure"; A. Proverbio, B. Siow, D. Alexander, J. Hebden, A. Gibson; Optical Society of America, (pp. BT3A-40), 2014.

"Mathematical models of colorectal tumour microstructure informed by oscillating gradients diffusion MRI", A. Proverbio, B.M. Siow, E. Panagiotaki, S. Walker-Samuel, M.F. Lythgoe, A.P. Gibson, D.C. Alexander; International Society for Magnetic Resonance in Medicine Meeting, Milano 2014.

List of acronyms

ADC	Apparent Diffusion Coefficient
BIC	Bayesian Information Criterion
CABI	Centre for Advanced Biomedical Imaging
CCD	Charge Coupled Device
CLSM	Confocal Laser Scanning Microscopy
CW-OGSE	Cosine Wave Oscillating Gradient Spin Echo
DA	Diffusion Approximation
DDCOSY	Diffusion-Diffusion Correlation Spectroscopy
DEXSY	Diffusion-Diffusion Exchange Spectroscopy
DKI	Diffusion Kurtosis Imaging
dMRI	Diffusion Magnetic Resonance Imaging
dNMR	Diffusion Nuclear Magnetic Resonance
DOS	Diffuse Optical Spectroscopy
DOT	Diffuse Optical Tomography
dPGSE	Double PGSE
DSS	Diffuse Scattering Spectroscopy
DTI	Diffusion Tensor Imaging
DW-MRI	Diffusion Weighted Magnetic Resonance Imaging
ECG	Electrocardiogram
EEG	Electroencephalography
EPI	Echo Planar Imaging
FA	Fractional Anisotropy
fMRI	Functional Magnetic Resonance Imaging
FOV	Field of View
GPD	Gaussian Phase Diffusion
H-G	Henyey–Greenstein
L-M	Levenberg–Marquardt
LSS	Laser Scattering Spectroscopy
MCMC	Monte Carlo Markov Chain
MD	Mean Diffusivity
MRE	Magnetic Resonance Elastography

MRI	Magnetic Resonance Imaging
MSE	Mean Square Error
MT	Mie Theory
NA	Numerical Aperture
NIR	Near Infrared
O/W	Oil in Water
OGSE	Oscillating Gradient Spin Echo
PBS	Phosphate Buffet Solution
PDF	Probability Distribution Function
PGSE	Pulsed Gradient Spin Echo
PMT	Photon Multiplier Tube
RF	Radio Frequency
RTE	Radiative Transfer Equation
SE	Stimulated Echo
SNR	Signal Noise Ratio
SW-OGSE	Square Wave Oscillating Gradient Spin Echo
TPSF	Temporal Point Spread Function
US	Ultrasound Imaging
vis-NIR	visible-near infrared
W/O	Water in Oil

List of symbols

Γ_n	Coefficients representing the contribution of the gradient waveform to the diffusion MRI signal
Δ	Diffusion time, time for spin diffusion in a diffusion MRI sequence
Φ	Fluence in the Radiative Transfer Equation
Ω	Solid angle (generally is an integration variable)
γ	Gyromagnetic ratio
δ	Duration of the gradient pulse in a diffusion MRI sequence
λ	Wavelength of an electromagnetic wave
μ_a	Optical absorption coefficient
μ_t	Optical extinction coefficient
μ_s	Optical scattering coefficient
$\mu_{s,event}$	Optical scattering coefficient related to one particle per unit volume
μ'_s	Optical apparent scattering coefficient
ψ	Volume fraction
σ	Spread of the distribution of size of the particles intended as its standard deviation
σ_{abs}	Optical absorption cross-section
σ_{sca}	Optical scattering cross-section
θ	Angle (generally is an integration variable)
ω	Angular velocity of the electromagnetic wave
ADC	Diffusion MRI apparent diffusion coefficient
$\mathbf{B}$	Vector representing the magnetic field
(B_n, λ_n)	Coefficients describing the contribution of the microstructure to the diffusion MRI signal
C_{EXP}	Experimental spectroscopic optical signal
$\bar{D}$	Diffusion MRI diffusion tensor
D	Diffusion coefficient of diffusion MRI spins
D_{cyt}	Diffusion coefficient in the cytoplasm
D_{ext}	Diffusion coefficient in the extracellular components of diffu-

	sion MRI spins
D_{nuc}	Diffusion coefficient in the nuclei of diffusion MRI spins
D_{Sph}	Diffusion coefficient in the sphere compartment of diffusion MRI spins
D_A	Optical diffusion coefficient
$\mathbf{E}$	Vector representing the electric field
E_0	Magnitude of the electric field
E_{phot}	Energy of a photon
E_xE_x	Horizontal and vertical components of the electric field
FA	Diffusion MRI fractional anisotropy
G	Diffusion MRI gradient intensity
$I_\parallel$	Intensity of light polarised parallel to the reference system
$I_\perp$	Intensity of light polarised orthogonal to the reference system
$\mathbf{J}$	Light energy flux in the Radiative Transfer Equation
L	Radiance in the Radiative Transfer Equation
$\mathbf{M}$	Vector representing the nuclear magnetisation
M_{DOS}	Model generating the synthetic optical signal for the Diffuse Optical Spectroscopy
M_{DSS}	Model generating the synthetic optical signal for the Diffuse Scattering Spectroscopy
M_{LSS}	Model generating the synthetic optical signal for the Laser Scattering Spectroscopy
MD	Diffusion MRI mean diffusivity
N_0	Number of particles per volume unit
P	Phase function in the Radiative Transfer Equation
R	Radius of the cell membrane in the geometrical model
R_I	Ratio between the intensity of backscattered and incident light
S_1 S_2 S_3 S_4	Components of the Jones matrix which are related to Mie theory
S_{Ball}	Diffusion MRI signal generated by a model with a *ball* compartment
S_{Bi-Exp}	Diffusion MRI signal generated by a model with two *mono-*

	exponential compartments
S_{dSph}	Diffusion MRI signal generated by a model with a compartment with a *distribution of spheres*
$S_{dSph+Ball}$	Diffusion MRI signal generated by a model with a *distribution of spheres* and a *ball* compartments
S_{DT}	Diffusion MRI signal generated by a model according to a *diffusion tensor*
S_E	Source term in the Radiative Transfer Equation
S_{EXP}	Diffusion MRI signal measured in the experiments
$S_{She+Sph+Ball}$	Diffusion MRI signal generated by a model with *shell*, *sphere* and *ball* compartments
$S_{Sph+Ball}$	Diffusion MRI signal generated by a model with two *sphere* and one *ball* compartments
$S_{Sph+Sph+Ball}$	Diffusion MRI signal generated by a model with *sphere*, *sphere* and *ball* compartments
S_{Sphere}	Diffusion MRI signal generated by a model with a *sphere* model
$S_{Tri-Exp}$	Diffusion MRI signal generated by a model with three *mono-exponential* compartments
S_{Zp}	Diffusion MRI signal generated by a model with a *zeppelin* model
T	Synthetic signal for a temporal point spread function
T_1	MRI spin-lattice relaxation time
T_2	MRI spin-spin relaxation time
T_E	Echo time in a diffusion MRI sequence
T_{EXP}	Experimental temporal point spread function for the optical signal
$\mathbf{S}$	Stokes vector
a	Particle dimension (generally indicates the integration variable, not the average size in a distribution)
b	Diffusion MRI b-value
$\mathbf{e}_x$ $\mathbf{e}_y$ $\mathbf{e}_z$	Unitary vectors in the three directions
h	Plank's constant

c	Speed of light in vacuum
f	Frequency of the oscillating gradient spin echo gradient
$\mathbf{g}$	Vector orientation for the diffusion MRI gradient
g	Optical anisotropy coefficient
g_{event}	Optical anisotropy coefficient related to a single particle per unit volume
k	Wave number
m	Refractive indexes ratio
n	Refractive index
n_{cyt}	Refractive index of the cytoplasm
n_i	Refractive index of the particle
n_m	Refractive index of the external medium
n_{nuc}	Refractive index of the nuclei
p_{DOS}	Distribution of the size of the particles in the diffuse optical spectroscopy model
p_{dNMR}	Distribution of the size of the particles in the diffusion nuclear magnetic resonance model
p_{DSS}	Distribution of the size of the particles in the diffuse scattering spectroscopy model
p_V	Distribution of the size of the particles on a volumetric average
r	Average radius of the compartment/particles in the model (including the radius of cell nuclei)
s	Slab/sample thickness
t_0	Time offset for calibration of the optical experimental signal
t_m	Mixing time for a diffusion MRI Stimulated Echo sequence
v	Speed of light in the medium
x	Mie theory shape factor
w	Weighting factor

Part I

Introduction and theoretical framework

Chapter 1

Introduction: microstructure investigation and multimodal approach in medical physics

1.1 Historical introduction

1.1.1 Microscopy, and body investigation techniques

The first and most relevant advancements were supported by microscopy techniques. The first microscopes were assembled in the XVII century, and their original applications were in botanics and general study of materials [Stewart, 2003]. Only about a century later, the first complete biological studies supported by microscopy were published [Ford, 1992].

Along with optical microscopy, other contrast mechanisms were introduced. One of the pioneering physiological investigation techniques was the Electrocardiogram (ECG), performed from the end of the XIX century. Electroencephalography (EEG), was also first applied in the same period to support and extend the advances in neurology [Swartz, 1998]. Both these techniques were a clear example of the synergetic advancement of technology and medical knowledge. Similarly, previous experiments on optical transillumination have been conducted with visible light since 1831 [Gibson and Dehghani, 2009].

The progressive interest in nanoscale features was one of the directions of research in the last century. Knowledge enabled technology advancements supported by the deeper understanding of physics. Completely novel techniques were developed such as electron microscopy [Mulvey, 1962], but also phase contrast, near field, or confocal laser microscopes were progressively introduced to address specific problems.

In the last century,the first x-ray images started to offer *in-vivo* imaging [Weber, 2001, Michette, 2003] at the beginning of the XX century. At that time, x-ray physics was recently discovered but the technique soon became a clinical practice. X-ray imaging and later developments in medical imaging have had a huge impact on clinical life.

1.1.2 First imaging techniques

Scientific and technological development have provided new opportunities and novel imaging modalities. Ultrasound imaging (US) was introduced,in 1940s, but clinical application began in 1950s [Kurjak, 2000]. Also Nuclear Magnetic Resonance dates its theoretical basis in the late 1930s [Rabi et al., 1991], and its first applications only 10 years later [Filler, 2009, Carr and Purcell, 1954, Damadian, 1971]. Starting from chemistry, it evolved with the use of different contrast mechanisms, and diffusion NMR was applied first in 1964 [Stejskal and Tanner, 1964]. In order to use this technique for clinical purposes, the spectroscopic information obtained should be reconstructed into images. Only in the 1973, the first 2D NMR image acquisition was performed, becoming Magnetic Resonance Imaging [Lauterbur, 1973]. From that time, MRI grew at impressive speed developing different techniques, moving from anatomical T1, T2, T2w, to functional BOLD and fMRI [Fass, 2008]. An additional contrast mechanism comes from Diffusion Weighted MRI (DW-MRI), where contrast comes from the observation of molecular movement in the microstructure

1.2 Why microstructure?

Disease states frequently alter the microstructure of tissue. An example is the variation of the axon lumen due to demyelination in multiple sclerosis [Lucchinetti et al., 2000], or the microstructure degeneration occurring in skin burns [Park et al., 2001]. Overall, cancer is the most widely known case of disease where different grades [Khan et al., 2003] are characterised by different packing of cells, leading to different volume occupied [Enfield and Gibson, 2012]. For example, nuclei grow with the disease, and occupy larger portions of the cell, or cells might be polynucleate [Shi and King, 2005]. Different volume fractions occupied by cells, as well as the ratio of nuclear size to cell size, are important histological bio-markers [Wittschieber et al., 2010, Frangioni, 2008]. Although histology relies primarily on the detection of genetic enzymes, microstructural investigation (using hematoxylin and eosin stain) can also provide an indication of the grade of tumours [Bloom and Richardson, 1957, Edge and Compton, 2010, Wittschieber et al., 2010]. Consequently, there a need for non-invasive histology to obtain clinically equivalent information relying only on intrinsic contrast [Enfield and Gibson, 2012].

1.3 Optics for microstructure

Optical techniques have been used for the investigation of microstructural features for centuries. Visible optical microscopes were first adopted in the 17th century, and progressive evolution changed the configuration first and the light source later. The observation of histological conditions was then improved by the use of additional contrast mechanisms, such as stainers or fluorescence. To improve the resolution, the first step was Confocal Laser Light, allowing to push at the diffraction limit and to obtain high resolutions [Spencer, 1982, Pawley, 2010]. At the same time, interferential microscopy can provide information on dense tissues in three dimensions with a penetration up to few millimetres [Spencer, 1982]. All these approaches apply to the investigation of microstructure of specific small areas of superficial layers or excised samples.

One technique used for studying microstructure is Diffuse Optical Spec-

troscopy (DOS). The microstructure modifies the optical properties (scatter and absorption) of a material and the signal obtained changes accordingly; consequently, it is possible to observe the chemical composition of a sample or the pattern of the microstructure non-invasively [Gibson and Dehghani, 2009]. The optical absorption (which depends on the different molecules), and the scattering (which depends on the configuration of such molecules or particles) introduces a contrast that can be used to inform a model. DOS provides information about thin emulsions [van Staveren et al., 1991, Chantrapornchai et al., 1999, Michels et al., 2008], food science [Lee et al., 1997, Pillonel et al., 2003, Everett and Auty, 2008], and in astronomy and meteorology [Henyey and Greenstein, 1940, Kaplan et al., 1994]. Other applications of DOS can detect the effects of pathological physiology or microstructure of the tissue, such as change of blood volume, of cytological expression, or of chromophore concentration [Gurjar et al., 2001]. The sizing of microstructural elements is more commonly implemented with polarised light where cytostructural changes in epithelial cells are observed [Schmitt and Kumar, 1998, Gurjar et al., 2001], but non-polarised light has also been used to distinguish between different typologies of microstructure [Ramachandran et al., 2007].

1.4 Diffusion MRI

A second technique able to investigate the microstructure of a sample is Magnetic Resonance Imaging (MRI), which describes certain chemical and physical properties of tissues. Diffusion MRI provides contrast by the diffusion of water molecules containing spins [Stejskal and Tanner, 1964, Callaghan and Xia, 1991]. In diffusion MRI, the mobility of spins depends on the density of barriers, the size and permeability of pores, and the intrinsic diffusivity of the medium. Thus, diffusion MRI provides sensitivity to these features of internal microstructure.

The use of DW-MRI is a marked step in the investigation of tissue microstructure. The first DW-MRI experiments began in the mid-80s [Le Bihan et al., 1985], but diffusion NMR has been adopted before in food sciences and other manufacturing applications, e.g. in the detection of different properties

of emulsions, curds and cheeses [Callaghan and Jolley, 1983, Rosenberg et al., 1992, Mahdjoub et al., 2003, Hollingsworth and Johns, 2003b, Denkova et al., 2004, Johns, 2009]. The first uses of gradients oriented in three directions leads to the identification of Apparent Diffusion Coefficient (ADC) as straightforward bio-marker. ADC has been applied to all the body with different results; nevertheless, the brain became the natural field of application [Moseley et al., 1990].

The first important correlation of MR images with the microstructure could be considered the introduction of Diffusion Tensor Imaging (DTI) [Douek et al., 1991, Basser and Pierpaoli, 1996]. This is a crucial point when the correlation of acquisition gradients and the microstructure was understood as an element describing the neuron dispersion [Assaf and Basser, 2005, Assaf et al., 2008, Assaf and Pasternak, 2008, Alexander et al., 2007, Johansen-Berg and Behrens, 2009]. It also has other major applications in medicine where it is used to detect and diagnose pathologies where histological changes occur, for example in cancer lesions [Koh and Collins, 2007], stroke [Neumann-Haefelin et al., 1999], multiple sclerosis [Werring et al., 1999], and Alzheimer's disease [Rose et al., 2000]. Recently, researchers have designed biophysical models to relate the signal to microstructural parameters of interest such as a dimension or a permeability of cellular compartment [Assaf et al., 2008, Xu et al., 2009b, Alexander et al., 2010].

Parallel to DTI, other approaches tried to detect non-Gaussian features with higher order signal [Jensen et al., 2005]. The use of multiple gradients led to ad hoc applications to obtain estimate of signal microstructure [Schachter et al., 2000, Does et al., 2003, Assaf and Basser, 2005, Shemesh et al., 2009, Panagiotaki et al., 2012, Jones et al., 2013].

1.5 Multimodality

The combination of different modalities is a new branch of biomedical imaging. The use of different sources of information increases the quality of diagnosis because it may provide different descriptions of the same problem, but it may also be a cross-validation. The most common approach in the literature is

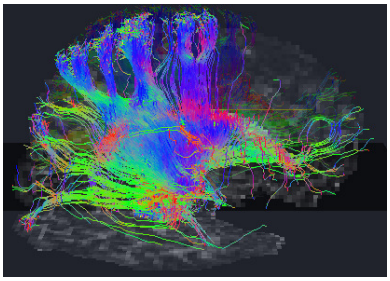

Figure 1.1: Tractography image obtained from a DTI acquisition of a middle sagittal section of a brain. The image was produced using the Basic probabilistic tractography tutorial from the Camino toolkit [Cook et al., 2006].

to compare the final results of different modalities, but here we propose the integration of different physical aspects in order to obtain advanced solutions.

Many new techniques combine elements from two physical mechanisms in order to obtain advanced tools; they are named hybrid. Hybrid modalities are not classed as multimodality imaging, but they are worth mentioning because of their innovative approach. Photoacoustics is one of them, and it combines laser light propagation and ultrasound; therefore, it is the combination which modifies the ultrasound waves and generates a new signal [Rosencwaig and Gersho, 1976]. This technique can image thin samples but with a very high resolution, and photoacoustics is a good example of the combination of two physical aspects of the sample. Another example of hybrid multimodalities is Magnetic Resonance Elastography (MRE) where ultrasound pulses excite the sample during an MRI acquisition in order to highlight the different elasticity modules inside the sample, and to obtain a map of the mechanical properties [Kruse et al., 2000].

Other authors adopted two modalities in order to have a validation between them. *Ntziachristos et al.* are an example because in their work on contrast-enhanced MRI and Diffuse Optical Tomography (DOT) in breast cancer they have compared the two results [Ntziachristos et al., 2000]. Another example is the combination of two modalities of the same technique, where T2-weighted MRI is connected to an area-based NMR spectroscopy [Kurhanewicz et al., 2002]. These works are still not properly multimodality approaches, but they are interesting co-validation methods operating with the final results of two

separate modalities.

A very interesting work is finally the combination of functional MRI (fMRI) and DOT in order to highlight and refine the map of oxy and deoxy-haemoglobin in the brain. In this work, the information obtained by the two methods is processed with a linear model in order to obtain a single result which is a map of the concentration of haemoglobin [Huppert et al., 2008].

In this work we are interested in the combination of a NIR optical approach and the diffusion NMR and MRI. The combination consists of the coupling of those two modalities that aim to describe the microstructure of the sample. Single and multiple wavelengths have been adopted to investigate homogeneous samples, while diffusion NMR and MRI are the natural extension to 3D of the spectroscopic technique.

1.6 Description of the work

The next chapters of this manuscript discuss the feasibility of the integration of Magnetic Resonance and Visible/Near Infrared Optics for the characterisation of microstructure. Section 2 presents the background, and parts two and three present the experimental work. Part two contains the first approaches to multimodality combinations on well known microstructures such as emulsions. Part three moves the attention to the application to biological tissues.

Chapter 3 presents the results obtained with the combinations of diffusion weighted nuclear magnetic resonance, and time-domain diffuse scattering signal. This chapter is extracted from the author's publication [Proverbio et al., 2014b] and describes the performances of the approach on a well known microstructure. The NMR acquisition were performed with the support of the co-author, Dr B. M. Siow, and the diffuse optical signals were obtained on the system *MONSTIR I*. The microscopy investigation performed with Confocal Laser Scanning Microscopy was executed on the system in the Department of Surgery at the Royal Free Hospital, London. This piece of work aims to exclude reconstruction issues and spatial heterogeneity by the problem, and to analyse the optimal performances of the approach.

Chapter 4 describes the effects of introducing multiple wavelengths to the

optical modality using an updated optical imaging system know as *MONSTIR II*. *MONSTIR II* can provide spectral information to be used for a fitting of the the dimension of scatterers. Measurements were performed by the author with the support of Dr R. Cooper, over a validation sample (intralipids) and the controlled emulsion used in the previous chapter. This work has been presented by the author in [Proverbio et al., 2014a].

Chapter 5 moves the first steps in the application over biological samples. Samples fixated during previous experiments performed by Dr E. Panagiotaki and Dr S. Walker-Samuel were used for MRI imaging. Acquisitions were performed with the support of Dr B.M. Siow. on the 9.4T scanner in the Centre for Advanced Biomedical Imaging. Sequences and experimental setup were prepared by the author, as well as the preparation of the samples for the scanning. The aim of this chapter is to understand the performances of signal models in providing representations of microstructural properties of the tissue by exploiting advanced sequences.

Chapter 6 describes the integration of the approach presented in chapter 5 with polarised Laser Scattering Spectroscopy (LSS). This work has been based on the measurements from chapter 5, and the optical measurements were performed on the same samples. As colorectal tumours are epithelial lesions compactly developing until the third stage, polarisation was used to filter the spectrum to isolate scattering properties connected to cell nuclei [Gurjar et al., 2001]. The experimental setup was prepared by the author with the support from Prof J. Hebden. The combination of LSS and diffusion MRI can offer a significant support to diagnosis and staging of colorectal cancer, and this section aims to provide a first characterisation of their combination.

The work aims to build up a step by step approach to the use of non-invasive histology based on the combination of different modalities.

Chapter 2

Theory and application: optical and diffusion MRI techniques in microstructure investigation

2.1 Optics

2.1.1 Optic physics

Light has famously a dual aspect, it is a particle but also a wave [Faye, 2008]. Photons are the particles responsible for light propagation, they propagate through materials and tissues, and they interact with molecules and atoms. The duality of light describes the propagation of a photon as a single particle interacting with atoms and other elementary particles, but also as the alteration of local electromagnetic field created by the presence of light and matter [Ingle and Crouch, 1988].

The electromagnetic field from light can generally be expressed as a combination of sinusoidal waves. Each component possesses a frequency, which is the primary indicator of the properties of light interaction with matter. Wavelength, λ, and energy, E_{phot}, are related through Plank's constant, h, as

$$E_{phot} = \frac{hc}{\lambda} \tag{2.1}$$

where c is the speed of light in vacuum.

Depending on the light energy and the matter in which the wave propagates, photon migration can be dominated by absorption, scattering, diffraction, refraction etc. or higher order effects. The first fundamental threshold is 100eV ($\lambda = 0.1nm$), separating ionising photons, able to alter with atoms' nuclei or orbitals, from non-ionising, permitting only elastic scattering.

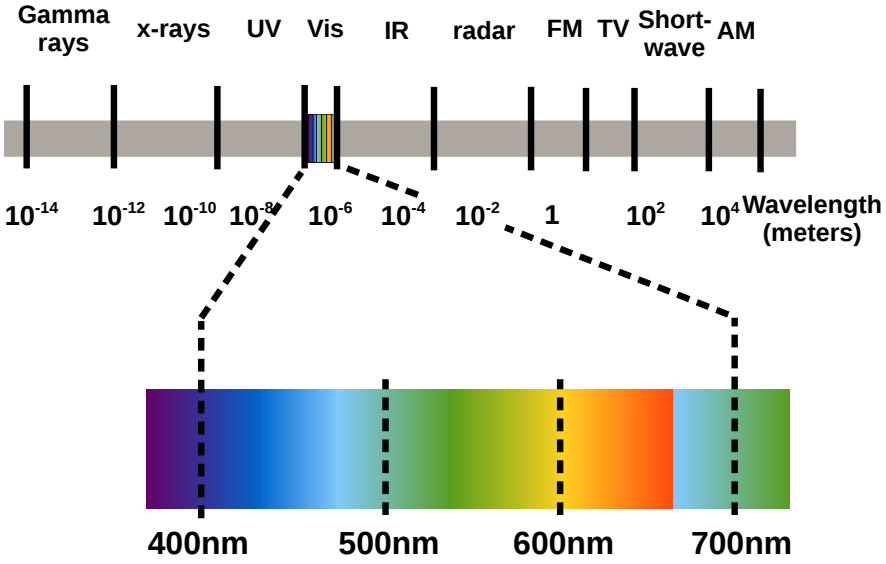

Figure 2.1: Electromagnetic spectrum. Description of the energies and wavelengths and the corresponding nomenclature.

Figure 2.1 illustrates the entire relevant electromagnetic spectrum. In the present work we will considered visible and near infrared regions (400-900 nm) where absorption, scattering, and refraction are the most important occurring phenomena.

Absorption Absorption is the most relevant physical phenomenon in visible-near infrared (vis-NIR) light. Photons migrating in the matter interact with the chemical bonds between atoms, and they are absorbed. Absorption depends on the chemical substances of the material and on the energy of the

photon which determines the ability of light to excite bonds between atoms in the same molecule. Photons are entirely absorbed as they are a quantum but the macroscopic effect results in a decrease of the total flux of light across the matter [Bohren and Huffman, 2008].Absorption is the principal contrast mechanism in vis-NIR regime.

Scattering Scattering is the change of direction of photons as a consequence of the interaction with matter. The physics of light scattering is related to intimate properties of the fundamental particles; nevertheless, macroscopic models are generally utilised. They only predict the number of scattering events per travelled distance by light, but they are generally sufficient to model the physics of macroscopic problems. In the vis-NIR, the concept of scatterer is introduced as the microscopic discontinuity in the medium causing a random change of direction to photons [Bohren and Huffman, 2008]. Scattering properties in vis-NIR depend on the ratio between wavelength and scatterer dimension. Scatterers are defined by a change of refractive index across closed boundary surfaces. The most adopted model of scattering is derived for spherical scatterers, where a solution of Maxwell's equations for the propagation of a plane wave across a sphere was described by Mie [Mie, 1908]. Mie theory is an exact solution, describing the whole spectrum, but practical approximations can be adopted when the scatterer has a dimension much smaller than the wavelength, Rayleigh elastic scattering, or geometrical optics provides solutions based on the Snell's law when the scatterer is larger and Mie solution becomes computationally inefficient.

Refraction Refraction is the change in direction of the wave vector due to a discontinuity of the medium. It is a macroscopic property, well known in geometric optics, and occurs when different refractive indexes exist. The change of wave propagation direction due to refraction is described by Snell's law as

$$\frac{sin(\theta_1)}{sin(\theta_2)} = \frac{n_2}{n_1} = \frac{v_1}{v_2} \tag{2.2}$$

where θ_1, θ_2 are the angles of the wave direction against the normal direction at the two sides of the interface, and n_1 and n_2 are the two refractive indexes. Phase velocities, v_1 and v_2, are also described by Snell's law. Phase velocities can be also intended as the local speed of light wave propagation, where $v_{vacum} = c$.

Diffraction Diffraction is the primary wave-related phenomenon observed in vis-NIR region. Diffraction occurs when the wave encounters apertures or slits of size comparable to the wavelength. It provokes a propagation varying with the dimension of the aperture, and the intensity follows a sinusoidal trend in space and time. This phenomenon is rarely considered in vis-NIR optics of turbid media as the required geometry rarely occurs in practice. Nevertheless, diffraction is fundamental as it imposes the minimum in imaging resolution as close enough small objects will be observed as unique dot. The minimum distance to distinguish two elements is expressed by the Rayleigh limit as

$$\Delta l = 2.44\lambda \tag{2.3}$$

with λ the wavelength of the radiation. This limit poses a strict limit to visible light microscopy, as smaller structures cannot be observed.

The combination of absorption, scattering, refraction and diffraction offer an accurate description of the physics of vis-NIR light in turbid media. Absorption and scattering properties are wavelength dependent and they offer a fingerprint of the material. Alternatively, the refractive index tends to offer reduced variations over vis-NIR regime as it is deeply related to the atomic aspects of the matter. Also refraction is generally not affected by wavelength. The combination of all these phenomena must be considered when photon migration is turbid media is modelled.

2.1.2 Diffuse approximation

Radiative transfer equation

The migration of photons within a turbid medium can be modelled considering the physical phenomena explained in section 2.1.1. The main contributions are scattering and absorption, and samples can be modelled as continuous at vis-NIR wavelengths if abrupt variations of optical properties do not occur [Yodh and Chance, 1995].

The classical formulation of Radiative Transfer Equation (RTE) is a balance of energy and describes the distribution of radiance, L, in time over the domain [Bohren and Huffman, 2008, Ishimaru, 1978]. Radiance is the amount of radiation passing through a surface in a specific angle (expressed in $(W/(srm^2))$). Photons are considered to have all the same energy; therefore, optical properties are identical as they are wavelength dependent only. The RTE becomes

$$\frac{1}{c}\frac{\partial L(\mathbf{r},\hat{\mathbf{s}},t)}{\partial t} = -\hat{\mathbf{s}}\cdot\nabla L(\mathbf{r},\hat{\mathbf{s}},t) - \mu_t L(\mathbf{r},\hat{\mathbf{s}},t) + \mu_s \int_{4\pi} L(\mathbf{r},\hat{\mathbf{s}},t) P(\hat{\mathbf{s}}\cdot\hat{\mathbf{s}}') d\Omega' + S_E(\mathbf{r},\hat{\mathbf{s}},t) \tag{2.4}$$

where $\mathbf{r}$ is position in the domain, $\mathbf{s}$ is a unit vector indicating a direction, t the time, Ω' the solid angle for the integration, while microscopic optical properties of material are given by the following coefficients:

- μ_s scattering coefficient indicating the number of scattering events occurring per length unit travelled by a photon. The scattering coefficient supports a macroscopic model of a microscopic phenomenon, and offers an average description of the behavior of a beam of particles.

- μ_a absorption coefficient indicates the reduction of energy flux per length unit travelled by a pack of photons.

- $\mu_t = \mu_a + \mu_s$ extinction coefficient representing the total proportion of energy flux absorbed as a combined result of scattering and absorption.

In addition to intrinsic material properties, two fundamental parameters are introduced to model external interactions:

- $P(\hat{\mathbf{s}} \cdot \hat{\mathbf{s}}')$ the phase function describing the probability of the direction of photons scattering from direction $\hat{\mathbf{s}}$ to $\hat{\mathbf{s}}'$ (see appendix A.1.2);

- $S_E(\mathbf{r}, \hat{\mathbf{s}}, t)$ the source term indicating the photons introduced in the volume in the specific point by a source.

No analytical solutions have been found for RTE so far. Computations are performed via discretisation with Finite Elements or Discrete Differences [Schweiger et al., 1995, Yang and Liou, 1996, Arridge, 1995b, Gao and Zhao, 2010]. Different software products are available, but the development of homemade code is also common for photon migration [Wang et al., 1995]. Along with deterministic algorithms, Monte Carlo approaches offer accurate and fast simulations particularly when exploiting GPU technology [Fang and Boas, 2009].

Diffusion approximation

Analytical solutions of RTE can be obtained by introducing the Diffusion Approximation (DA). DA is based on the concept that photons diffuse without a predominant direction as the highly scattering medium randomises the flux of energy before the effect of absorption become relevant [Tarvainen, 2006, Wright et al., 2006]. As a direct consequence, DA holds only when the apparent scattering coefficient $\mu_s' = (1 - g)\mu_s \gg \mu_a$ where g is the anisotropy coefficient described in appendix A.1.2. To obtain an approximation of equation 2.4, a hierarchical decomposition of the solution in spherical harmonics as

$$L(\mathbf{r}, \hat{\mathbf{s}}, t) \approx \sum_{n=0}^{1} \sum_{n=-m}^{m} H_{n,m}(\mathbf{r}, t) Y_{n,m}(\hat{\mathbf{s}}) \tag{2.5}$$

is introduced where $H_{n,m}$ are coefficients and $Y_{n,m}$ are spherical harmonics.

Two physical parameters arise from the DA model. The fluence is the amount of energy propagating in all the directions and it is obtained as

$$\Phi(\mathbf{r}, t) = \int_{4\pi} L(\mathbf{r}, \hat{\mathbf{s}}, t) d\Omega \tag{2.6}$$

where Ω is the solid angle. The energy flux is

$$\mathbf{J}(\mathbf{r},t) = \int_{4\pi} \hat{\mathbf{s}} L(\mathbf{r},\hat{\mathbf{s}},t) d\Omega \tag{2.7}$$

and it represents the propagation of energy in a specific direction [Tarvainen, 2006, Ishimaru, 1978, Bohren and Huffman, 2008].

If we substitute equation 2.5 into equation 2.4, solutions of different orders for each polynomial of the basis are obtained. By substituting the zero solution in the first order we have the linear equation

$$\frac{\partial \mathbf{J}(\mathbf{r},t)}{c\partial t} + (\mu_a + \mu_s')J(\mathbf{r},t) + \frac{1}{3}\nabla\Phi(\mathbf{r},t) = 0. \tag{2.8}$$

If we assume that transport over the scale of the mean free path is negligible, and that the fluence can be modelled by the Fick's law [Tarvainen, 2006, Ishimaru, 1978, Bohren and Huffman, 2008], we obtain

$$\frac{\partial \Phi(\mathbf{r},t)}{c\partial t} + \mu_a \Phi(\mathbf{r},t) - \nabla \cdot [D_A \nabla \Phi(\mathbf{r},t)] = S(\mathbf{r},t) \tag{2.9}$$

where we define the diffusion coefficient as

$$D_A = \frac{1}{3(\mu_a + \mu_s')}. \tag{2.10}$$

The main consequences of a diffuse approximation reside in the exclusion of anisotropy from scattering events. The medium is highly scattering; therefore, photons go through enough scattering events and lose any memory of anisotropy before suffering of absorption. This hypothesis is easily verified in biological tissues where the microstructure offers refractive index discontinuities leading to high scattering coefficients, μ_s' [Gibson et al., 2005].

Solutions of diffuse approximation

Introducing the diffuse approximation leads to an analytical description of photon migration in simple problems. Equation 2.9 can be rearranged in the frequency domain and be eventually expanded to address spectral problems

[Patterson et al., 1989, Martelli et al., 1997, Fantini et al., 1994]. All spatial, temporal, and spectral aspects can be equally described using the diffusion approximation, but in this work we concentrated on spatial-temporal problems. Two important solutions should be mentioned above all:

- Time-domain propagation in an infinite slab;
- Spatial distribution of light in a semi-infinite plane.

Many different solutions are available at the moment [Ishimaru, 1978]. The most common is the migration of photons generated from a point source in an infinite volume. Starting from this solution, the introduction of boundary conditions enables the description of finite volumes such as semi-planes or infinite slabs. The introduction of the time variable requires a different approach from standard intensity-based solution of equation 2.9.

Time-domain propagation in an infinite slab The basic case involving a Temporal Point Spread Function (TPSF) characterisation is a geometry with a point source on the surface of an infinite homogeneous slab. The two variations are transillumination and backscattering, but the solution maintains the same functional form as the differences reside in the boundary conditions only [Contini et al., 1997, Martelli et al., 1997, Arridge, 1995b].

An analytical expression of the TPSF, $T(t, t_0; \mu_s', \mu_a, n)$, is given by Patterson *et al.* (1989) and improved by Patterson *et al.* (1989) and Martelli *et al.* (1997). The analytical solution depends on the refractive index, n, on the apparent scattering, μ_s', and absorption, μ_a, coefficients, on the offset time, t_0, used for calibration of the experimental signal, and on the time of observation (t) [Contini et al., 1997] as

$$\begin{aligned} T(t, t_0; \mu_s', \mu_a, n) = & \frac{\exp\left(-\mu_a v(t-t_0)/n\right)}{2(4\pi K v)^{3/2}((t-t_0)/n)^{5/2}} \\ & \times \sum_{m=-\infty}^{\infty} \left[z_{1,m} \exp\left(-\frac{z_{1,m}^2}{4Kv(t-t_0)/n} \right) \right] \\ & - \sum_{m=-\infty}^{\infty} \left[z_{2,m} \exp\left(-\frac{z_{2,m}^2}{4Kv(t-t_0)/n} \right) \right]; \end{aligned} \tag{2.11}$$

with $K = 1/(3(\mu'_s + \mu_a))$, v is the speed of light in the medium, $z_0 = 1/\mu'_s$, $z_e = 2K$, s is the slab thickness, and t_0 is the offset time used for calibration of the experimental signal [Contini et al., 1997]. The case of backscattered light uses the coefficients

$$\begin{aligned} z_{1,m} &= s(1-2m) - 4mz_e - z_0; \\ z_{2,m} &= s(1-2m) - (4m-2)z_e + z_0; \end{aligned} \tag{2.12}$$

while the transmission

$$\begin{aligned} z_{1,m} &= -2ms - 4mz_e - z_0; \\ z_{2,m} &= -2ms - (4m-2)z_e + z_0. \end{aligned} \tag{2.13}$$

A representation of the problem modelled by equation 2.11 and a description of the physical parameters is presented in figure 2.2.

Equation 2.11 is valid for a pencil-shaped source and detector, and this model has been extended [Contini et al., 1997] so that a finite detector can be modelled instead of a point detector. The refractive index is fixed *a-priori*, and only the absorption and scattering coefficients are fitted.

Spatial distribution of light in a semi-infinite plane The other fundamental solution models the distribution of light fluence emitted by a pencil beam in a backscattering geometry. This solution is the integration over time of equation 2.11 and leads to the dependence to the distance, r only. The solution offers a profile of intensity, R_I, corresponding to the ratio between the initial energy and the backscattered as

$$\begin{aligned} R_I(\mu'_s(\lambda), \mu_a(\lambda), \rho) &= \\ &= \frac{\mu'_s}{4\pi(\mu'_s + \mu_a)} \left[z_0 \left(\mu_{eff} + \frac{1}{r_1} \right) \frac{\exp(-\mu_{eff} r_1}{r_1^2} \right] \\ &+ (z_0 + 2z_b) \left(\mu_{eff} + \frac{1}{r_2} \right) \frac{\exp(-\mu_{eff} r_2}{r_2^2} \end{aligned} \tag{2.14}$$

where $\mu_{eff} = \sqrt{3\mu_a(\mu_a + \mu'_s)}$, $z_0 = (\mu_a + \mu'_s)^{1/2}$, r_1 and r_2 are distances from the sources in two orthogonal directions, and $z_b = 2AD_A$ [Lin et al., 1997, Fishkin

and Gratton, 1993,Nachabé et al., 2010]. The parameter D_A has been defined in equation 2.10, while A is a coefficient depending on the refractive index of the slab and on the angle of incident radiation [Contini et al., 1997].

2.1.3 Effect of microstructure on light propagation

Mie theory

Research on photon migration has been focused on macroscopic propagation of light. Interactions of light with the microstructure are commonly summarised by the coefficients described in section 2.1.2, but Maxwell's equations can describe the electromagnetic field within the microstructure. Different solutions have been proposed to model light interaction with simple microstructural geometries.

Different models can describe light microstructure interaction. The Mie

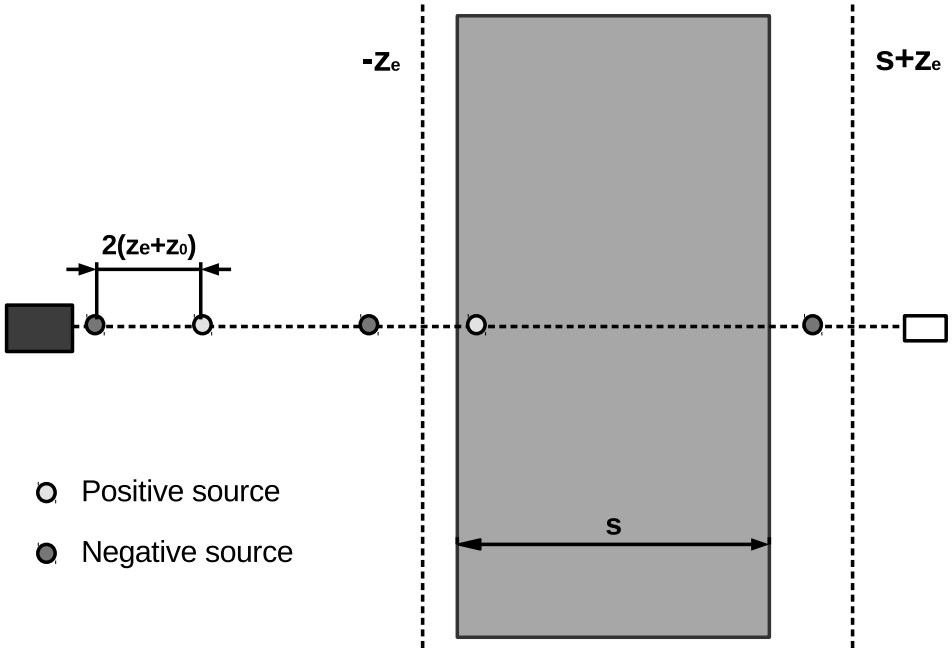

Figure 2.2: Representation of the physical problem resolved in equation 2.11. A slab of turbid medium of thickness s is shined by a point source and light is observed by a point detector. The position of the other parameters contained in the equation are also shown.

Theory (MT) is an analytical solution of Maxwell's equations for spheroidal particles in spherical and cylindrical coordinates [Mie, 1908, Ishimaru, 1978], but Rayleigh approximation provides a valid model under certain conditions [Rayleigh, 1899]. The parameter defining the best model is the shape factor

$$x = \frac{2\pi a}{\lambda} \tag{2.15}$$

where a indicates the diameter of the particle of interest, and λ the wavelength of the radiation in the medium. Wavelength in the medium is $\lambda = n_m \lambda_0$ where n_m is the refractive index in the medium and λ_0 the wavelength in the void [Rayleigh, 1899, Mie, 1908, Ishimaru, 1978, Graaff et al., 1992].

The Mie theory can relate the microstructure of a sample to the optical scattering, σ_{sca} and absorption, σ_{abs}, cross sections, and to the anisotropy coefficient, g. The MT is an exact solution of Maxwell's equations for the electromagnetic field around an isolated spherical bead with radius, a, and offers information on a single scattering event only [Ishimaru, 1978, Wiscombe, 1980]. Using the cross sections we can define an event scattering coefficient, $\mu_{s,event}$, and an anisotropy coefficient g_{event}. The coefficients are a function of the ratio of internal and dispersion medium refractive indexes (n_i and n_m respectively), and the shape factor, x presented in equation 2.15.

The Mie theory approach to Maxwell's equations solution is numerically efficient at wavelengths close to the size of the particle. For $x \gg 1$ geometric optics provides accurate solutions as the surfaces presenting refractive index changes can be explicitly modelled. Mie computations also require a large number of coefficients of the series representing the solution when the size parameters increases. For $1 \gg x$ Rayleigh approximation is more appropriate as very few terms are required for the solution [Rust and Donnelly, 2001].

Optical parameters

Optical parameters discussed in section 2.1.2 are obtained both experimentally or by averaging the expected microscopic models over a finite volume [Johns et al., 2005]. Both scattering and absorption coefficients can be obtained starting from Mie theory, by considering the number of particles per unit

volume.

The core parameters are the scattering and absorption cross-sections, σ_{sca} and σ_{abs}. Cross-sections represent the properties related to the geometry and optical properties only, they are non-dimensional and they are scaled to model the actual dimension of the microstructure (see Appendix A.1.1 for more details). The value of scattering coefficient becomes

$$\mu_s = N_0 \pi a^2 \sigma_{sca}(a, \lambda) \tag{2.16}$$

where N_0 is the number of scatterers per volume unit, while a is the radius of the scatterer and πa^2 is geometric cross-section specific to the scatterer and the wave properties [van Staveren et al., 1991]. Similarly, absorption coefficient is

$$\mu_a = N_0 \pi a^2 \sigma_{abs}(a, \lambda). \tag{2.17}$$

The presence of a population of particles with different dimensions modifies equations 2.16 and 2.17. The contributions from each dimension is accounted as

$$\mu_s = N_0 \int_0^{+\infty} \pi a^2 \sigma_{sca}(a, \lambda) p(a) \mathrm{d}a \tag{2.18}$$

with N_0 the number of particles per volume unit, and $p(a)$ a probability distribution function representing the occurrence of particle with a radius a in the population. Appendix A.2.1 describes a collection of probability distribution functions adopted in this work. Similarly, absorption properties can be estimated with the same approach.

Alternatively to equation 2.18 it is possible to extract the scattering coefficient μ_s starting from the event scattering coefficient $\mu_{s,event}$. In order to consider all the scatterers in the sample, the scattering coefficient of the whole sample becomes

$$\mu_s = \frac{3\psi}{4\pi a^3} \mu_{s,event} \tag{2.19}$$

where ψ is the volume fraction of the spheres, while the apparent scattering coefficient is $\mu_s' = \mu_s(1 - g_{event})$ where g_{event} is the anisotropy coefficient from the single event [van Staveren et al., 1991].

Absorption is a volume-related feature. Alternative approaches to equation 2.17 are based on modelling the material as a set of separate and chemically homogeneous compartments. The contribution to absorption from each chemical species is accounted as

$$\mu_a = \sum_{i=1}^{N_{comp}} \psi_i \mu_{a,i} \tag{2.20}$$

where ψ_i are the volume fractions for each of the $i = 1, ..., N_{comp}$ compartments, while $\mu_{a,i}$ are the absorption coefficients for each single compartment. This second approach is often preferred when large samples are considered as it does not involve microscopic models. When only two compartments exist, n and μ_a, can be related to microstructural properties by

$$\begin{aligned} n &= \psi n_i + (1 - \psi) n_m \\ \mu_a &= \psi \mu_{a,i} + (1 - \psi) \mu_{a,m} \end{aligned} \tag{2.21}$$

where $\mu_{a,i}$ and $\mu_{a,m}$ are the absorption coefficients of the internal compartment and of the dispersion medium.

2.1.4 Polarised light

The emerging light is characterised by a set of properties such as intensity (varying with the angle of observation, with time of flight, or with the wavelength), phase (if the beam is made of coherent light), and polarisation [Arifler et al., 2003]. All these properties could be used as a contrast mechanism to investigate the sample [Chu and Churchill, 1955, Gurjar et al., 2001, Berrocal et al., 2007]. Specifically, polarisation can be used to highlight properties not commonly detected by the human eye or standard optical instruments, and the depolarisation of a wave induced by the interaction with a material can provide information on its microstructure. The alteration of polarisation in different directions can provide additional information on anisotropy [Lie et al., 2008] or on the depth of penetration of the sample [Rehn et al., 2013, Feng et al., 2013]. Also, the size of the scatterers could affect the polarisation and be used as a contrast mechanism [Gurjar et al., 2001].

Mathematical representation of polarised waves

The polarisation of a wave could be represented by a vector, and it coincides with the electric field vector $\mathbf{E}$ in waves travelling in void. The direction of the polarisation vector could vary when the wave propagates in matter, and different polarisation modes are determined by the orientation of $\mathbf{E}$ in respect to a reference system aligned to the direction of propagation of the wave, z. Three polarisation modes are:

- Linear polarisation, when the polarisation vector sits in a plane orthogonal to z and maintains a constant direction;
- Circular polarisation, when the polarisation vector rotates with a fixed angular velocity and magnitude in a plane orthogonal to z. Clockwise is named left polarised (CLP), anti-clockwise is named right polarised (CRP);
- Elliptic polarisation, when the vector rotates as in the circular mode but presenting a variable magnitude.

The well known model for a plane wave propagating in the direction z could be adapted to represent the linear polarisation in the direction $\mathbf{e}_x$ for a wave. This would be

$$\mathbf{E}(z,t) = E_0 cos(kz - \omega t)\mathbf{e}_x \tag{2.22}$$

where k is the wave number, E_0 is the magnitude of the electric field, and ω the angular velocity depending on the wave frequency. The direction of propagation of the wave and of the polarisation remains constant in time (t) while the electric field oscillates along the direction x. Here the vector $\mathbf{e}_x$ is the unity vector in the direction x. An additional polarisation mode is circular polarisation where, for a plane-wave, it could be expressed as:

$$\mathbf{E}(z,t) = E_0(\frac{cos(kz - \omega t)}{\sqrt{2}}\mathbf{e}_x + \frac{sin(kz - \omega t)}{\sqrt{2}}\mathbf{e}_y) \tag{2.23}$$

where the polarisation rotates in the plane orthogonal to the direction of the wave z containing $\mathbf{e}_x$ and $\mathbf{e}_y$. Rotation occurs at a constant angular velocity without altering the magnitude of the electric field E_0.

An additional mode is elliptical polarisation. Similarly to circular polarisation, the polarisation vector rotates in the plane orthogonal to the direction of the propagation of the wave at a constant velocity. The magnitude of the electric field varies between two different magnitudes cyclically.

An alternative representation of the wave properties could be obtained using the Stokes vector. The idea behind this approach is to contain all the information regarding wave intensity and polarisation in a convenient format. The Stokes vector is then defined as

$$\mathbf{S} = \begin{bmatrix} I \\ Q \\ U \\ V \end{bmatrix} = \begin{bmatrix} \langle E_x E_x^* + E_y E_y^* \rangle \\ \langle E_x E_x^* - E_y E_y^* \rangle \\ \langle E_x E_y^* + E_y E_x^* \rangle \\ i\langle E_x E_y^* - E_y E_x^* \rangle \end{bmatrix}. \tag{2.24}$$

Here, the vector $\mathbf{E}$ representing the electric field is decomposed in horizontal and vertical components E_x and E_y, and the operator star (*) indicates the complex conjugate with i the imaginary unit. In this work, the factor $k/2\omega\mu$ is neglected as the alteration of the characteristics of the wave due to scattering would be independent from it.

Each of Stokes vector components has a physical direct meaning. The component I represents the intensity of the wave, Q the difference between horizontal and vertical polarisation, the component U is an indication of the inclination of the polarisation in the plane, and the last component informs about the circular polarisation component.

As a consequence, the Stokes vector could represent any state of polarisation and a few important examples are presented here. The first case is an unpolarised wave where the only non-null element is I:

$$\mathbf{S_{unpol}} = \begin{bmatrix} 1 \\ 1 \\ 0 \\ 0 \end{bmatrix} \tag{2.25}$$

Horizontal and vertical linear polarisation modes are represented as

$$\mathbf{S}_{\parallel} = \begin{bmatrix} 1 \\ 0 \\ 0 \\ 0 \end{bmatrix} \tag{2.26}$$

and

$$\mathbf{S}_{\perp} = \begin{bmatrix} 1 \\ -1 \\ 0 \\ 0 \end{bmatrix} \tag{2.27}$$

and finally, the circular polarisation is represented by a vector with a positive value of V if right handed (and negative if left handed):

$$\mathbf{S}_{\mathbf{Cyr,R}} = \begin{bmatrix} 1 \\ 0 \\ 0 \\ 1 \end{bmatrix}. \tag{2.28}$$

Polarised scattering

The interaction of a wave with matter may alter its polarisation state. The transition between one polarisation state and another could be expressed with the Muller formalism with the matricial multiplication as

$$\begin{bmatrix} I_s \\ Q_s \\ U_s \\ V_s \end{bmatrix} = \begin{bmatrix} S_{11} & S_{12} & S_{13} & S_{14} \\ S_{21} & S_{22} & S_{23} & S_{24} \\ S_{31} & S_{32} & S_{33} & S_{34} \\ S_{41} & S_{42} & S_{43} & S_{44} \end{bmatrix} \begin{bmatrix} I_i \\ Q_i \\ U_i \\ V_i \end{bmatrix} \tag{2.29}$$

where the subscript s indicates the scattered wave, the subscript i the input wave and the matrix is the Muller matrix representing the transition caused by an optical component or a scattering event. Each component of the matrix indicates the factor modifying every component of the Stokes vector as a

consequence of the scattering, including alterations of polarisation modes from one to another.

The form of the Muller matrix is dependent on the element or event to be represented. A first case reported here is the matrix representing the action of a linear polariser on the Stokes vector as:

$$M(\theta) = \frac{1}{2}\begin{bmatrix} 1 & \cos(2\theta) & \sin(2\theta) & 0 \\ \cos(2\theta) & \cos^2(2\theta) & \sin(2\theta)\cos(2\theta) & 0 \\ \sin(2\theta) & \sin(2\theta)\cos(2\theta) & \sin^2(2\theta) & 0 \\ 0 & 0 & 0 & 0 \end{bmatrix} \tag{2.30}$$

where θ is the angle of the polariser in respect to the reference system. Different positions in the angle allow to obtain horizontal, vertical or transverse polarisation modes. A more complete Muller matrix could be expressed in a generic form when scattering occurs as a consequence of the interaction with a symmetric scatterer. The Muller matrix then becomes

$$M(\alpha) = \begin{bmatrix} s_{11}(\alpha) & s_{12}(\alpha) & 0 & 0 \\ s_{12}(\alpha) & s_{11}(\alpha) & 0 & 0 \\ 0 & 0 & s_{33}(\alpha) & s_{34}(\alpha) \\ 0 & 0 & -s_{34}(\alpha) & s_{33}(\alpha) \end{bmatrix} \tag{2.31}$$

where

$$\begin{aligned} s_{11} &= \tfrac{1}{2}\left(|S_2|^2 + |S_1|^2\right) \\ s_{12} &= \tfrac{1}{2}\left(|S_2|^2 - |S_1|^2\right) \\ s_{33} &= \tfrac{1}{2}\left(S_2^* S_1 + S_2 S_1^*\right) \\ s_{34} &= -\tfrac{i}{2}\left(S_1 S_2^* - S_2 S_1^*\right) \end{aligned} \tag{2.32}$$

with S_1 and S_2 are the diagonal components of the Jones matrix described here.

A second approach is to use the Jones formalism where the mathematical representation of polarisation is generally obtained by decomposing the electric field $\mathbf{E}$, in two orthogonal components. The transition as a consequence of the

scattering with a particle is then:

$$\begin{bmatrix} E_{\parallel sca} \\ E_{\perp sca} \end{bmatrix} = \frac{exp[ik(r-z)]}{-ikr} \begin{bmatrix} S_2 & S_3 \\ S_4 & S_1 \end{bmatrix} \begin{bmatrix} E_{\parallel in} \\ E_{\perp in} \end{bmatrix} \tag{2.33}$$

The case where the scatterer is symmetric, the matrix becomes diagonal [Ishimaru, 1978]. The coefficients S_1 and S_2 can be obtained relating to Mie theory where the extinction coefficient is

$$C_{ext} = \frac{4\pi}{k^2} Re(S(0)) \tag{2.34}$$

where $S(0)$ is the value of $S_1(0) = S_2(0)$, and the value 0 indicates a direction aligned with the previously defined $\mathbf{e}_x$ [Bohren and Huffman, 2008, Schmitt et al., 1992]. Further details on Mie theory are provided in Appendix A.1.1.

Combination of polarisation modes

The ability of a wave to preserve its polarisation when travelling in a scattering medium depends on the specific polarisation mode, but also on the ratio between the wavelength and scatterer size [MacKintosh et al., 1989]. For example, the preservation of polarisation in backscattering is larger in the case of circular polarisation due to the mirroring of waves in backscattering. Conversely, linear polarisation modes appear to be more poorly preserved. When a more detailed investigation has been conducted, suggesting that the previous results are extended in terms of penetration depth, where the polarised light emerging from deeper layers maintains larger autocorrelation in circular polarisation modes [Schmitt et al., 1992]. As a consequence of such properties, a combination of light generated with one mode and detection of a different one enables the subtraction of the signals to obtain different information about the sample.

Parallel polarisation channels A first possible use of polarisation consists of the detection of only the linearly polarised light generated by a linearly polarised source in the same direction after the light has been backscattered

by the sample. Decay of parallel polarisation occurs very rapidly with the increase of depth in the material. The only light detected would be arising from superficial layers. The photons interact promptly with scatterers, and scattering events would change the direction of polarisation sufficiently to prevent detection [Schmitt et al., 1992].

Orthogonal polarisation channels A second possible use of polarisation consists of the detection of only the linearly polarised light generated by a linearly polarised source orthogonal to the first polarisation after the light has been backscattered by the sample. It requires many scattering events to have a part of the polarisation aligned to the orthogonal direction. As a consequence, the signal from the orthogonal polarisation channel is observed from the unpolarised portion of light backscattered. The amount of light detected in this modality is lower than the directly reflected light, and it gives an indication of all the scattering events from the surface to the deeper layers [Schmitt et al., 1992, Ramella-Roman et al., 2007a, Ramella-Roman et al., 2007b].

Elliptic polarisation channels The detection of elliptically polarised light from a sample backscattering which was generated by an elliptically polarised source with reverse handedness could be used to probe sample layers at different depth [Rehn et al., 2013,Feng et al., 2013]. It can also be used to probe the microstructure as with other polarisation gating techniques [Sun et al., 2013].

Combination of polarisation channels

The combination of two acquisition channels could be used to extract the information from the superficial layers only [Gurjar et al., 2001]. The spectra from each channel contain different information. The concept is that the scattering caused by a set of scatterers contained in the first sample layers would alter the polarisation differently depending on the direction.

In order to obtain a possible interpretation of the spectrum to obtain information on the microstructure of the sample we use Mie theory [Mie, 1908]. The alteration of the electric field of a wave as a consequence of the interaction

with the scatterers is described as

$$\begin{aligned} I_{\perp}(\mathbf{s}) &= \frac{|S_2(\mathbf{s},\mathbf{s}_0)|}{k^2 r^2} I_{\perp}^0(\mathbf{s}_0) \\ I_{\parallel}(\mathbf{s}) &= \frac{|S_1(\mathbf{s},\mathbf{s}_0)|}{k^2 r^2} I_{\parallel}^0(\mathbf{s}_0) \end{aligned} \tag{2.35}$$

where the superscript 0 indicates the source wave, and the subscripts $\perp$ and $\parallel$ indicate the components aligned and orthogonal to the reference system defined by the direction of polarisation of the source. The vectors $\mathbf{s}$ indicate the direction and I the intensity of incident or backscattered light. S_1 and S_2 are the components of Jones' matrix derived from Mie theory. Finally, r is the distance between sample and detector and k the wave number [Backman et al., 1999].

As a direct consequence of the previous equations, the intensity of light in the two orthogonal components can be directly calculated as

$$\begin{aligned} I_{\parallel} &= \frac{1}{k^2 r^2} \int_{\Delta\Omega} \mathrm{d}\mathbf{s} \int^{\Delta\Omega_0} \mathrm{d}\mathbf{s}_0 \mathrm{d}\mathbf{s}_0 I_0(\mathbf{s}_0) |S_2(\mathbf{s}_0,\mathbf{s}) cos\phi cos\phi_0 + S_1(\mathbf{s}_0,\mathbf{s}) sin\phi sin\phi_0| \\ I_{\perp} &= \frac{1}{k^2 r^2} \int_{\Delta\Omega} \mathrm{d}\mathbf{s} \int^{\Delta\Omega_0} \mathrm{d}\mathbf{s}_0 \mathrm{d}\mathbf{s}_0 I_0(\mathbf{s}_0) |S_2(\mathbf{s}_0,\mathbf{s}) cos\phi sin\phi_0 + S_1(\mathbf{s}_0,\mathbf{s}) sin\phi cos\phi_0| \end{aligned} \tag{2.36}$$

where Ω is the solid angle representing the range of possible directions of generated and detected light. The angles ϕ and ϕ_0 represent the change of angle of polarisation as a consequence of the scattering event [Backman et al., 1999].

For a case when the incident light is well collimated ($\Delta\Omega = 0$) the backscattered light will also be collimated. In this case the light collected will be

$$I_{\perp} - I_{\parallel} = \frac{I_0}{k^2 r^2} \int_{\pi}^{\pi-\theta_0} Re(S_1^*(\theta) S_2(\theta)) sin\theta \mathrm{d}\theta \tag{2.37}$$

with $\theta_0 = \sqrt{\Delta\Omega/\pi}$ [Backman et al., 1999]. This last equation enables us to obtain a simplified model of the system and of the geometries which are expected to be adopted for the experimental work when a collimated incident beam is

used. The two complex parameters S_1 and S_2 are generally representative of scattering events determined by the presence of particles with one single dimension. If a polydispersed ensemble of scatterers is present, it is possible to calculate an analytical solution approximating the signal representative of the entire system, or the contribution could be added together similar to what was previously done in equation 2.18 for the scattering coefficient given the distribution of dimensions $p(x)$.

2.2 Diffusion MRI

2.2.1 Physics of magnetic resonance

Bloch-Torrey equations

Electromagnetic fields are completely described by Maxwell's equations. Electric field **E**, and magnetic field, **B**, are correlated as the variation of each of the two generates the other [Ishimaru, 1978]. Despite the deep connection between the two fields, the magnetization of a two state quantum system is described by Bloch-Maxwell. The introduction of diffusion of spins generates the Bloch-Torrey equations leading to

$$\frac{\mathrm{d}\mathbf{M}}{\mathrm{d}t} = \gamma\mathbf{M} \times \mathbf{B} - \frac{M_x\hat{i} + M_y\hat{j}}{T_2} - \frac{(M_z - M_0)\hat{k}}{T_1} + \nabla \cdot \bar{D}\nabla M \tag{2.38}$$

where **M** is the nuclear magnetisation vector, γ the gyromagnetic ratio, and T_1 and T_2 are two time constants. The matrix $\bar{D}$ is the diffusion tensor, describing the diffusion of spins in the microstructure [Jones, 2011, Haacke et al., 1999].

The constant T_1 assumes a role of spin-lattice relaxation time. T_1 is the recovery time of the component of **M** aligned to the magnetic field. It represents the time required to reach the thermal equilibrium. T_1 relaxation times depend on the Larmor frequency [McRobbie et al., 2006].

The constant T_2 is the spin-spin relaxation time. It represents the decay time of the components of magnetic vector orthogonal to magnetic field. It is a complex phenomenon, but essentially is related to the fluctuations occurring

due to the excitation. T_2 is shorter than T_1, and represent an alteration of magnetic field [McRobbie et al., 2006].

The relaxation times are key properties of a material. They are related to the properties of the material only and they are key elements to discriminate between tissues.

Gradient sequences

Magnetic Resonance has been utilised to probe different interaction mechanisms between magnetic field and sample. Relaxation times described in section 2.2.1 are the first element of contrast adopted to discriminate between different tissues. All magnetic resonance techniques are based on a magnetic stimulation of the sample, and a consequent observation of the magnetisation response. Systems have been designed to apply programmable protocols.

MR systems are primarily designed to generate homogeneous magnetic fields in the sample. Magnetic fields are measured in *tesla*, and current human MRI systems can generate fields from 1.5-11.4T while NMR systems reach 30T. Magnetic field magnitude is the key element of the system, it is obtained with permanent or superconductive magnets, and it remains constant during the entire duty cycle. Secondarily, an MR system perturbates the sample via Radio-Frequency (RF) waves. Radio-frequency electromagnetic waves at the resonant (Larmor) frequency of the system excite the spins to change their magnetisation state Generally, spins are hydrogen nuclei with a gyromagnetic ratio of 42.576 MHz/T; therefore, a Larmor frequency of 400.214 MHz in a 9.4T system. Finally, MR systems introduce magnetic field spatial gradients to enable diffusion MR, and readout imaging protocols.

Magnetic Resonance techniques apply a sequence of radio frequency pulses, and gradients to characterise or image the sample. The position and duration of imaging gradients are crucial to quantify microstructural diffusion. Spins rotate accordingly to Larmor frequency; therefore, field gradient will cause to rotate at different angular velocities at different positions in the sample. The diffusion of spins within the microstructure introduces a phase shift dependent on the trajectory and on the sequence of gradients and RF pulses.

Pulsed gradient spin echo The basic sequence is the Pulsed Gradient Spin Echo (PGSE) presented in figure 2.3. PGSE consists of two gradients of intensity G and equal duration δ. The two gradients are separated by a diffusion time Δ. A first RF pulse at resonant frequency is applied to align the spins at 90 degrees. Following, diffusion is marked with a gradient while relaxation of spins occur. Consequently, a second RF pulse performs a 180 degrees rotation of spins. A second identical gradient is applied, and finally, the echo is recorded throughout a readout sequence, generally an Echo Planar Imaging (EPI).

Stimulated echo A first variation to PGSE is the Stimulated Echo (SE) shown in figure 2.3. Identical gradients are applied, but the 180 degrees RF pulse is exchanged with two 90 degrees RF pulses separated by a mixing time, t_m. The use of two 90 degrees RF avoids T_2 relaxation during the mixing time. SE is applied when short T_2 materials are examined, as this sequence allows for longer diffusion times.

Double PGSE Additional sequences have been studied over the years. Investigation of pore isotropy relies on Double PGSE (dPGSE), consisting of two PGSE gradient profiles separated by a mixing time, t_m. The gradient directions of the two parts of the sequence can be changed to probe directional micro-anisotropy of pores as well as their size [Shemesh et al., 2009]. dPGSE is also precursor to Diffusion-Diffusion Correlation Spectroscopy and Diffusion-Diffusion Exchange Spectroscopy (DDCOSY and DEXSY) which provide indications on the spin transfer between compartments [Callaghan et al., 2003].

Oscillating gradient spin echo A further extension of PGSE is the Oscillating Gradient Spin Echo (OGSE) as presented in figure 2.4. OGSE repeats a pattern of gradients multiple times to achieve a larger weighting effect, alternatively their sensitivity to detect diffusion. A first 90 degrees RF is applied at the beginning, than two pattern of gradients are applied separated by a 180 degrees RF pulses. Gradients patterns are composed of unitary lobes repeated a number N_{LOBES}, of times. OGSE are also characterised by the number of

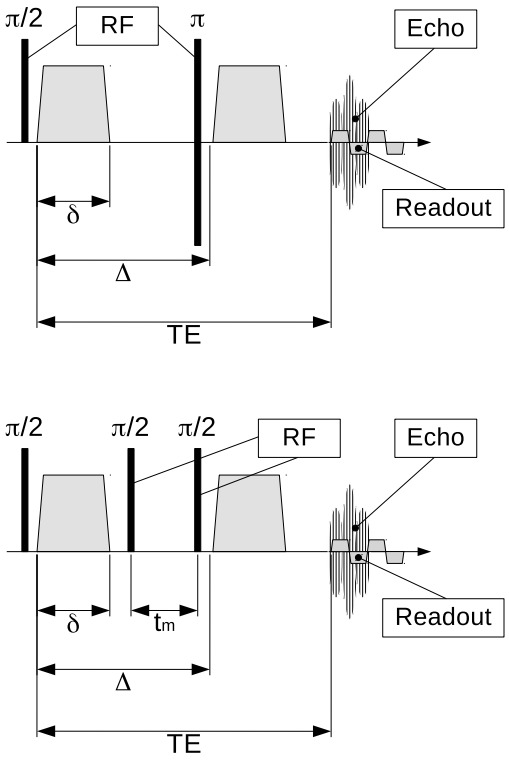

Figure 2.3: Scheme presenting a Pulsed Gradient Spin Echo sequence (top) and a Stimulated Echo (bottom). The figures show the location of RF pulses, gradients, and readout sequence.

lobes the frequency, f, at which gradients are repeated.

The profile of the gradient determines the ability of the sequence to detect the diffusion [Callaghan, 1997, Ianuş et al., 2013, Drobnjak and Alexander, 2011]. The two parts of the sequence (before and after 180 degrees RF pulse) can be symmetric or antisymmetric, and general shape of lobe is rectangular or sinusoidal. The Square Wave OGSE (SW-OGSE) is a repetition of N_{LOBES} PGSE gradients. SW-OGSE maximises the weighting factor as it uses the maximum gradient strength for all the time of application. A variation of SW-OGSE is the Trapezoid Wave OGSE, TW-OGSE, which models the slew time of the system in a mathematical modelling approach. The use of trapezoids increases complexity in the formulation of sequence mathematical representation [Ianuş et al., 2013]. Sinusoidal waves are a family of gradients where

their properties are related to the initial phase of the sinusoid. Sine and cosine OGSE offer an easier implementation as they do not suffer of slew rate limitations.

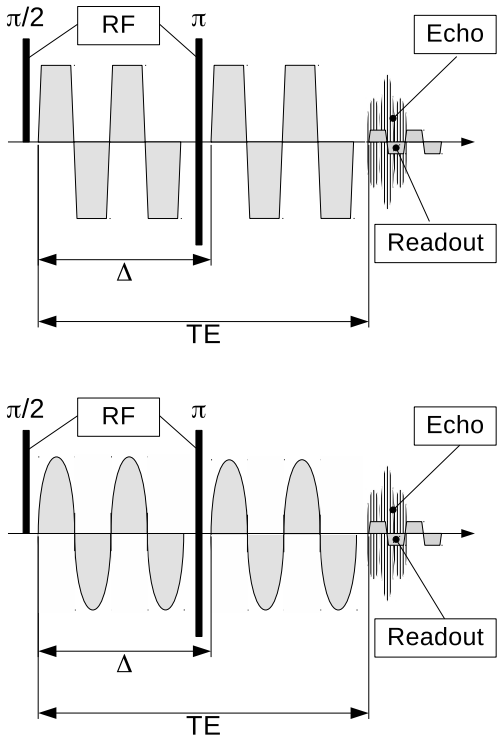

Figure 2.4: Scheme presenting a Square Wave Oscillating Gradient Spin Echo sequence (top) and a Sinusoidal Wave Oscillating Gradient Spin Echo (bottom). The figures show the location of RF pulses, gradients, and readout sequence.

Diffusion in the microstructure in biological tissues

Biological tissues are made at 70% of water. Water is a molecule with two hydrogen atoms, and one of oxygen. The hydrogen atoms are effectively one proton and one electron and the spins (H^1) are susceptible to magnetic field stimulation as equation 2.38 models. Molecules move in the microstructure within the tissue compartments, and their drifting speed, is related to the

geometry and biochemistry of the sample.

The simplest diffusion model describes molecules not constrained by any barrier. Water molecules are subject to reciprocal chemical interactions, bounds excitation induced by the temperature and these elements contribute to the characterisation of spin diffusivity. In addition to water, biological tissues contain a large variety of proteins and their diffusivity is also related to the length of their chains. All the chemical species together define the diffusion properties of spins [Chapman and Cowling, 1970]. The random movement of molecules is known as Brownian motion. Einstein's law provides a generic description of the average molecular displacement $< x >$ occurring in a time, Δ, as

$$< x^2 >= 2D\Delta \tag{2.39}$$

where D is the diffusion coefficient (expressed in m^2/s). As a matter of fact, absence of barriers and isotropy of the diffusion kernel, the propagation of molecules is equally likely in all the different directions [Miller, 1924, Chapman and Cowling, 1970].

Brownian motion is a time-homogeneous Markov process with transition probability density

$$p_\Delta(r) = (2\pi D\Delta)^{-3/2} \exp\left(-\frac{r^2}{2D\Delta}\right), \qquad \Delta \in (0, \infty) \tag{2.40}$$

where p_Δ indicates the probability of movement r in a time Δ. The Brownian motion does not have memory as it is a Markov process, and equation 2.40 is the basis for the statistical description of molecular diffusion confined by barriers which are described in section 2.2.3.

Free diffusion The signal attenuation is correlated to diffusion by equation 2.38. The most common sequence of gradients is the Pulsed Gradient Spin Echo, which has been widely adopted in clinical applications [Basser and Pierpaoli, 1996]. In the case of free diffusion, the signal attenuation becomes

$$S = S_0 \exp(-bD) \tag{2.41}$$

where the b-value, b, describes the effect of the gradient sequence while D is the diffusion coefficient, and S_0 is the reference signal. For a PGSE, the b-value becomes

$$b = \gamma^2 G^2 \delta^2 (\Delta - \delta/3) \tag{2.42}$$

where all the parameters are relative to the applied PGSE sequence [Stejskal and Tanner, 1964, Tanner, 1970].

b-value The b-value indicates the potential to introduce spin phase shift consequent to diffusion by a gradient sequence. Under the Gaussian Phase Diffusion hypothesis (GPD), b-value only depends on the gradient sequence, and it is defined as

$$b = \gamma^2 \int_0^{2\pi} \mathbf{F}^T(t')\mathbf{F}(t')\mathrm{d}t' \tag{2.43}$$

where

$$\mathbf{F}(t) = \int_0^t \mathbf{G}(t')\mathrm{d}t' \tag{2.44}$$

contains the information on the sequence of gradients G. As a matter of fact, b-value depends only by the gradient sequence and by the spin species through the gyromagnetic ratio [Douglass and McCall, 1958,Neuman, 1974,W.S. Price, 1997].

Diffusion tensor A second model of diffusion accounts for anisotropy with the introduction of a diffusion tensor $\bar{D}$. Diffusion in biological tissues is hardly isotropic, and the microstructural features tend to introduce an anisotropic diffusion of molecules. Three principal components over three principal directions can be separated, and the symmetry of the diffusion tensor $\bar{D}$, allows for six free parameters. If we describe

$$\bar{D} = \begin{bmatrix} D_x & D_{xy} & D_{xz} \\ D_{xy} & D_y & D_{yz} \\ D_{xz} & D_{yz} & D_z \end{bmatrix}, \tag{2.45}$$

the components D_x, D_y, and D_z model the diffusion along the three main axis while D_{xy}, D_{xz}, and D_{yz} describe the orientation of principal axis. When the

principal directions are aligned to the coordinate reference system, D becomes diagonal as

$$\bar{D} = \begin{bmatrix} \lambda_1 & 0 & 0 \\ 0 & \lambda_2 & 0 \\ 0 & 0 & \lambda_3 \end{bmatrix}, \tag{2.46}$$

with λ_1, λ_2, and λ_3 the diffusivity along each axis [Basser and Pierpaoli, 1996, Jones, 2011].

The two basic signal models presented in this section depend on diffusivity and gradients applied to the sample. The interaction between the mechanical movement of water molecules, and the magnetic labelling of the spins is the key contrast mechanism offered for the microstructure characterisation as an additional element contributing to the signal are the barrier to diffusion [Basser and Pierpaoli, 1996, Assaf and Basser, 2005, Alexander et al., 2007].

2.2.2 Basic diffusion models

Basic biological index

Diffusion MRI offers a large set of possible biological indicators of anatomical and physiological conditions. Biological indicators are utilised to summarise and map information contained in the signal. The simpler indicators are based on the description of change in magnitude of diffusivity coefficient or orientation of diffusion tensor.

Apparent diffusion coefficient The first index is the Apparent Diffusion Coefficient (ADC). The ADC is expressed as

$$S = S_0 \exp(-b\, ADC) \tag{2.47}$$

where b is the b-value, and S_0 the reference signal. ADC corresponds to the coefficient D in equation 2.41, but accounts for the microstructural barriers with a reduced diffusivity value [Moseley et al., 1990, Does et al., 2003].

Mean diffusivity Mean Diffusivity (MD) is the average value of diffusivity on the different directions. Starting from equation 2.46 we obtain

$$MD = \frac{\lambda_1 + \lambda_2 + \lambda_3}{3}, \tag{2.48}$$

we have the three components, λ_1, λ_2, and λ_3, of the diagonalised tensor 2.46. The mean diffusivity is an appropriate parameter when free diffusion occurs; it represents the ability of spins to diffuse due to their chemical properties. MD does not include information on the anisotropy.

Fractional anisotropy Along the mean diffusivity, the first order information about anisotropy is the Fractional Anisotropy (FA). Starting from equation 2.46 we have

$$FA = \sqrt{\frac{3}{2}} \frac{\sqrt{(\lambda_1 - \lambda)^2 + (\lambda_2 - \lambda)^2 + (\lambda_3 - \lambda)^2}}{\sqrt{\lambda_1^2 + \lambda_2^2 + \lambda_3^2}}, \tag{2.49}$$

where $\lambda = (\sum_i \lambda_i)/3$. Fractional anisotropy quantitatively indicates the presence of a preponderant diffusion direction, but does not offer information on the actual direction. FA becomes a fundamental parameter to identify specific microstructures. Finally, FA is an always positive scalar with $FA < 1$ [Basser et al., 2000].

Diffusion tensor imaging Diffusion Tensor Imaging (DTI) is the complete characterisation of tensor $\bar{D}$ for each voxel. Diffusion tensor imaging is based on multi-direction acquisition of diffusion weighted images based on PGSE. Diffusion tensor has six free parameters; therefore, at least six measures are required. Nevertheless, standard protocols contain 32, 42 or 64 measures to enable a robustness to noise. DTI provides information on the magnitude of diffusivity and on the direction of principal components of diffusion tensor [Basser and Pierpaoli, 1996, Assaf and Basser, 2005].

Higher order index Higher order indexes can be utilised to describe non-Gaussianity of molecular diffusion. Kurtosis is the fourth order statistical

momentum, and the signal with a symmetric distribution can be expressed with a Taylor series as

$$\frac{S}{S_0} = \exp\left(-bD + \frac{1}{6}b^2D^2K\right), \tag{2.50}$$

and kurtosis alights as the second order term K. This is the basis of Diffusion Kurtosis Imaging (DKI) which is a promising approach of non model specific is description of the microstructure [Jensen et al., 2011].

2.2.3 Compartments models

Tissues microstructure is a complex set of components. Previously discussed biological indicators offer a general information on the characteristics of the microstructure. Nevertheless, they do not provide accurate modelling of the signal for many problems. In order to achieve a more accurate signal model, a decomposition of the signal based on a compartment criteria has been adopted [Henkelman et al., 1994, Assaf et al., 2008, Alexander et al., 2010]. Certain techniques focus on estimating parameters describing the composition of fiber bundles, such as axon density and diameter distribution. *Stanisz et al. (1997)* proposed a three-compartment model of nervous tissue: one population of water inside elongated ellipsoidal axons, another inside spherical glial cells, and a third in the extracellular space. Fitting the full model provides estimates of all these parameters but requires a very rich data set containing low noise measurements with a wide range of diffusion times and b-values [Bihan, 1995, Stanisz et al., 1997]. A novel technique called VERDICT (Vascular, Extracellular and Restricted Diffusion for Cytometry in Tumors) was also presented to quantify and map histologic features of tumors. VERDICT couples DW-MRI to a mathematical model of tumor tissue to access features such as cell size, vascular volume fraction, intra- and extracellular volume fractions, and pseudo-diffusivity associated with blood flow [Panagiotaki et al., 2014].

The microstructure of biological tissues is considered to be divisible in intracellular and extracellular compartments. Intracellular compartments correspond to the water molecules contained in the cells while extracellular com-

partments are the remaining part of the tissue. Division occur on a signal basis rather than on a geometrical one [Assaf et al., 2008, Panagiotaki et al., 2012]. Extracellular compartments are

- Diffusion Tensor,
- Zeppelin;
- Ball (free diffusion);

while relevant intracellular compartments are:

- Sphere;
- Cylinder;
- Spherical shell.

Consequently, signal becomes a combination of the contribution from each compartments such as

$$S = \sum_i S_i \psi_i \tag{2.51}$$

where S_i are the signal from a single compartment while ψ_i are the volume fraction of each single compartment such as $\sum_i \psi_i = 1$ [Assaf et al., 2008, Panagiotaki et al., 2012].

Extracellular compartment models

Extracellular compartments are special cases of the diffusion tensor model. They are generated with the introduction of symmetries to represent an increasing level of isotropy.

Diffusion tensor The use of tensor model represents different diffusions along three arbitrary directions. Six parameters are required to characterise the tensor and define the diffusivity. The signal

$$S_{DT} = S/S_0 = \exp(-b^T \bar{D} b) \tag{2.52}$$

Waveform	Formula
PGSE	$b = G^2\gamma^2\delta^2\left(\Delta - \frac{\delta}{3}\right)$
CW-OGSE	$b = \delta\left(\frac{G\gamma}{\omega}\right)^2$
SW-OGSE	$b = \frac{G^2\gamma^2\delta}{6\nu^2} + G^2\gamma^2(\Delta - \delta)\left(\frac{1-(-1)^N}{4\nu}\right)^2$
TW-OGSE	$b = \frac{G^2\gamma^2\delta}{30\nu^2}(5 - 15t_r \cdot \nu - 5tr^2 \cdot \nu^2)$

Table 2.1: b-values formulae for PGSE, Cosine Wave OGSE, Square Wave OGSE, and Trapezoidal Wave OGSE [Stejskal and Tanner, 1964, Does et al., 2003, Ianuş et al., 2013].

where the diffusivity $\bar{D}$ is the matrix

$$\bar{D} = d_{\parallel}\mathbf{n}\mathbf{n}^T + d_{\perp_1}\mathbf{n}_{\perp_1}\mathbf{n}_{\perp_1}^T + d_{\perp_2}\mathbf{n}_{\perp_2}\mathbf{n}_{\perp_2}^T. \tag{2.53}$$

Zeppelin Zeppelin model constrains the diffusivity to be isotropic over a plane orthogonal the the first principal direction of the tensor [Alexander, 2008]. Four parameters are required in a symmetric tensor as in equation 2.52 where the signal is S_{Zp} the diffusivity $\bar{D}$ is the matrix

$$\bar{D} = \alpha\mathbf{n}\mathbf{n}^T + \beta\mathbf{I} \tag{2.54}$$

Ball The ball compartment represents an isotropic mono-exponential decay. The echo attenuation is modelled by the equation

$$S_{Ball} = S/S_0 = \exp(-b\mathbf{g}^T\bar{D}\mathbf{g}) \tag{2.55}$$

where $\bar{D} = D\mathbf{I}$ is the free diffusivity coefficient, b represents the b-value, and $\mathbf{g}$ the vector of gradient orientation. The decay model is mono-exponential, it represents the attenuation of signal due to the free diffusion of spins in a non-restricted compartment [Behrens et al., 2003]. Different b-values are reported in table 2.1 for four relevant gradient waveforms [Stejskal and Tanner, 1964, Does et al., 2003, Ianuş et al., 2013].

Intracellular compartment models

Intracellular compartments are generally represented by a restricted diffusion pattern. Impermeable barriers confine molecules within a certain space, altering the diffusion pattern. The description of signal attenuation becomes non-trivial as it requires to solve a Laplace problem [Murday and Cotts, 1968].

The signal model always depends on a kernel related to the sequence of gradients, and on a second part considering the effect of the microstructural geometry. The signal attenuation from a generic sequence is modelled as

$$S/S_0 = \exp\left(-\frac{2\gamma^2}{D^2}\sum_{n=0}^{\infty}\frac{B_n}{{\lambda_n}^2}\Gamma_n\right) \tag{2.56}$$

where the purely geometric part is $\frac{B_n}{{\lambda_n}^2}$, and the gradient waveform contribution is Γ_n. Different waveform contributions Γ_n, are reported in table 2.2 [Murday and Cotts, 1968, Xu et al., 2009b, Ianuş et al., 2013]. The geometric contributions do not depend on the waveform, and they are described in the next paragraphs.

Sphere The core intracellular compartment for the model of cancer cell lines is the diffusion confined by an impermeable sphere [Murday and Cotts, 1968]. The spherical compartment aim to capture the diffusion inside nuclei or in cells where nuclei have a negligible dimension. The attenuation model S_{Sph} is defined by two parameters, the radius, r, and the diffusivity, D, within the sphere.

$$B_n = \frac{2(r/\mu_n)^2}{\mu_n^2 - 2} \qquad \lambda_n = \left(\frac{\mu_n}{r}\right)^2, \tag{2.57}$$

where μ_n is the n–th root of $\mu J'_{3/2}(\mu) - \frac{1}{2}J_{3/2}(\mu) = 0$ with $J_{3/2}$ a Bessel function of the first kind and order 3/2 [Stepišnik, 1993, Xu et al., 2009a].

Distribution of spheres The model describing a distribution of spheres with different size is based on a weighted sum of the contributions from each dimension. The distribution of of pore radii, $p(a; r, \sigma)$, characterises the microstructure. If we say $S_{Sph}(x)$ the signal from a spherical compartment of

Waveform	Formula
Pulsed Gradient	$\Gamma_n = \{\lambda_n D\delta - 1 + e^{-\lambda_n D\Delta}(1 - cosh(\lambda_n D\delta))\}$
Cosine Wave	$\Gamma_n = \frac{G^2}{(1+\omega^2/(\lambda_n D)^2)^2}$ $\times\{\frac{{\lambda_n}^2 D^2+\omega^2}{\lambda_n D}\left[\frac{\delta}{2} + \frac{sin(2\omega\delta)}{4\omega}\right]$ $-1 + \exp(-\lambda_n D\delta)$ $+ \exp(-\lambda_n D\Delta)(1 - cosh(\lambda_n D\delta))\}$
Square Wave	$\Gamma_n = G^2\left(\frac{e^{\frac{\lambda_n D}{2\nu}}-1}{e^{\frac{\lambda_n D}{2\nu}}+1}\right)^2 (1 - N(e^{-\lambda_n D/(2\nu)} + 1)$ $-(-1)^N e^{-\lambda_n D/(2\nu)}$ $-e^{-\lambda_n D\Delta}(1 - (-1)^N cosh(\lambda_n D\delta)))$ $+\lambda_n D\delta + N\left(e^{-\frac{D\lambda_n}{2\nu}} - 1\right)$
Trapezoidal Wave	$\Gamma_n = \frac{G^2}{D^2{\lambda_n}^2{t_r}^2}(\frac{(-1)^N}{E_{1,n}^2}(e^{\tilde{t_n}} - 1)^2(e^{\tilde{t_n}} - e^{\tilde{\nu_n}})^2 e^{-\tilde{\delta_n}-2\tilde{t_n}}$ $(e^{-\tilde{\Delta_n}}\left(-1 + (-1)^N e^{\tilde{\delta_n}}\right)^2$ $-2(1 + (-1)^N e^{\tilde{\delta_n}}(N - 1 + Ne^{-\tilde{\nu_n}})))$ $+N(2e^{-\tilde{\nu_n}}(e^{\tilde{t_n}} - 1)^2$ $-4(e^{-\tilde{t_n}} - 1 + \lambda_n D t_r))\lambda_n{}^3 D^3 {t_r}^2(1/\nu - 8t_r/3))$ $N = 2\delta\nu, \quad \tilde{\delta_n} = D\lambda_n\delta, \quad \tilde{\Delta_n} = D\lambda_n\Delta,$ $\tilde{\nu_n} = D\lambda_n/2\nu, \quad \tilde{t_n} = D\lambda_n t_r,$ $E_{1,n} = e^{D\lambda_n/(2\nu)+1}$

Table 2.2: Coefficients Γ_n describing the effect of the gradient waveform on the signal model [Murday and Cotts, 1968, Xu et al., 2009b, Ianuş et al., 2013]. Here, N represents the number of waveform lobes, t_r the ramp time, and ν the frequency of waveform oscillations.

radius a, the total signal becomes

$$S_{dSph} = S/S_0 = \frac{\int_{a=0}^{+\infty} a^3 p(a) S_{Sph}(a) \mathrm{d}a}{\int_{a=0}^{+\infty} a^3 p(a) \mathrm{d}a}, \tag{2.58}$$

where r and σ are the average radius and the spread of the distribution of spheres size. S_{dSph} is an additional brick to build a complete model of the signal related to the microstructure. Here, equation 2.58 is numerically solved, but many distributions have explicit models [Callaghan and Jolley, 1983].

Cylinder The second intracellular model describes the diffusivity confined in an impermeable cylinder [Stepišnik, 1993]. The cylindrical compartment is fundamental for the modelling of signal in white matter where axons have a preponderant dimension [Alexander, 2008]. The compartment has a finite dimension on the section plane, and an infinite longitudinal dimension. The signal attenuation, S_{Cyl}, is defined by two parameters: the radius, r, and the diffusivity, D. The coefficients of equation 2.56 become

$$B_n = \frac{2(r/\mu_n)^2}{\mu_n^2 - 1} \qquad \lambda_n = \left(\frac{\mu_n}{r}\right)^2 \tag{2.59}$$

where μ_n is the n–th root of $J_1(\mu) = 0$ with J_1 a Bessel function of the first kind and first order [Stepišnik, 1993, Xu et al., 2009a].

Spherical shell The final model is the spherical shell. Spherical shell compartment is designed to model the cytoplasm when nuclei have a comparable dimension to the cellular membrane. The compartment is limited by an internal and a concentric external sphere; therefore, three parameters are required: the inner radius, r, the outer radius, R, and the diffusivity, D. The description follows the approach from *Xu, et al. 2009* where

$$B_n = \frac{2r^3R^3[j'(\lambda_n r) - j'(\lambda_n R)]^2}{\lambda_n(R^3 - r^3)[r^3(\lambda_n^2 R^2 - 2)j'^2(\lambda_n r) - R^3(\lambda_n^2 r^2 - 2)j'^2(\lambda_n R)]} \tag{2.60}$$

and λ_n are defined in equation 2.59 [Xu et al., 2009a].

Part II

Investigation on emulsions

Chapter 3

Study of bi-phase emulsions with single wavelength diffuse scattering spectroscopy and diffusion NMR

3.1 Introduction

Non-destructive investigation of material microstructure is a general challenge for imaging science. Microstructure imaging exploits the sensitivity of the signal obtained from an imaging device to the microscopic architecture of materials, such as emulsion droplet sizes [van Staveren et al., 1991,Denkova et al., 2004], material inclusion in minerals [Kaiser et al., 1997] or indication of biological properties [Schmitt and Kumar, 1998], to estimate features of the microstructure within a sample. In biomedical imaging these ideas lead to the possibility of non-invasive histology. Histology provides the gold standard for diagnosis of a wide range of diseases [Assaf and Basser, 2005], but is invasive and limited to small target areas. Microstructure imaging potentially offers similar information, non-invasively, about the microscopic architecture throughout a sample, instead of a local description obtainable with a biopsy. Early demonstrations of microstructure imaging primarily focus on a

single imaging device [Alexander et al., 2010]. However, combining different modalities potentially enhances the technique because different modalities are sensitive to different physical contrasts that may be complementary to one another [Kramer et al., 2010].

Here, we present the first approach based on informing a model with the signal from two complementary modalities in order to obtain a quantitative description of the microstructure. This work demonstrates that microstructural parameters can be estimated with increased accuracy by informing a biophysical model with the signals from two distinct modalities: measurements of the near infrared Diffuse Optical Signal (DOS) and Diffusion Nuclear Magnetic Resonance (dNMR). Both techniques can measure the average size of the microstructural pores, but only dNMR can study the distribution of sizes, and only DOS is sensitive to the volume fraction between microstructural compartments where different chemical species compose the compartments. dNMR can provide information about the volume fraction from the peaks of different compounds, but the present implementation is optimised for the study of the oil peak only. This work presents a combined biophysical model able to cross-correct the estimation of the average size by exploiting the contrast mechanism from each modality. The model also improves the accuracy of other parameter estimates as a consequence of a more precise estimation of particle average size.

3.2 Methods

3.2.1 The problem

Here, we consider a simple material in which the microstructure is composed of two compartments: a homogeneous dispersion medium and spherical impermeable pores with a distribution, σ, of sizes, as shown in figure 3.1. The objective is to evaluate the mean size, r, of the particles in the microstructure, the spread of their size distribution, and the volume fraction, ψ, of the spherical pores (the particles), using DOS, dNMR, and the combined model.

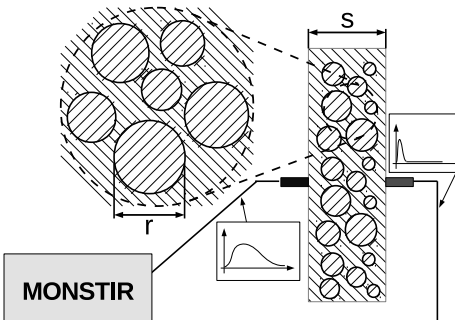

Figure 3.1: The model showing the microstructure geometry, where the size of microspheres a, is distributed with mean r and standard deviation σ. Inner and outer compartments are made of different materials with different properties. In the scheme, the experimental setup for the optical measurements is reported alongside the sample where source and detector are paired on the two sides of the sample.

The sample

The sample adopted in this study is commercial light mayonnaise (Sainsbury's Basic) produced by *J Sainsbury plc*. Mayonnaise is an emulsion composed of two compartments: rapeseed oil microspheres suspended in a dispersion medium of water and proteins. The microstructure is stable in time, and both DOS and dNMR are sensitive to it. It is isotropic, homogeneous, easy to store and its DOS and dNMR contrasts are similar to those of cells (for dNMR) and nuclei (for DOS) in biological tissues. The components of the emulsion are listed on the label, and they are mainly water, salt (1.5%), egg yolk (6%), and rapeseed oil (27%). Despite the apparent complexity of the dispersion medium, its homogeneity makes it easily usable, and the sample has a simple tissue-like microstructure.

The model

The optical model considers a set of homogeneous spherical scatterers with different sizes immersed in a medium. The refractive indices of scatterers and medium are different, and the medium and scatterers (droplets) have different absorption coefficients. The dMRI model considers a single compartment

representing the set of spheres inside which spins are confined (droplets) while the external spins are not modeled and they diffuse freely but cannot enter the spherical pores. The parameters of the optical model are the absorption and apparent scattering coefficients of the two compartments, the mean spherical pore radius, and the pore volume fraction. The parameters of the dNMR model are the diffusion coefficients in each compartment and the mean and standard deviation of the pore radius distribution. Thus the models have one parameter in common, r, and several unique for each modality.

3.2.2 Signal models

Diffuse optical spectroscopy

We take a novel approach in DOS by using time-domain measurements. Previous sizing applications use a multispectral approach by analysing a single intensity spectrum. Here, a TPSF at a single wavelength was studied to extract μ_s' and μ_a. The limitation to a single wavelength is compensated by the use of a very simple geometry.

The DOS model requires some of the optical properties describing the two compartments as prior information in order to estimate the microstructural parameters. Four parameters are fixed: the absorption coefficients $\mu_{a,i}$ and $\mu_{a,m}$, and the refractive indexes of the compartments n_i and n_m. The oil compartment parameters $\mu_{a,i}$ and n_i are well known in the literature [van Staveren et al., 1991, Michels et al., 2008], however this is not the case for the dispersion medium where the composition is relatively complex, and changes in the optical parameters n_m and $\mu_{a,m}$ lead to different estimates of parameters r and ψ. As a first approximation for this work, the parameters selected for $\lambda = 780\,\text{nm}$ are reported in table 3.1 where the dispersion medium is a mix of water ($n = 1.33$), vinegar ($n = 1.31$), flour ($n = 1.434$) and egg yolk ($n = 1.419$) [Vadehra and Nath, 1973]. A weighted average of the different compounds provides the parameters stated in table 3.1. Similarly for the absorption coefficient, data for the single components were obtained from the literature and an intermediate $\mu_{a,m}$ is obtained [Pickering, 1992, Chantrapornchai et al., 1999].

In DOS, the signal is modeled as a diffusive regime, and the microspheres

	μ_a (mm^{-1})	n
Oil	0.00077	1.471
Dispersion medium	0.0031	1.377

Table 3.1: Optical parameters for the two compartments at $\lambda = 780nm$.

are assumed to be all the same size. The signal is approximated by equation 2.11 in order to obtain the apparent scattering and absorption coefficients. MT is then used to correlate the microstructure with the scattering optical properties, while equation 2.21 takes refractive index and absorption coefficient into account. Finally, the function implementing the described steps, M_{DOS}, and relating a microstructure with unique radius r, and volume fraction ψ with its optical properties (μ_s', μ_a, n) according to MT and equation 2.21

$$(\mu_s', \mu_a, n) = M_{DOS}(r, \psi). \tag{3.1}$$

where MT provides a relation between r and ψ, and μ_s and g while μ_a is obtained from equation 2.21.

Diffusion NMR

The sample is modeled as a population of spherical pores (droplets of oil) with a log-normal distribution of sizes. Signals obtained from a Stimulated Echo (STE) [Tanner, 1970] sequence at different diffusion times and gradients strengths are fitted with equation 2.58.

Combined model

The combined model integrates the two previous approaches to obtain a common set of microstructural parameters. The model unifies the information in a common physical model which includes information from both modalities.

DOS can provide an estimation of the average radius of microspheres r, and of the volume fraction ψ, while dNMR provides r and the spread of size distribution σ, of the microspheres. In the integration, the DOS model only provides the average radius while dNMR fits the log-normal distribution. Since DOS

considers only a single radius of microspheres, the combined model redefines the optical coefficients to model a distribution of radii.

In order to combine DOS and dNMR models, the optical parameters are based on the log-normal probability distribution of sizes, and they are obtained as

$$\mu_s = N_0 \int_{x=0}^{+\infty} C_{sca}(x) p_{DOS}(x; r, \sigma) \mathrm{d}x \tag{3.2}$$

and

$$g = \frac{\int_{x=0}^{+\infty} g(x) C_{sca}(x) p_{DOS}(x; r, \sigma) x}{\int_{x=0}^{+\infty} C_{sca}(x) p_{DOS}(x; r, \sigma) \mathrm{d}x} \tag{3.3}$$

where N_0 is the number of microspheres per volume unity, $C_{sca} = \pi r^2 Q_{sca}(r)$, and Q_{sca} is the ratio between the scattering and the geometrical cross section [van Staveren et al., 1991,Michels et al., 2008]. The final value of $\mu'_s = \mu_s(1-g)$, and $p_{DOS}(x; r, \sigma)$ is a log-normal distribution of sizes as in section 2.2.3 in agreement with the literature [Denkova et al., 2004]. Note that the DOS data alone do not support estimation of both r and σ so we must represent the distribution of droplets radii by a single mean r parameter. Finally, similarly to equation 3.1 the optical parameters become

$$(\mu'_s, \mu_a, n) = M_{Com}(r, \sigma, \psi). \tag{3.4}$$

A schematic representation of the approach is presented in figure 3.2. The two signals are fitted at the same time with the models and a weighted combination of the two residuals is minimised.

3.2.3 Data acquisition

Diffuse optical spectroscopy

The optical experiments were conducted with *MONSTIR*. *MONSTIR* is a time domain integrated optical system that has been developed by the department of Medical Physics and Bioengineering at the University College London. The experimental system is provided with a set of 32 probes each composed by a source and a detector. The system is able to generate a train of light pulses

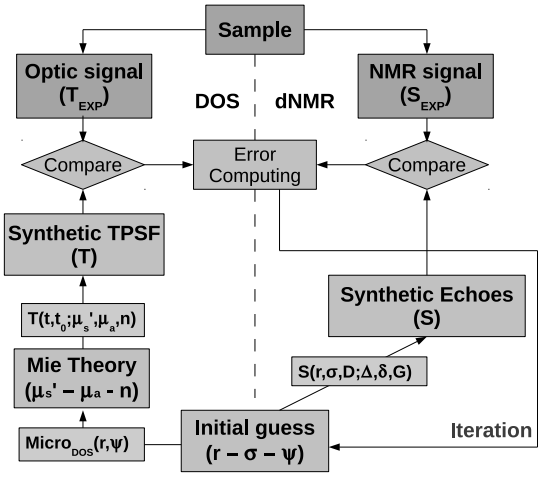

Figure 3.2: A scheme explaining the algorithm adopted in the combined model approach.

and to detect them with an accuracy of few nanoseconds. The generation and detection is synchronised and the system enables to change pulse intensity and to select between two wavelength 780 nm and 820 nm.

In the present work, Temporal Point Spread Functions (TPSF) were recorded in a transmission geometry. *MONSTIR* was used to generate a non-collimated laser beam of 3 ps pulses at 780 nm with a pulse interval of 12.5 ns between the used pulse and the unused 820 nm pulse [Schmidt et al., 2000, Jennions et al., 2006]. The intensity of the laser beam was reduced with neutral density filters. The mayonnaise sample was poured in a transparent plastic container of 17 $\times$ 50 $\times$ 50 mm^2 with a wall thickness of 1.5 mm.

The laser source was positioned in contact with the external surface of the container, and a detector was aligned on the opposite side, 17 mm away, in order to have a direct transmission measurement. A reference measurement was taken, averaged over 10 s of interrupted pulsing without the sample in position. The system is designed to The entire acquisition required about 1 min. Measurements with the sample in position were acquired by changing the position of source and detector along the sample. All the measures were normalised as $\|T(t, t_0; \mu'_s, \mu_a, n)\|_{l^2} = 1$, and the reference measurement was deconvolved from the measured TPSF to remove experimental artifacts due to

laser drift, fiber coupling and temporal delays in the fibers and cables.

Diffusion NMR

We applied a dNMR STE sequence to a $20 \times 20 \times 20\,\mathrm{mm}^3$ sample using a 9.4T Varian pre-clinical scanner. A set of measurements with each combination of diffusion times $\Delta = 50$, 100, 150, 200, 250, 400, 700 ms and gradients $G = 0.05$, 0.1, 0.2, 0.4, 0.6, 0.8, 0.95 T/m, $\delta = 5\,\mathrm{ms}$, and $T_R = 4\,\mathrm{s}$ was obtained. The echo time, T_E, was set to the minimum, corresponding to 2.5 ms after the end of the second gradient. The mixing time, t_m, was maximised by applying the first RF pulse immediately after the end of the first gradient. For every set of parameters (Δ,δ,G) four repetitions along the three orthogonal directions were taken, and the no diffusion gradient (G_0) scan was acquired for each repetition. The spectra obtained with different diffusion gradients were normalised against the signal obtained in each single direction independently when no gradients were applied. The full spectrum in each acquisition was processed to identify the oil peak corresponding to the signal from inside the spherical pores which informs the key parameters r and σ.

3.2.4 Parameter estimation

We calculated the microstructural parameters by fitting the model to the experimental data using a Levenberg-Marquardt algorithm. The dumping parameter of the algorithm was set to 0.01 after a trial and error approach. This choice was primarily determined by the the stability of the fitting of the optical signal. The DOS model estimates r, ψ and t_0, the dNMR model r, σ and D, while the combined model estimates all the parameters together: r, σ, D, ψ, and t_0.

The minimisation in DOS is performed with a multi-step procedure to enhance the robustness and to avoid convergences to local minima. The parameters are fitted in three steps consisting of different minimisations with Levenberg-Marquardt algorithms initialised with different guesses. The first step uses an arbitrary starting point with physically realistic values for each parameter, the second uses the initial guess of the radius, and the value of

concentration obtained by the first step; finally, the third step uses the minimised ψ (from the second step), and the radius fitted in the first step to find the remaining parameters.

The combined model uses the two signals together to define the distribution $p_{DOS}(x;r,\sigma) = p_{dNMR}(x;r,\sigma) = p(x;r,\sigma)$ and the volume fraction ψ. The objective function minimised is a weighted combination of the errors from the two signals

$$\begin{aligned}(r,\sigma,\psi) =& min_{(\hat{r},\hat{\sigma},\hat{D},\hat{\psi},\hat{t_0})} \\ & w \left\| T(t,\hat{t_0}; M_{Com}(\hat{r},\hat{\sigma},\hat{\psi})) - T_{EXP} \right\| \\ & + (1-w) \left\| S(\hat{r},\hat{\sigma},\hat{D}) - S_{EXP} \right\|\end{aligned} \tag{3.5}$$

where w is the weighting coefficient combining the errors from the two signals in the objective function, S_{EXP} the experimental signal for dNMR, and T_{EXP} for DOS. The model of optical signal $T(t,\hat{t_0}; M_{Com}(\hat{r},\hat{\sigma},\hat{\psi}))$, is defined by equation 2.11. The dNMR signal $S(\hat{r},\hat{\sigma},\hat{D})$ is obtained from equation 2.58 when we consider the special case of a SE gradient sequence.

A Monte Carlo Markov Chain (MCMC) algorithm was adopted to further investigate the properties of the model by sampling the posterior distributions on each parameter after locating the maximum likelihood estimate. MCMC consists of the generation of a Markov chain where the parameters are updated with a Gibbs sampler and the Metropolis algorithm [Walsh, 2004,Haario et al., 2006]. The computations were conducted on a laptop (Quad Core 2.2GHz, 8GB RAM).

3.2.5 Validation with confocal laser scanning microscopy

To validate the reconstructed microstructural parameters against results describing the microstructure obtained independently, the concentrations of the different compounds were taken from the label on the mayonnaise package, and the size distribution of the oil microspheres were measured using Confocal Laser Scanning Microscopy (CLSM).

A small portion of sample was diluted 1:1 with water and stained with

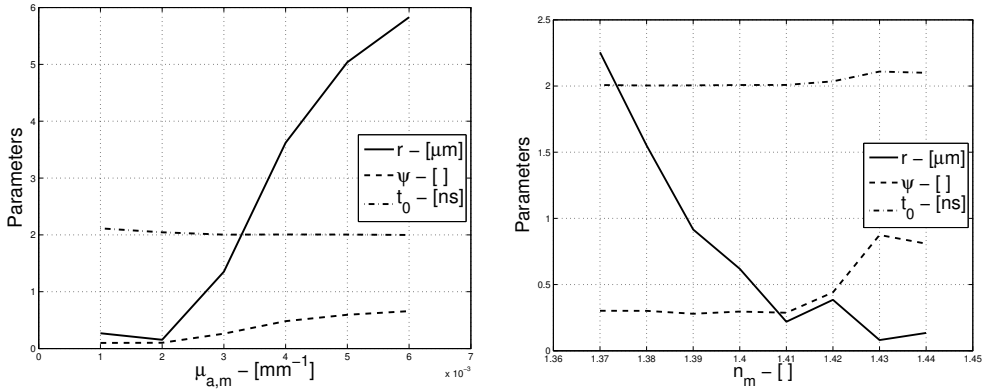

Figure 3.3: The change of input parameters in DOS model affects the estimation of microstructural parameters. In (a) the effect of the change of absorption coefficient ($\mu_{a,m}$), while in (b) the effect of refractive index (n_m) changes.

Rhodamine 6G, produced by Sigma-Aldrich Co. LLC. This dye stains the proteins surrounding oil globules, and therefore the oil, as red [Blonk and van Aalsh, 1993]. The diluted mayonnaise was spread on a slide and illuminated with light at 680 nm. A first set of 10 images were acquired varying the position of the focal plane and 5 other images by moving the position of the lenses on the slide in order to capture any differences between areas of the sample. The images were manually processed to determine the diameter of about 100 microspheres. Any sphere visible in the central part of four images were considered, and their diameter measured manually.

3.3 Results

3.3.1 Parameters of the models

We first assess the sensitivity of the microstructural parameter estimates to the fixed parameters. Here, the effect of changes in the fixed values of the absorption coefficients $\mu_{a,i}$ and $\mu_{a,m}$ and the refractive indexes n_i and n_m, and the weighting factor w are described.

Figure 3.3 shows the change in the estimates with different initial estimates of absorption coefficients and refractive indexes. Synthetic datasets were gen-

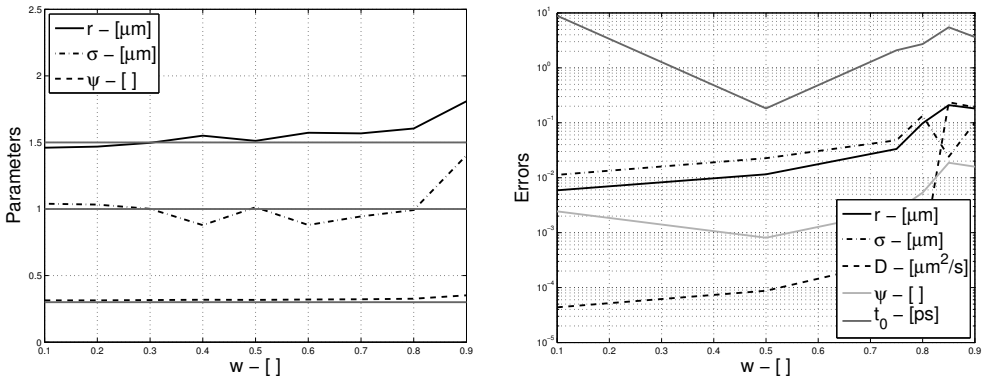

(a) (b)

Figure 3.4: Effect of the weighting parameter w on the error of fitting, and on the use of synthetic data to obtain the fitting at different w. In (a) the estimated parameters in a synthetic dataset generated with a SNR = 16, $r = 1.5\,\mu$m, $\sigma = 1.0\,\mu$m, and $\psi = 0.3$. In (b) the error obtained in the estimation.

erated by varying one parameter while keeping the other fixed as in table 3.1. The offset time t_0 is practically independent of the fixed parameters. The volume fraction ψ remains constant for $n_m < 1.41$ but increases steadily with $\mu_{a,m}$. Similarly, r increases with $\mu_{a,m}$, but a more non-linear dependency is observed with n_m.

Figure 3.4(a) reports the parameters fitted on a noisy synthetic dataset (SNR = 16, $r = 1.5\,\mu$m, $\sigma = 1.0\,\mu$m, and $\psi = 0.3$) at different values of w. A divergence of the estimates from their real values is observed for w greater than 0.9. Figure 3.4(b) shows the errors in the estimates at different values of w. Despite the increase in the error as the estimate of r with w, the estimates obtained from DOS only present a minimum when w is set to 0.5. The errors observed in all the other parameters (also related to dNMR) tends to increase with the value of w. For the further parts of this work, w is fixed at 0.5.

3.3.2 Simulation results

The models were first characterised using different synthetic datasets. Table 3.2 and 3.3 show the mean and the associated error (as standard deviation) of the estimates of r and ψ over different datasets. Noise-free synthetic datasets

model	1 μm	2 μm	3 μm
DOS	1.09(0.16)	2.13(0.67)	3.06(1.34)
dNMR	0.82(0.57)	1.93(0.63)	3.75(1.49)
Com	1.02(0.31)	1.98(0.21)	3.14(0.38)

Table 3.2: Estimation of r in groups of 50 synthetic datasets generated with SNR fixed at 16 and different microstructural parameters. The datasets are fitted with the two modalities independently and with the combined approach. Here, the estimation of r with the three modalities is applied on datasets generated with $r = 1, 2, 3$ μm, $\sigma = 1$ μm, and $\psi = 0.3$. Standard deviations of the parameter estimates are reported in brackets.

were generated for various combinations of microstructural parameters via Monte Carlo simulations, which are more accurate than the approximate models we fit but computationally more expensive. Noise was added such that the SNR was 16, and the parameters considered were $r = 1, 2, 3$ μm, σ= 1, 2, 3 μm and $\psi = 0.1, 0.2, 0.3$. The Monte Carlo code for DOS was implemented by modifying the widely available code *MCML* [Wang et al., 1995] where the tracking of the distance travelled by every single packet of photons in the sample is recorded. The noise is proportional to the square root of the number of events simulated and is Gaussian [Arridge, 1995a]. The dNMR signal was generated with Monte Carlo simulation [Hall and Alexander, 2009] in the Camino toolkit [Cook et al., 2006].

Table 3.2 presents the estimates of r. The combined model produces more accurate estimates of r with lower associated error, and the improvement against the single modalities increases with the size of the microspheres. DOS tends to provide better estimations than dNMR in terms of fitted values and error of estimation. The results from the estimation of the parameter ψ are reported in table 3.3, and an improvement of the estimation with the combined model is observed specifically for lower values of ψ. The identification of σ, directly depends only on dNMR, but is improved by the indirect effect of the enhanced estimation of r by the DOS in the combined approach 3.4.

model	0.2	0.3	0.4
DOS	0.2136(0.0701)	0.3071(0.0547)	0.3993(0.0374)
Com	0.1908(0.0376)	0.2957(0.0418)	0.3996(0.0379)

Table 3.3: Estimation of ψ in groups of 50 synthetic datasets generated with SNR fixed at 16 and different microstructural parameters. Here, the estimation of ψ, with DOS and combined modality, is applied on datasets generated with $\psi = 0.1,\ 0.2,\ 0.3$, $r = 1.5\ \mu$m, and $\sigma = 1\ \mu$m. Standard deviations of the parameter estimates are reported in brackets.

model	1	2	3
dNMR	1.2796(1.9971)	3.2816(4.4511)	3.1924(3.4141)
Com	0.9867(0.4059)	2.0394(0.8764)	2.8849(0.9069)

Table 3.4: Estimation of σ in groups of 50 synthetic datasets generated with SNR fixed at 16 and different microstructural parameters. Here, the estimation of σ, with dNMR and combined modality, is applied on datasets generated with $\sigma = 1,\ 2,\ 3\ \mu$m, $\psi = 0.3$, and $r = 1.5\ \mu$m. Standard deviations of the parameter estimates are reported in brackets.

3.3.3 Experimental results

The fitting of experimental data is shown in figure 3.5. Figure 3.5(a) shows a good fitting of the TPSF since there is a high number of scattering events to ensure the applicability of the diffusion approximation. Minor artifacts probably due to the reflection in the plastic box occur and are not considered in the model. The dNMR model fits the data well as shown in 3.5(b) at the longer diffusion times. A lack in fitting precision is obtained for the lowest gradient strengths and diffusion times. The fitted value of the diffusivity coefficient is $D = 0.0098\,(\mu\text{m})^2/\text{ms}$ which is in agreement with the expected value found in literature for the diffusivity of fat at room temperature ($D = 0.01\,(\mu\text{m})^2/\text{ms}$) [Denkova et al., 2004, Hollingsworth et al., 2004].

The estimates of microstructural parameters obtained with the models are reported in table 3.5 along with the CLSM ground truth. All three parameter estimates from the combined model are closer to the ground truth than from the individual models. Figure 3.6 presents one of the images acquired during the CLSM measurements. DOS appears to overestimate r, while dNMR and

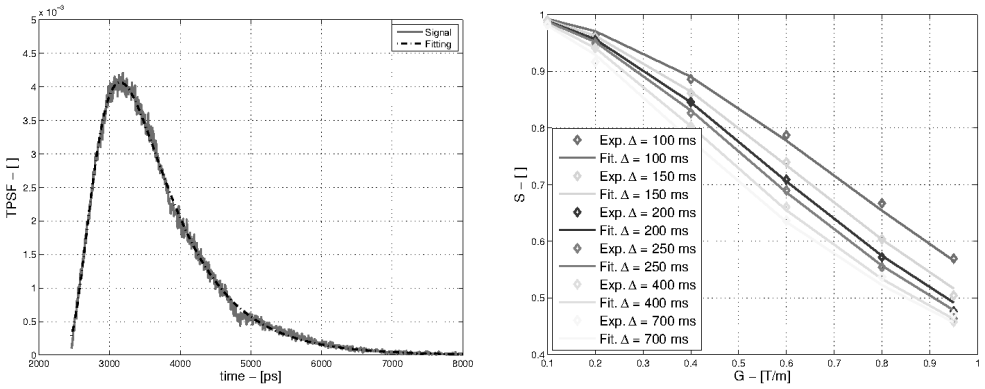

(a) (b)

Figure 3.5: Fitting of experimental data in DOS modality (a), and in the dNMR modality (b).

the combined model provide a close approximation to the distribution. Although the real value of σ is out of the confidence interval around the estimate from dNMR, an improvement is achieved with the combined model. A slight improvement of the fitting of the volume fraction occurs, but the ability of the method to converge to a suitable final result is highly improved in the combined model. Figure 3.7 reports the distribution of sizes estimated with the three models compared to the ground truth. It shows a change in the size distribution consistent with the better estimation obtained with the combined model.

3.3.4 Monte Carlo Markov Chain results

Figure 3.8 shows the solutions from a Monte Carlo Markov Chain (MCMC) chain of 10,000 steps after a burn in phase of 1,000 iterations for the microstructural parameters of interest and the CLSM results as ground truth. The variance between the elements in the Markov chain indicates the precision of the parameter estimates. The combined model improves the precision compared to the single dNMR model but the results differ from CLSM estimation in terms of σ. At the same time, DOS provides only the mean value of size which is biased and higher than CLSM.

Figure 3.9 shows the trend of MCMC chains of convergence to the final gra-

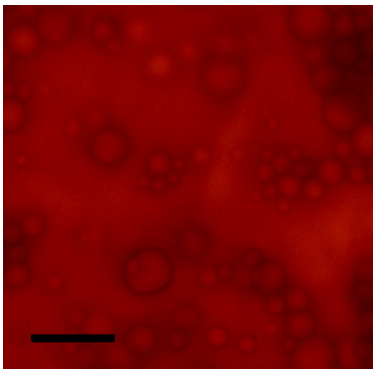

Figure 3.6: Image of the sample acquired using a Confocal Laser Scanning Microscopy as described in section 3.2.5. The black bar indicates a length of ten microns.

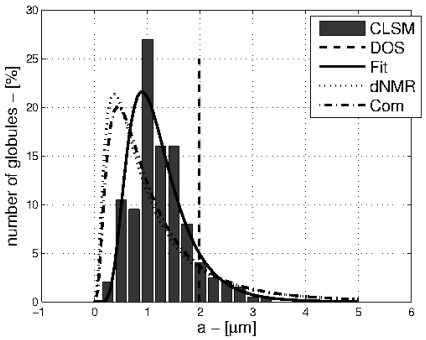

Figure 3.7: Estimation of the size of radii estimated with DOS, and the distributions obtained with dNMR and (Com) the combined model. The ground truth values obtained with CLSM are also shown, and fitted with a log-normal distribution (Fit).

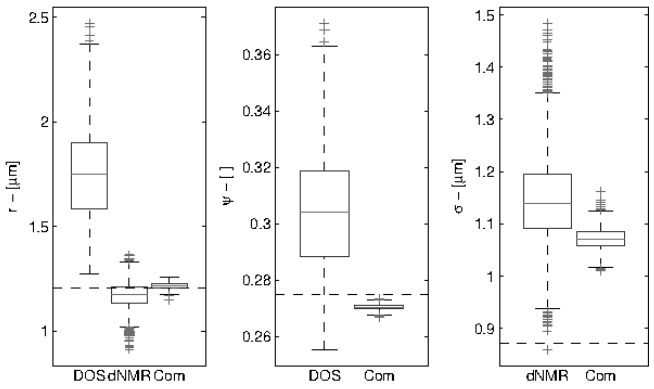

Figure 3.8: Monte Carlo Markov Chain solutions in a 10,000 solution chain for the estimation of r, ψ, and σ.

dient descent value of parameters. All the Markov chains start from a solution obtained with a single minimisation of the objective functions. The convergence is enhanced by the combination of modalities, while the DOS modality requires a longer number of iteration to reach a stable set of parameters. Moreover, the variance obtained with the combined method is reduced compared to the other two models.

3.4 Discussion

3.4.1 Overview of the results

The whole set of parameters may only be obtained at the same time by the combination of DOS and dNMR data. DOS estimates r and ψ, and not σ, while dNMR provides r and σ but not ψ. The DOS model requires the absorption coefficients and refractive indexes of the two compartments, which have been retrieved from the literature [Vadehra and Nath, 1973, van Staveren et al., 1991, Pickering, 1992, Chantrapornchai et al., 1999, Michels et al., 2008]. The parameters of the inner compartment are well known while the absorption of the dispersion medium has been deduced from its chemical composition. The absorption coefficients and refractive indexes could be obtained more accu-

model	r (μm)	σ (μm)	ψ
DOS	1.981(0.465)	-	0.324(0.041)
dNMR	1.168(0.078)	1.255(0.174)	-
Com	1.197(0.011)	1.192(0.0234)	0.268(0.001)
CLSM	1.439(0.218)	0.623(0.244)	0.293

Table 3.5: Value of r, σ and ψ obtained in with a Markov chain of $10,000$ elements with the three models. The values are the average estimation while in brackets are shown the related standard deviations. The values in brackets in the CLSM entries are the standard deviation of the parameters calculated utilising the distributions obtained from different microscopy images, the CLSM image technique does not present significant limitations in the detection of small oil droplets in this context. The volume fraction is instead a manufacturer datum and no variation could be obtained.

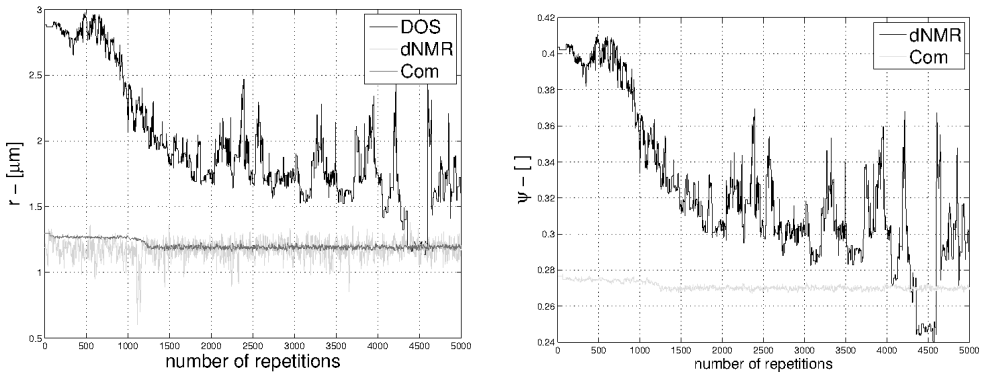

(a) (b)

Figure 3.9: MCMC chains related to (a) the radius, and (b) the volume fraction in the different models. Here, the chain are shown with their burn in phase included for only the first 5,000 solutions.

rately by further experiments, but this problem is outside the scope of this work.

Modelling the optical signal with Mie theory introduces an oscillatory dependence of the optical parameters on r [Ishimaru, 1978]. The objective function of the model introduces multiple local minima identified by similar pairs (μ_s', μ_a) but corresponding to different microstructural parameters. The accurate estimation of microstructural parameters depend on a precise choice of the initial guess, and this dependency on initial guess is one of the main disadvantages of this modality. A further disadvantage is the absence of sensitivity to the distribution of sizes due to the introduction of the DA which does not model angular dependency of the scattering.

The dNMR model does not require input parameters other than assuming the shapes and distributions, and the obtained value of the diffusivity coefficient is close to the expected value from literature, confirming the accuracy of the model [Denkova et al., 2004]. The model is very sensitive to the microstructure and the fitting depends only slightly on the initial guess. The time required for the fitting is around 5-10 s and the model shows a strong sensitivity to the microstructure. However, this modality is not able to provide information about the volume fraction.

The combined model provides enhanced accuracy compared to the single modalities. It is insensitive to the initial guess since it exploits the dNMR properties, but the fitting of distribution is improved thanks to the contribution of DOS which cross-informs the model about r. Finally, the estimation of concentration is also improved due to fitting the size with a robust model such as that of dNMR.

3.4.2 Experimental results

Finding a material able to provide experimental signals from both DOS and was challenging but mayonnaise works well for this simple demonstration. The measurements obtained with the DOS modality were sensitive to the shape of the container, and reflections deteriorated the weak signal produced by the high absorbing sample. Other researchers have used aqueous diffusion medium such

as intralipids, but these separate too quickly to be used with dNMR. Another potential confounder to the dNMR acquisitions is the presence of air bubbles.

The results obtained by the use of the combined model on the experimental signals shows an improvement of the fitting of all the microstructural parameters against the single modality models. The comparison against the CLSM indicates a discrepancy between the two measurements due to the spread of the distribution. dNMR is possibly unable to fit the larger microspheres accurately due to the low diffusivity of fat molecules compared to water (which is more common to measure with dNMR): even at the largest diffusion time in our experimental protocol, the root mean squared displacement is 3.75 μm. At the same time, a probable coalescence between the smaller bubbles in the sample may produce the narrowing of σ recorded in the CLSM estimation.

The fitting of the parameters related to the size appears to be driven by the dNMR modality. In fact, the distribution of radii estimated with the dNMR and combined modalities do not differ strongly, but the information added in the optical data improves the quality of estimation a little. Since, the optical model is not able to provide an estimation of the spread of the radii distribution, any w factor over-weighting the DOS model will result in instability.

3.4.3 Accuracy of the model

The MCMC algorithm reveals the convergence properties of the three methods. The results presented demonstrate a reduced capability of DOS to define a pair of parameters r and ψ representing the microstructure which generates the experimental TPSF; in fact, many pairs (r, ψ) can provide similar TPSFs and the fitting is not as accurate as with the other modality. MCMC for the DOS modality requires more than 1,000 iterations to converge, while dNMR is quicker, and the initial set of parameters estimated by a single minimisation algorithm are very distant from the point of convergence of the chain. The dNMR model is very selective and the parameter estimates are robust to the choice of algorithm. The Markov chains are very regular proving the strong stability of the model which is able to discriminate between the information

contained in different signals.

The MCMC analysis of the combined model illustrates the complementarity of information between the two single modalities. The parameters directly detected by the dNMR model preserve the stability of their chains, showing that properties and advantages of single modalities may be inherited by the combined method. At the same time, the volume fraction estimation is also improved by the interaction between the two modalities. The information contained in the dNMR signal constrains the size estimation and it drives the DOS model to estimate the volume fraction based on an appropriate distribution of radii. At the same time, the mean of distribution of radii is informed by the DOS modality, creating a strong correlation.

3.5 Conclusion

The use of combined models increases the accuracy of the fitting because of the interdependence between the single techniques. The approach is general and may be extended to other complementary modalities, i.e. diffraction X-ray and laser scattering spectroscopy, by adapting the model only. The demand for a more advanced microscopy investigation, and an improved sample is clear. This approach can be applied to diagnosis of epithelial cancer with the combination of diffusion MR and laser scattering spectroscopy.

DOS measurements can be performed quickly and easily, whereas dNMR measurements require a large, static scanner and are slow (around 1.5 hrs). A combined imaging system may be able to generate good quality fits with a faster imaging system than using dNMR alone. The two modalities are also able to observe different properties of the sample; therefore, they can be used in more advanced models where the correlation between different aspects is important in the description of a pathology.

This first demonstration of the benefits of multimodality for estimating microstructural material features provides motivation for further work on more complex models appropriate for biological tissue and eventually devices enabling multimodal microstructure imaging and non-invasive histology.

Chapter 4

Study of bi-phase emulsions with multiple wavelength optical spectroscopy and diffusion NMR

4.1 Introduction

The microstructural features of a tissue have different dimensions and their characterisation requires contrast at different scales. The scale of interest in this work is the micrometers where the maximum geometrical and biochemical diversification relates to specialisation of cellular substrates or disease conditions [Weinberg, 2013, Orchard, 2011, Junqueira et al., 1977]. Different investigation techniques obtain contrast exploiting different physical mechanisms and they can be more appropriate for the study of specific microstructural components. Tuning the parameter of the technique allows to maximise the contrast on the microstructural components of interest (i.e. cell size, or presence of specific proteins etc) as discussed in sections 3.1 and 3.2.

Optical techniques based on infrared light propagation can be utilised to describe scattering properties of the tissue. Scattering can be related to the dimension and the optical properties of the population of scatterers, such as

the mismatch of refractive index inside the microstructure. Standard scattering experiments tend to perform very well on sample with populations having a narrow distribution of sizes and diluted emulsions [Flock et al., 1992, Michels et al., 2008]. Both oil in water (O/W), and water in oil (W/O) emulsions have been deeply studied, but intralipid emulsions are growing in importance. Intralipid emulsions are well characterised soybean oil in water emulsions utilised in pharmacological industry, but they are growing importance as tissue-like samples [van Staveren et al., 1991, Di Ninni et al., 2011]. Despite the microstructure of emulsions appearing different from biological that of biological tissues because of scatterers different concentration and dimensions spanning over different magnitudes, they offer similar signals [Flock et al., 1992, Ding et al., 2005, Sankaran et al., 1999]. Nevertheless, the larger complexity requires additional information that could be obtained with the use of multiple wavelengths chosen accordingly to all the characteristic dimensions of interest.

Optical scattering measurements rely on the changes of refractive indices between the compartments in the microstructure. The ratio of the size of compartments to the wavelength is the scale parameter dominating the physics in the vis-NIR light domain, along with the absorption. Since larger differences in the signal can be obtained when scatterers and wavelength have similar magnitude, the selection of the light properties focuses the contrast on specific elements [Mie, 1908]. In a biological tissue, we are interested in the dimensions of organelles, nuclei and cells, whose dimensions span in the range from 0.1 to 10 microns. A selection of such characteristic dimensions in contrast to nanoscopic properties related to other components (i.e. collagen) could be performed by comparing and merging signals at different wavelengths. The observation of changes along controlled wavelengths allows the contribution from scatterers of different dimension which compose the signal to be distinguished.

The multiple wavelengths approach in optical scattering measurements is similar to the approach with dNMR. The use of different diffusion times separates the contribution to the signal from compartments with different sizes. The most interesting for our purpose are the use of different diffusion times to estimate any arbitrary distribution of sizes [Hollingsworth and Johns, 2003b, Hollingsworth et al., 2004]. Different diffusion times on a Stim-

ulated Echo (SE) sequence are able to capture the exact apparent diffusion defined by the confinement in different parts. The identification of each single contribution leads to the recovery of the microstructural features observed. Similarly for the optical modality, the separation of contributions at each single wavelength enables a characterisation of the sample. In this work, these two approaches are combined using a similar approach to that described previously.

The samples adopted in this work are emulsions of oil in water (see also section 3.2.1) [van Staveren et al., 1991, Michels et al., 2008]. A presence of a microstructure divided in two well separated compartments is well known for intralipids [van Staveren et al., 1991]. For oil in water and water in oil emulsions such as mayonnaise, the microstructure is more complex and additional elements or chemical compounds can be found [Bower et al., 1999]. Nevertheless the presence of two main compartments in the microstructure reduces the parameters to be estimated to the volume fraction, ψ, between the two compartments, the ratio between the refractive indexes, m, and the information about the size of droplets: mean radius, r, and spread of distribution, σ as reported in figure 4.1.

The aim of this piece of work is to improve the approach described in chapter 3 to Diffuse Scattering Spectroscopy (DSS), and to describe the results of a modality combining optical scattering techniques and Diffusion NMR (dNMR) as presented in section 3.2. No general solutions could be described since the changes in sample and technology alters the results. Nevertheless, we aim to move a step further based on the implementation of a multiple wavelength optical scattering technique and the use of a new optical system, *MONSTIR II*, enabling multiple wavelength acquisitions [Hebden et al., 2012].

The migration of photons in a sample under the diffusion regime is dominated by a material's scattering and absorption properties. The two properties are related to the nature of the substances in the sample and to the geometry of the microstructure [Dahm and Dahm, 2001]. Absorption is a volume-related property, where the interaction of light with chemical bounds of the molecules determines a transfer of energy and a reduction of absorption of the beam energy. Absorption has a very complex physics but can highlight the presence of some specific compounds as in the standard spectroscopic approach [Enfield

and Gibson, 2012]. Nevertheless, due to the proportionality of the absorption to the volume (and mass) of material encountered by the light, it is difficult to describe the entire microstructural composition. Scattering is a more selective process, relating internal microscopic reflection which, in principle, can be isolated at different scales [Dahm and Dahm, 2001]. In this work we excluded the information related to absorption, concentrating our models on the contributions from scattering only [Schmitt and Kumar, 1998].

Figure 4.1: Model of the microstructure. Different colors indicate different compounds, with corresponding refractive indexes and diffusivity.

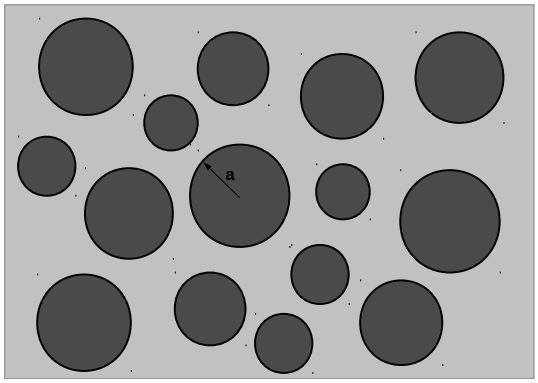

The natural upgrade of the model presented in chapter 3 consists of utilising multiple wavelengths simultaneously. Although a new method is developed, no additional theoretical framework is required for the optical technique, and the dNMR technique has already been fully presented in chapter 3.

4.2 Methods

4.2.1 The problem

The sample

In this chapter we consider two oil in water emulsions: the emulsion described in section 3.2.1, and a solution of intralipids. The objective remains to evaluate the mean size, r, of the particles in the microstructure, the spread of their size distribution, and the volume fraction, ψ, of the spherical pores (the particles),

using DOS, dNMR, and the combined model.

Intralipids phantoms with a concentration of 1% (v/v: volume concentration) of the original 20% stock solution (*Sigma–Aldrich*, Canada) were used to mimic the scattering properties of biological tissue. Intralipid emulsions are a mixture of soybean oil and distilled water which has a microstructure composed by oil droplets. The solution of intralipids was diluted with distilled water to obtain a final emulsion concentration of 1% oil-in-water. The microstructure is stable in time and the dimension of the droplets are in the order of 100 nm of diameter [Di Ninni et al., 2011]. Intralipid solutions offer a well-characterised microstructure to be utilised for calibration of new technologies [van Staveren et al., 1991, Di Ninni et al., 2011].

Scatterer size distributions

The framework described in section 2.1.3 provides an approach for estimating the size of particles in a population all of which have the same, unique radius, a. Here, starting from the idea presented in section 3.2.2, we model the contribution to the signal of a population of scatterers with a distribution of radii. As described in section 3.2.1, the microstructure is composed of a set of spherical particles randomly distributed in the volume, and we do not consider interaction between particles.

In this multi-wavelength approach, different distributions of scatterer sizes p_{DOS}, are considered. The microstructure is modelled as an ensemble of particles with a distribution of dimensions with mean r and standard deviation σ, and volume fraction ψ as described in section 3.2.1. Here three distributions p_{DOS}, have been considered:

- Single radius value (mean r, spread $\sigma = 0$);
- Gaussian distribution (mean r, spread σ);
- Log-normal distribution (mean r, spread σ).

Different distributions can be more appropriate for different microstructures. The *single radius* approximation is a straightforward model when nuclei

have all the same size and organelles do not contribute to the signal. This is a common approximation but it does not represent the complexity of biological tissue [Chalut et al., 2008, Drezek et al., 1999]. The *Gaussian* distribution can model scenarios when the low volumetric density allows a random allocation of the particles and the extension of each particle is not constrained by the presence of other particles. Moreover, since the Gaussian distribution allows for negative values, the average must be much higher than the standard deviation to avoid negative dimensions [Callaghan and Xia, 1991, Perelman et al., 1998]. Finally, the most common representation of emulsion microstructures is the *log-normal* when size of droplets is large enough to have a confinement due to the presence of other droplets which also has positive values only [Denkova et al., 2004, Michels et al., 2008].

4.2.2 The optical model

The optical model presented in chapter 3 has been modified to account for acquisitions of multiple wavelength diffuse scattering spectroscopy data. The physics of TPSF signals is modelled with the approach described in section 2.1.2, but the additional information contained in the scattering spectrum (TPSFs at different wavelengths) provides multiple length scales of observation over the microstructure.

The model describing the optical signal fits the apparent scattering coefficient spectrum as described in figure 4.2. The parameters μ'_s, and μ_a are estimated by fitting each TPSF with the model described in equation 2.11 at each wavelength independently. The set of $(\mu'_{s,i}, \mu_{a,i}, t_{0,i})$ ($i = 1 : 12$ indicates the wavelength) generates the spectra describing the sample, and $\{\mu'_{s,i}\}_i$ contains the information about the microstructural features. The values of $\mu_{a,i}$ and $t_{0,i}$ are discarded as they are auxiliary parameters for the fitting of the TPSFs.

The diffusion approximation time-domain model is convolved to the reference signal for the corresponding wavelength. Convolution is performed with a Levenberg-Marquardt algorithm performed over the TPSF signal normalised to a norm l^2 after the subtraction of the darkroom offset. The reference signal

is not normalised, no offset was subtracted, but the initial step is removed.

MT relates the microstructure to the scattering optical properties. This is implemented by the function M_{DSS} which connects a microstructure with distribution of scatterer radii $p_{DSS}(r, \sigma)$, volume fraction ψ, and refractive indexes ratio m, to the apparent scattering coefficient $\mu_s'(\lambda)$ as

$$\mu_s'(\lambda) = M_{DSS}(r, \sigma, m, \psi), \tag{4.1}$$

for each wavelength λ. Absorption coefficient μ_a, is estimated directly on the TPSF, and the refractive index n of the sample is fixed a-priori.

The microstructural parameters are obtained by fitting equation 4.1 to the scattering spectrum. Four parameters are fitted over the 12 data points, instead of two parameters against two data points in chapter 3. The parameters of interest are the r, σ and ψ and they will be integrated with the dNMR parameters.

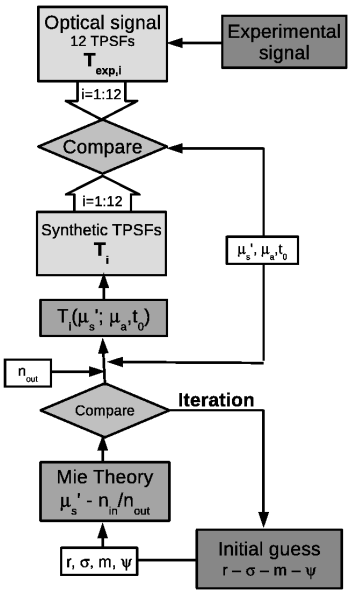

Figure 4.2: The scheme representing the algorithm utilised to fit the data. The optical model is presented in all the .

4.2.3 The combined model

The aim of this work is to develop a model informed by Diffuse Scattering Spectroscopy (DSS) and Diffusion NMR (dNMR) techniques. Both techniques can characterise dimensional properties of the microstructure via scattering properties in the optical modality and signal attenuation in dNMR.

The combined modality fits a linear combination of normalised signal errors from the two modalities. The object function is a combination of the errors obtained by subtracting the signal generated with the modelled microstructural parameters, and the experimental signals as

$$\begin{aligned} Err(r,\sigma,\psi) = w \left\| M_{DSS}(r,\sigma,\psi,m)) - C_{EXP} \right\| \\ + (1-w) \left\| S(r,\sigma,D) - S_{EXP} \right\| \end{aligned} \tag{4.2}$$

where w is the weighting coefficient, $C = M_{DSS}(r,\sigma,\psi,m)$ is the apparent scattering coefficient generated by Mie theory, and C_{EXP} the spectrum estimated from the 12 TPSFs. The dNMR experimental signal is S_{EXP}, and $S(r,\sigma,D)$ is the echo attenuation modelled as described in section 3.2.4. The coefficient w selects the contribution of each modality in the fitting process as discussed in section 3.3.1.

The combined model is described in figure 4.3. The object function in equation 4.2 is minimised by choosing the optimal microstructural parameters which reduce the discrepancy between synthetic signals and experimental measurements. A nested loop optimises the value of absorption coefficients to minimise the distance between synthetic TPSF and measurements for each wavelength.

4.2.4 Data acquisition

The system of measurements: *MONSTIR II*

MONSTIR II is the second version of the time-domain near infrared imaging system presented in section 3.2.3. The new system addresses the necessity of spectroscopic measurements to capture absorption peaks for metabolic investigations [Pogue et al., 2004]. *MONSTIR II* enables the supercontinuum laser

Figure 4.3: Scheme representing the algorithms used to fit the data in the multimodality approach.

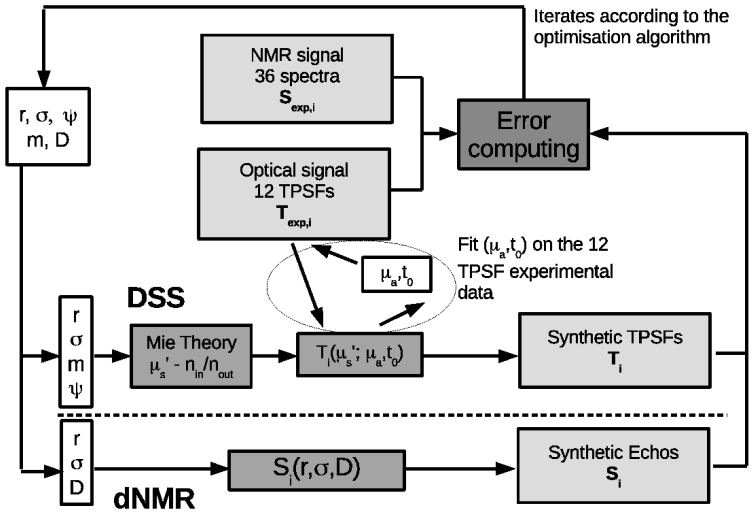

to be tuned continuously to obtain wavelengths from 650 nm to 900 nm, and to record four TPSFs at different wavelengths simultaneously.

The design of *MONSTIR II* is presented in figure 4.4. The laser source generates a packet of photons at a specific wavelength, a switch directs the photons through a single glass optical fiber, and all the Photon Multiplier Tubes (PMT) from the other fibers count the number of photons detected. Counts are recorded and processed in a computer working as controller. The system is completely controlled by a C++ homemade software while a LabVIEW-style interface provides control of the wavelengths and number of averages of pulses.

***MONSTIR II* light signal** The main technical features and performance of MONSTIR systems are reported in table 4.1. The system generates 1 ns pulses in trains of 4 pulses at four different wavelengths separated by 12.5 ns. Thirty-two source/detector probes offer a simultaneous measurement of TPSFs at different points. All the probes have a central source fibre, surrounded by a bundle of detector fibres with an external diameter size of 5.5 mm. The source is not collimated and has a Numerical Aperture (NA) of 0.25. The PMT can detect photons in a broader interval of time than the first version of

Figure 4.4: Scheme representing UCL time-resolved imaging system *MONSTIR II* general design. (Image courtesy of Prof J Hebden)

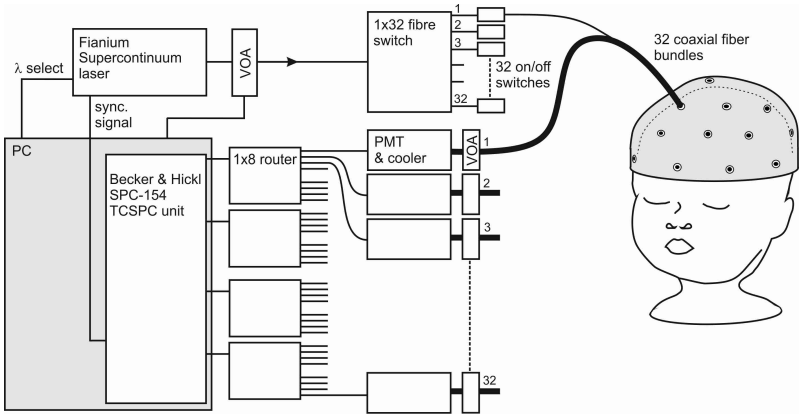

MONSTIR, and detection can be regulated with 12 neutral density filters to avoid detector saturation. The temporal resolution is about 280 ps, lower than in the previous system (*MONSTIR I*), but this feature becomes less important in thick or highly scattering media where the time between the impulse and the detection becomes longer. quality of the measurements even when source and detectors are below 2 cm of distance.

***MONSTIR II* calibration** The system is designed for the detection of absorption properties of samples. The characterisation of scattering properties requires additional attention, but the homogeneity of the sample does not require any reconstruction algorithm [Wang et al., 2005, Wang et al., 2006]. The characteristics of reference signals are presented in figure 4.5. A primary peak due to the transmission of light from the laser to the detector can be observed, and a secondary peak with reduced intensity possibly represents a reflection within source or detector. The system provides a very high SNR and a reduced background noise.

Selection of the wavelengths

The selection of the wavelengths characterise the dimension of microstructural features described by the scattering properties. The direct fit of absorption properties in time-domain enables a choice of the wavelengths where no ab-

	MONSTIR I	*MONSTIR II*
Source:	Fibre laser. Two fixed wavelengths (780 nm, 815 nm). Interleaved.	Supercontinuum laser. Four selectable wavelengths. Switched at 1kHz.
Detectors:	Four 8-channel MCP-PMTs. Thermoelectrically and water cooled.	32 PMTs. Thermoelectrically cooled.
Detector crosstalk:	0.3 %.	None
Temporal resolution:	100 ps.	280 ps.
VOAs:	Eight pinholes: 0 - 2 ND.	12 regions of variably exposed film: 0 - 3.7 ND

Table 4.1: The specifications of old and new MONSTIR systems compared in their more practical features.

Figure 4.5: Scheme of the effects of source and detector position.

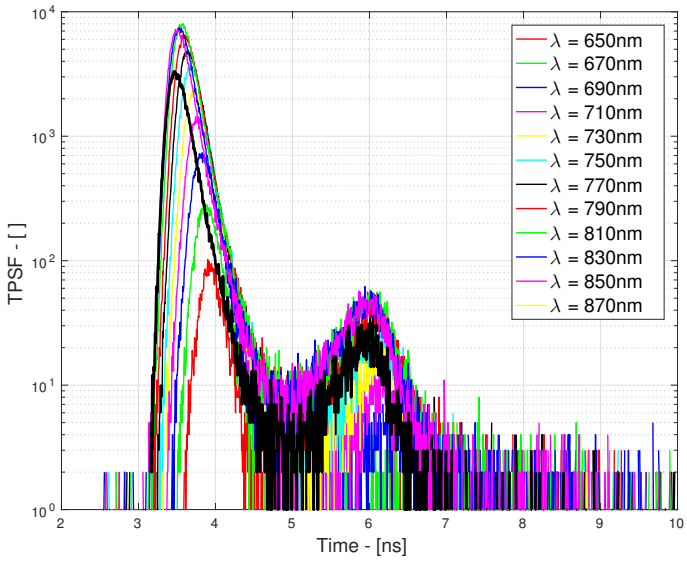

sorption peaks can be observed. The use of multiple wavelength to detect both absorption and scattering properties requires to acquire TPSFs at the absorption peaks but also over a homogeneous distribution able to describe the

scattering from scatterers of different sizes [Pogue et al., 2004, Gurjar et al., 2001].

The choice of wavelengths should follow different trends in the scattering properties from the droplets of different sizes. At the same time, the presence of strong absorption peaks can alter the signal obtained and the accuracy of the fitting. Since no hard absorption peaks are expected in the near infrared, a set of 12 equally spaced wavelengths, from 650 to 850 nm is adopted, see figure 4.6. This set of wavelengths contains 790 and 810 nm correspond to the maximum absorption peaks of oxy and de-oxyhemoglobin and can be adopted to distinguish their concentrations in clinical translation [Matcher et al., 1999]. Also the presence of fat is more important in a solution of oil in water, but the first relevant peak (at around 930 nm) is higher than the wavelengths achievable with the system adopted [Matcher et al., 1999, van Veen et al., 2004].

Figure 4.6: Spectra of laser intensities at the chosen wavelengths. The figure shows the spectrum generated by the super-continuous laser tuned on each wavelength adopted. The laser provides a Gaussian-shaped spectrum with bandwidth of 4 nm.

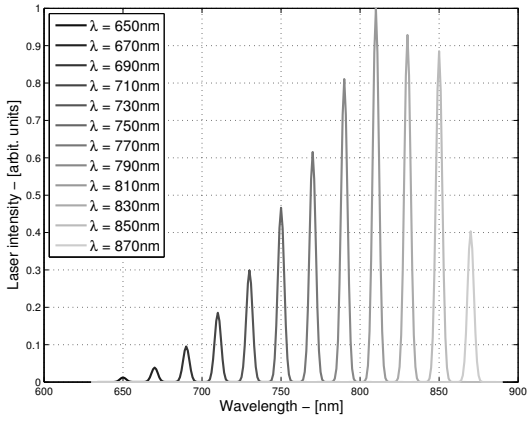

Experimental procedure

The experiment is performed in a reflection geometry on a homogeneous sample. The container was a box with dimensions 200x80x120 mm^3 made of plastic, transparent at vis-NIR light. All walls were 2 mm of thickness, and all edges

sealed with silicone. The samples were poured to cover at least 2/3 of the height of the container to provide enough room to avoid edge effects. Light was shined from the top, by placing the source in touch with the surface of the sample. Similarly, the detector was set parallel and in touch with the surface to avoid additional reflection. All the positioning was performed with laboratory beads.

The geometry of the experiment enables the diffusion approximation discussed in 2.1.2 to be applied. Furthermore, it is necessary to ensure a large enough source/detector separation to avoid ballistic or weakly scattered photons as illustrated in figure 4.7. Similarly, the distance between source or detector and the box surfaces must be sufficient to avoid interaction with the surfaces. Practical experience suggests that less than two times the distance set between source and detector is sufficient. The design of the distance between source and detector depends on the apparent scattering coefficient μ_s', and in this experiment was set to 16 mm and 28 mm depending on the experiment.

The experiments were performed with the system *MONSTIR II*. Four wavelengths were selected at each stage of the acquisition. Each acquisition were composed by three stages where contiguous wavelengths from the selected set, and one channel is selected for light generation and one for detection. Measurements are averaged over 10 s. The experiments were performed on two samples: intralipids and oil-in-water emulsion. Three repetitions were acquired for each sample with a source/detector separation distance of 16 mm, and only one with a separation distance of 28 mm. Reference measurements were acquired for each single wavelength by placing the two fibers in touch, and with an otherwise identical protocol.

The dNMR model adopted was presented in chapter 3. The distribution of particle dimensions, and the molecular diffusivity D are estimated from the echo attenuation $S(r, \sigma, D; G, \Delta, \delta)$ utilising six Δ and six G, 36 measurements. Under the hypothesis of a distribution of spherical compartments, signal is modelled with equation 2.58.

Figure 4.7: Signal recorded using source and detector in contact. The TPSFs presents the characteristic properties of the light generation and detection systems.

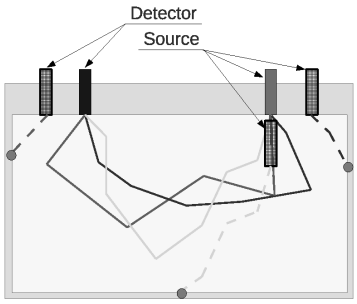

4.2.5 Parameter estimation

We calculated the microstructural parameters by fitting the models to the experimental data using a Levenberg-Marquardt algorithm. The optical model estimates r, σ, ψ, and m, the dNMR model r, σ, ψ, and D while the combined model estimates all the parameters together.

The fitting of the optical model is performed directly with the algorithms presented in section 4.2.2 on the values of apparent scattering coefficient spectrum C_{EXP}. No intermediate steps are required as presented in section 3.2.4 since the data available lead to a well-conditioned problem. The combined model uses the two signals together to define the distribution $p_{DSS}(x; r, \sigma) = p_{dNMR}(x; r, \sigma) = p(x; r, \sigma)$ and the volume fraction ψ. When the DSS model is applied, the objective function minimises a weighted combination of the errors from the dNMR signal and from the apparent scattering spectrum estimated from TPSFs. The objective function is

$$\begin{aligned}(r, \sigma, \psi, m, D) = & min_{(\hat{r},\hat{\sigma},\hat{\psi},\hat{m},\hat{D})} \\ & w \left\| M_{DSS}(\hat{r}, \hat{\sigma}, \hat{\psi}, \hat{m})) - C_{EXP} \right\| \\ & + (1 - w) \left\| S(\hat{r}, \hat{\sigma}, \hat{D}) - S_{EXP} \right\|,\end{aligned} \tag{4.3}$$

where w is the weighting coefficient combining the errors from the two signals in the objective function. The model of optical signal, $M_{DSS}(\hat{r}, \hat{\sigma}, \hat{\psi}, \hat{m}))$, has

been defined by Mie theory while the dNMR signal $S(\hat{r}, \hat{\sigma}, \hat{D})$ by equation 2.58.

A Monte Carlo Markov Chain (MCMC) algorithm was adopted to further investigate the properties of the model by sampling the posterior distributions on each parameter after locating the maximum likelihood estimate. MCMC consists of the generation of a Markov chain where the parameters are updated with a Gibbs sampler and the Metropolis algorithm [Walsh, 2004,Haario et al., 2006]. The computations were conducted on a desktop (Quad Core 4.2GHz, 8GB RAM).

4.3 Results

4.3.1 Optical signals and noise

The fitting of diffusion approximation TPSF models to the data might be affected by the noise. Variation of noise level between different wavelengths and in the position in the TPSF contribute to the quality of microstructural parameter estimates.

Figure 4.8 presents the TPSFs (not calibrated) from the intralipids at all the wavelengths with a source/detector separation of 16 mm. The noise is below 2% over the entire signal from intralipids, and a pure logarithmic decay is observed until 5.5 ns when the decrease remains logarithmic, but with a lower attenuation. This is likely due to internal reflections between surface of the material and probes or due to the walls. The low absorption in the medium, and high scattering suggests that the anomalies, occurring in all the measurements at the same time, are likely to be related to the geometry. This explains the different TPSFs obtained with a different separation.

Figure 4.9 presents the TPSFs (not calibrated) from mayonnaise samples at all the wavelengths with a source/detector separation of 16 mm. The signal does not show the reflection artifacts presented by intralipids measurements, and a higher Signal Noise Ratio (SNR) can be observed. Axis scales are different between intralipids and mayonnaise axis as mayonnaise signal shows a larger scattering and a longer tail of the TPSF. Finally, noise on mayonnaise

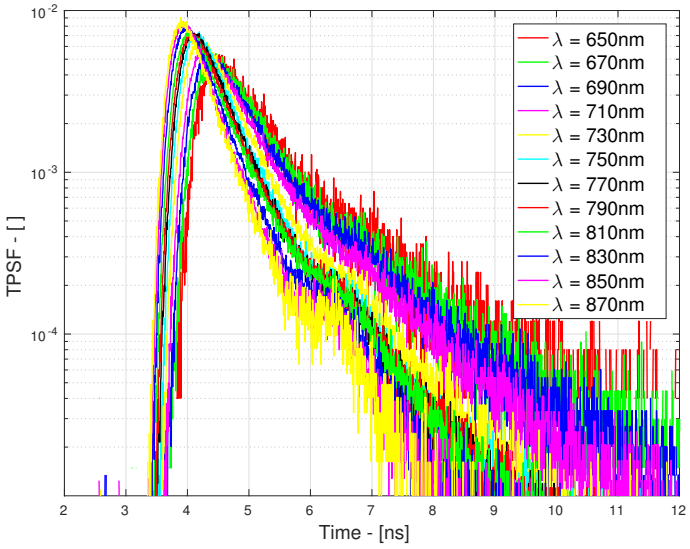

Figure 4.8: Temporal point spread functions from the experiment *Intralipids 1*. TPSFs were obtained at all the wavelengths on the sample made of intralipids at 1% and normalised. The experiment was conducted with a source/detector separation of 16 mm.

experiments remains constant over the different wavelengths.

Table 4.2 shows the SNRs for each TPSF acquired during the experiments where SNR was obtained from equation A.16. Better signal quality is observed in the central wavelengths 690-830nm, while a progressive decay of signal quality is experienced at the outer wavelengths. This trend is expected in relation to the reduced amount of photons counted in the reference measurements. The measurement *Intralipids 4* and *Mayonnaise 4* were acquired with a separation of 28 mm (instead of 16 mm for the other experiments) which improves the SNR at the lower wavelengths in Intralipids 4, while it degrades the signal at higher wavelengths. The effects on mayonnaise appear to be erratic, with an improvement of the signal over the entire spectrum of wavelengths.

Figure 4.10 shows the SNR computed over different portions of the signal. Only the signal from the sample *Intralipids 1* is plotted, but similar trends were observed in all the other experiments. Signals show a higher SNR in the second half of the main peak at all the wavelengths. The minimum SNR

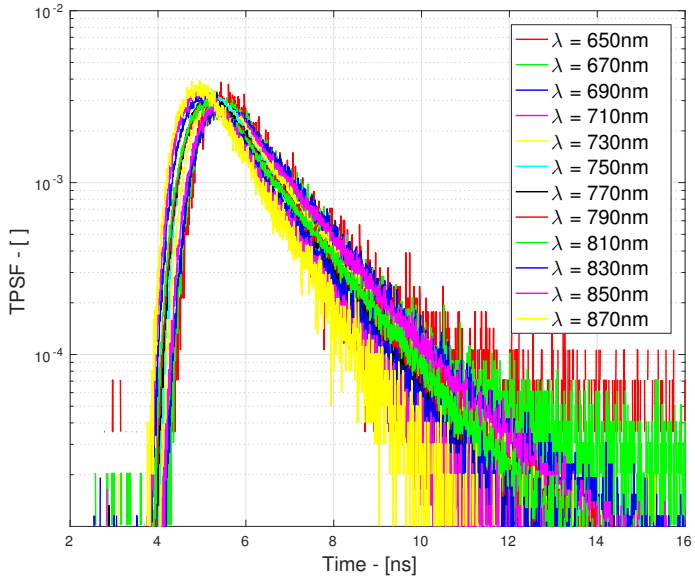

Figure 4.9: Temporal point spread functions from the experiment *Mayonnaise 1*. TPSFs were obtained at all the wavelengths on the sample made of oil-in-water emulsion described in section 3.2.1. The experiment was conducted with a source/detector separation of 16 mm.

are recorded in the first part of the signal, and show a lower SNR at lower wavelengths, where the signal is smaller. Finally, the average level of SNR remains constant above 770 nm.

Figure 4.11 shows the distribution of residuals from *Intalipids 1* experimental signal. The distribution of residuals is Gaussian when signal is sufficiently above the noise level. Where this is not the case, the distribution of residuals shows asymmetries with poor signal, and non-Gaussian distributions show positive value of skew.

4.3.2 Optical experiments on intralipids

Signal fitting

We adopt intralipid emulsions as samples to test the performance of the optical modality. The well-known microstructure of intralipids enables the performances in the characterisation of dimensional features for a novel technique

Wavelengths (nm)	650	670	690	710	730	750	770	790	810	830	850	870
Intralipids 1	2.50	3.68	5.00	6.02	6.10	6.39	6.71	6.35	6.78	6.51	5.68	4.48
Intralipids 2	2.29	3.77	5.46	6.08	6.38	6.46	6.83	6.66	6.53	6.07	6.05	5.01
Intralipids 3	2.25	3.59	5.37	6.14	6.15	6.72	6.69	7.24	6.53	6.42	5.53	4.50
Intralipids 4	4.06	5.65	7.45	7.62	6.25	5.41	5.59	6.36	6.62	4.73	3.80	3.08
Mayonnaise 1	2.47	4.27	6.74	8.01	7.69	7.20	7.67	7.97	7.81	7.02	6.68	4.37
Mayonnaise 2	1.60	2.91	4.96	5.85	5.85	5.61	6.85	7.05	7.16	6.15	5.00	3.13
Mayonnaise 3	1.39	2.62	4.12	5.10	5.16	5.35	5.88	6.09	6.50	5.30	4.32	2.62
Mayonnaise 4	1.86	3.33	5.80	6.58	5.62	5.68	6.53	7.06	7.24	5.87	5.05	3.05

Table 4.2: The values of SNR for the different samples and wavelengths. Average value of SNR computed for each TPSF obtained in each experiment performed during this work. The samples numbered 1–3 were measured with a source/detector distance of 16 mm, while samples numbered 4 had a distance of 28 mm.

to be probed [van Staveren et al., 1991, Flock et al., 1992]. Here, we describe the spectrum of scattering and absorption coefficients, and the evaluation of microstructural parameters.

Figure 4.12 shows the fitting of TPSFs at the different wavelengths for the intralipids experiments. Signals and fitting are visually not distinguishable before the peak and until reflection effects become important. The logarithmic scale highlights that poor fitting occurs only when the noise becomes dominant in the aft part of the tail. Lower wavelengths appear to suffer higher noise which is related to the lower power generated by the laser as shown in figure 4.6. The additional peak between 6-7 ns is progressively marked with the increase of wavelengths suggesting that it is dependent on the spectral properties of the container leading to a reflection phenomenon. Signals presented in this figure are all normalised and difference in magnitude also depend on the effective spread of the TPSF acquired.

Parameters estimation on intralipids

The approach can estimate apparent scattering μ_s', and absorption μ_a, coefficients at wavelengths from 670-870 nm. Here, we present the estimates of the optical properties of the sample and the results leading to the estimation of microstructural features.

Figure 4.13 shows the spectra obtained from the measurements on the three samples of intralipids. Scattering properties show a variation of less than 8% between measurements while absorption spectra present a maxi-

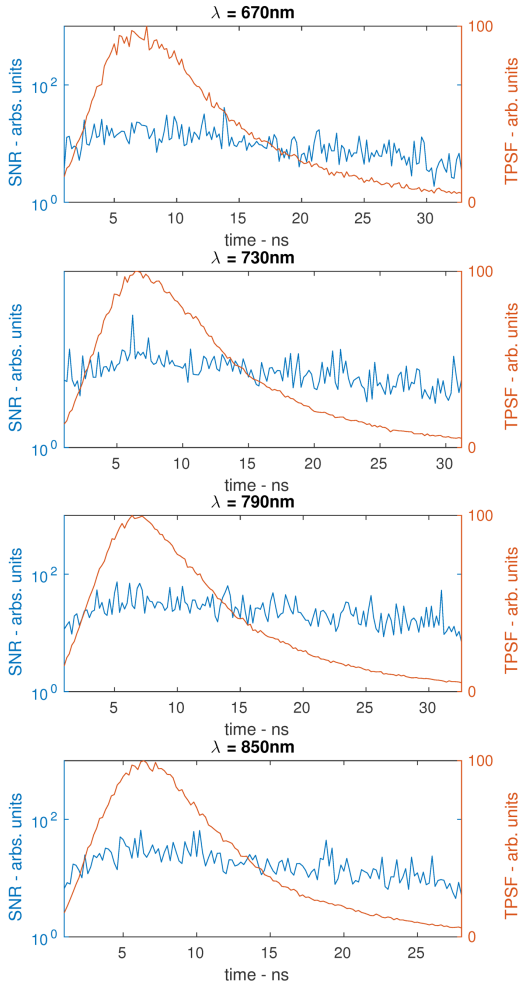

Figure 4.10: Signal noise ratio computed on different windows over a TPSF signal. The signals were obtained from a sample of intralipids at 1%, and all the wavelengths are shown.

mum discrepancy of less than 5%. The maximum discrepancies are located at higher or lower wavelengths where laser outputs are reduced, and SNR becomes lower. Nevertheless, the wavelength of 830 nm shows an unexpected discrepancy which was caused by an artifact in the acquisition of sample *Intralipids 3*.

The fitting of the apparent scattering coefficient spectrum with the optical model is shown in figure 4.14. The fittings are provided for all the size distribution models presented in section 4.2.1, and they all provide a reasonable

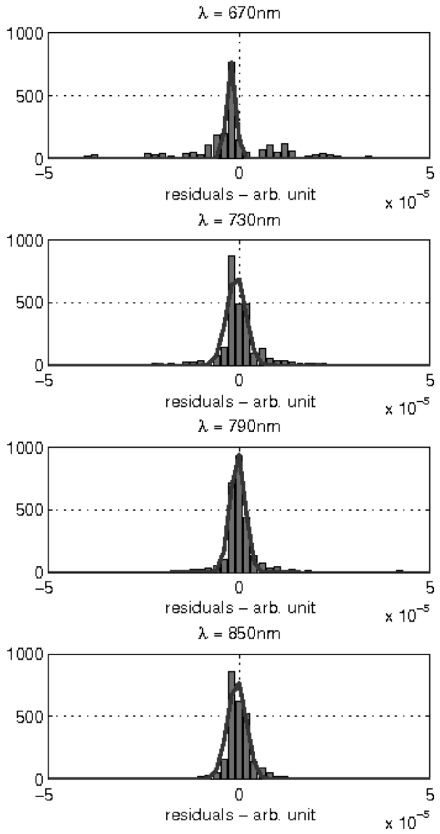

Figure 4.11: Distributions of residuals computed on a selection of the TPSF signals. The signals were obtained from a sample of intralipids at 1%, and all the wavelengths are shown.

fittings of the cloud of points. The similarity between the three fittings is a consequence of the particular case studied. Here, the parameter x (proportional to the ratio between scatterer size and wavelength) is much smaller than 1, and scattering behaviour could be described by Rayleigh scattering in this conditions, despite Mie theory still holds [Ishimaru, 1978]. The variation of the cross section (and of the scattering coefficient) in relation to the wavelength is expected to follow a trend described by $\approx \lambda^{-}4$, which is also followed by the model fitting of the experimental data. Given that a single decay mode exists for all the wavelengths considered, the estimate of the particle sizes becomes strongly related to the information defined *a-priori* on the distribution

Figure 4.12: TPSF fittings of the signal obtained with intralipids at 1% for all the wavelengths. The continuous lines show the signal recorded from experiments while the dash lines represent the best fitting obtained.

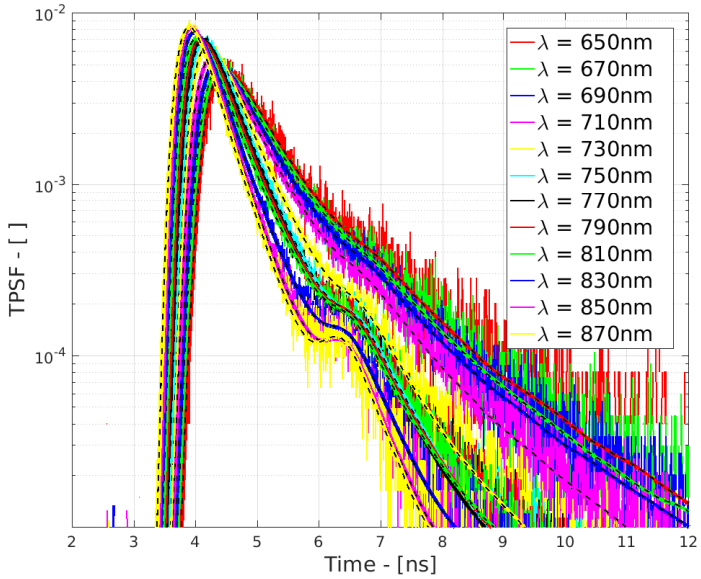

Figure 4.13: Spectra of apparent scattering coefficient (above) and absorption coefficient (below) measured for intralipid samples. Scattering and absorption spectra were estimated from the measurements from the three samples of intralipids diluted at 1%. TPSF signals were fitted separately to obtain the best estimate of optical properties for each wavelength.

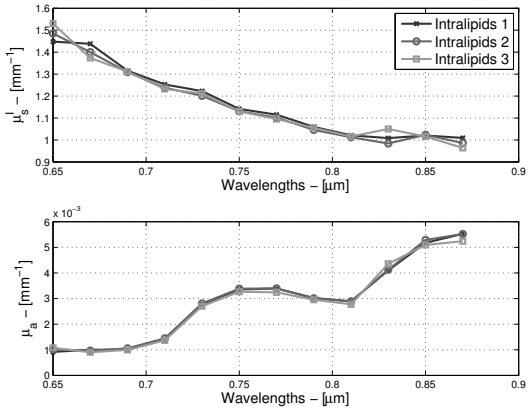

of size of the scatterers. Different distribution choices would fit equally well the signals but provide different estimates.

Table 4.3 complete the previous results with the estimates of microstructural parameters on the intralipid samples. Literature suggests a mean radius of the fat droplets in the microstructure of less than 50 nm for a solution of intralipids at 1%. The expected refractive index ratio is 1.106 [Rotenberg et al., 1991, Michels et al., 2008]. The single radius distribution does not provide a good approximation as the estimate of m is 0.06 points below the expected value, and the lipid concentration ψ of 11.4%. Both the Gaussian and log-normal distribution of sizes models overestimate the parameter m, but they both estimate the concentration with a 20% error. Finally, the Gaussian distribution model is able to predict a radius within 15 nm from the expected value while the log-normal distribution model triples its size.

Figure 4.14: Fitting of the scattering spectrum with the optical model. Three fittings are reported, one for each size distribution illustrated in section 4.2.1 for the sample *Intralipids 1.*

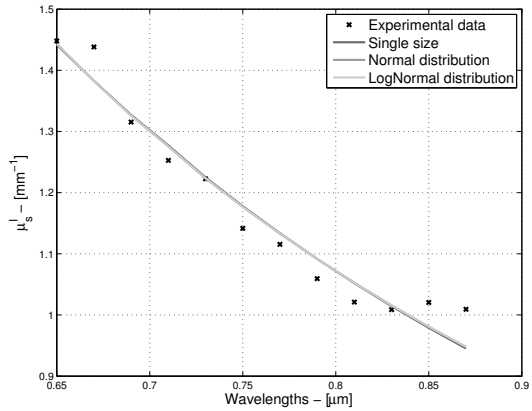

4.3.3 Experiments on emulsions

Optical signal fitting

The experiment performed on oil-in-water emulsions aim to establish the performance of an advanced multimodality approach on a tissue-like sample. In this section, optical data are combined with the dNMR signals presented in the previous chapter to achieve a model not requiring previous knowledge of

	Single	Gaussian	log-normal	Literature
r - [μm]	96(3)	35(2)	168(125)	48.6(1.5) nm.
σ - [μm]	-	32(1)	18(4)	-
m - [ ]	1.044(0.003)	1.162(0.014)	1.141 (0.051)	1.106
ψ - [ ]	0.114(0.024)	0.012(0.002)	0.012(0.002)	-

Table 4.3: Estimates of microstructural parameters of intralipid samples. Single size, Gaussian and log-normal distributions are considered. Mean values across the samples are presented while the standard deviation is reported in brackets. The properties of the intralipid samples obtained from literature were also presented with the error of estimation when available [van Staveren et al., 1991].

parameters. A first section describes the performances of optical modality alone, than the multimodality approach is presented.

Figure 4.15 shows the fitting of equation 2.11 over the TPSFs obtained from sample *Mayonnaise 1*. The signal shows a perfect logarithmic decay of the tail, with no reflection artifacts. The higher scattering coefficient of the emulsion respect to intralipids elongates the tail by about 1.5 ns compared to the TPSFs. The normalisation introduces different value of the background noise counts, leading to non-zero values at increasing times. This bias is particularly observed at 650 nm where the lowest SNR is observed.

Figure 4.16 presents the apparent scattering and absorption spectra obtained from the three emulsion samples. Spectra were obtained by fitting separate TPSFs at each wavelength setting a refractive index $n = 1.40$. The apparent scattering coefficient shows an average increase of scattering with the wavelength, but oscillations are of the same magnitude of the increase. Measurements from the three samples present similar trends, but discrepancies of about 7% between samples can be observed. No dependence on the noise level can be detected above 650 nm, and the three spectra do not intersect.

Figure 4.17 shows the fitting of the apparent scattering coefficients. The scattering spectrum from the sample *Mayonnaise 1* is selected, and the model described in section 4.2.2 is fitted to the signal. The single size distribution model is not able to capture the ascending trend shown by the signal. Both Gaussian and log-normal distributions are able to model the signal more ac-

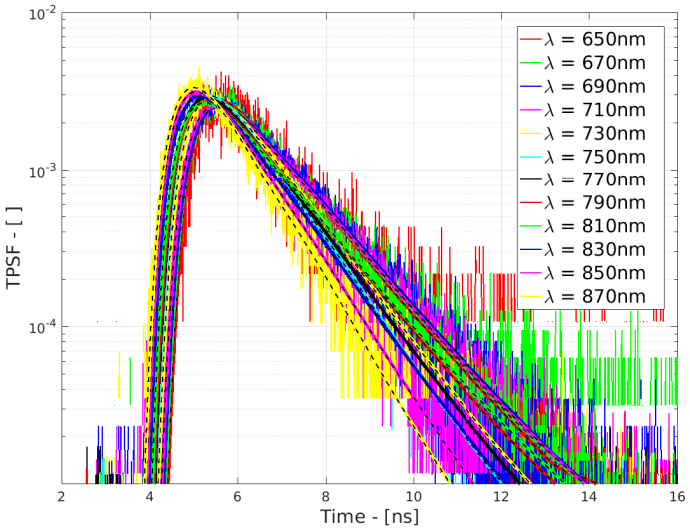

Figure 4.15: TPSF fittings of the signal obtained with water in oil emulsion for all the wavelengths.

Figure 4.16: Spectra of apparent scattering coefficient (above) and absorption coefficient (below)

measured for oil in water emulsion samples. Scattering and absorption spectra were estimated from the measurements from the three samples of mayonnaise. TPSF signals were fitted separately to obtain the best estimate of optical properties for each wavelength.

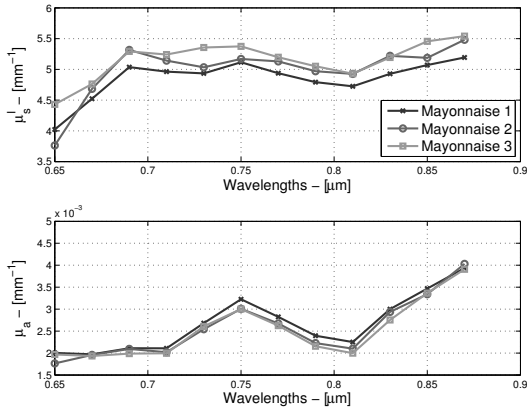

curately, but the oscillations are not captured in their full dynamics. The oscillations in the apparent scattering coefficient measured in the experiments are generated by the presence of a large number of scatterers with a specific

dimension. Mie theory shows that the scattering from a population of scatterers with a single size could produce sinusoidal oscillations with the variation of the wavelength. The presence of different scatterers with different dimensions could attenuate the oscillations. Here, a continuous distribution of scatterers generates a smooth signal unable to fit the large oscillations observed in the experiments. Attempts were made to fit a distribution of scatterer sizes composed of two populations of particles at a single radius. The model becomes difficult to fit and lacks in representing a smooth signal in the largest part of the spectrum as a consequence of the absence of a continuous distribution of sizes. It is understood that the absence in capturing the oscillations might lead to ignoring a significant property of the sample, but it does not appear feasible with the level of understanding of the problem.

Figure 4.17: Fitting of the optical model on the scattering spectrum. Three fittings are reported, one for each size distribution illustrated in section 4.2.1 for the sample *Mayonnaise 1*.

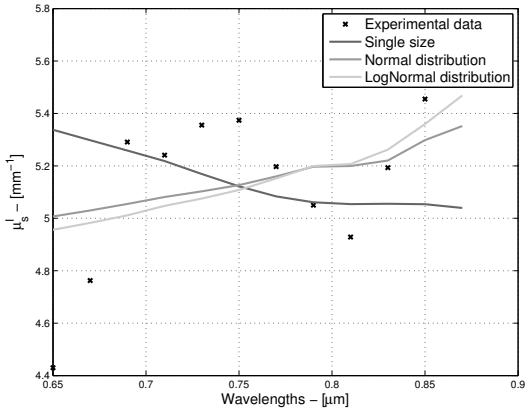

Figure 4.18 shows the MCMC chains obtained by fitting the spectra from oil-in-water emulsions with the optical model only. The estimated value of r is similar between samples, but larger variations can be observed over the estimates of size distribution spread σ. The chain of solutions for r show that 50% of the solutions are contained in a variation of 3.26 μm in sample *Mayonnaise 3*. Estimates of σ present larger variations in the sample *Mayonnaise 1* where the chain amplitude is 3.63 μm. All the chain of solutions for the parameter r are compatible with the CLSM investigation (see table 3.5), but only sam-

ples *Mayonnaise 2* and *Mayonnaise 3* show MCMC solutions compatible with CLSM value of σ. Conversely, all the estimates of ψ are biased compared to the expected volume fraction of the sample.

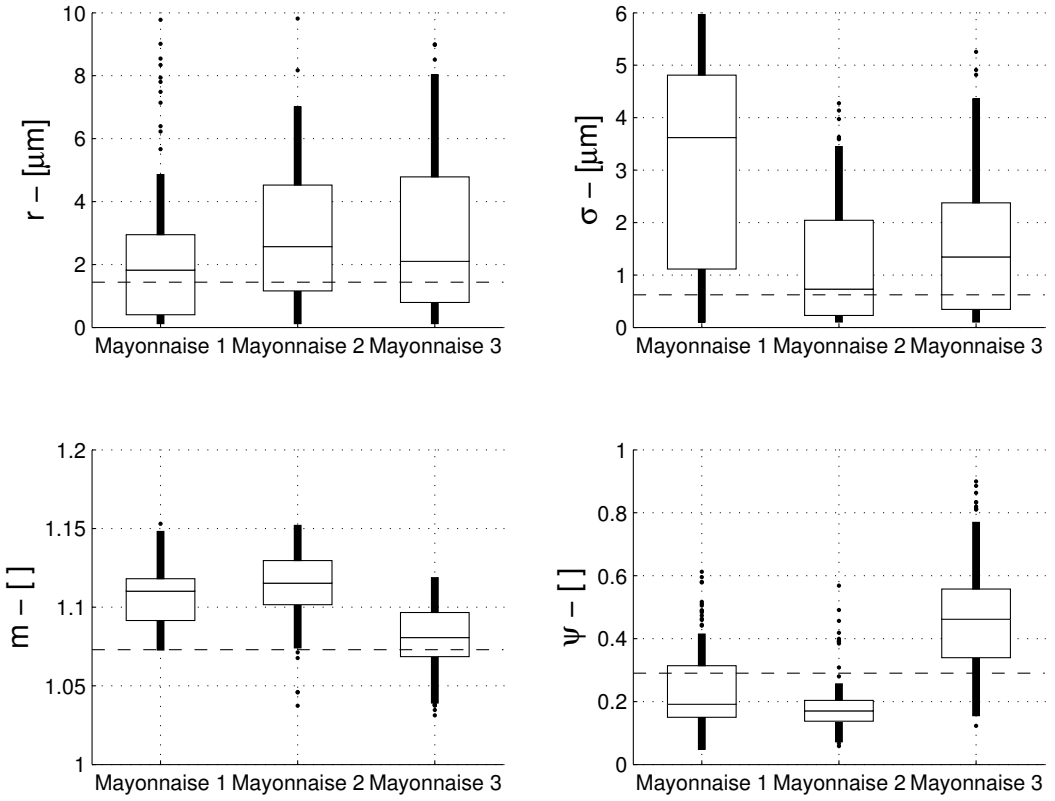

Figure 4.18: The boxplots show the MCMC chains of the microstructural estimates (r,σ,m,ψ) obtained from the optical modality only. Here, the chain are shown excluding their 2,500 solutions burn in phase for the first 5,000 solutions. Dash lines represent the expected values of the parameter defined by CLSM or known chemical composition.

Diffusion NMR signal fitting

The work presented in this section was conducted on the same type of samples adopted in the work presented in chapter 3. The previous dNMR measurements were adopted in this part of the work to provide the dNMR signals.

The acquisition of dNMR signals on intralipids might present a problem due to the mobility of the droplets during long scanning sessions. Works were

conducted in the past on similar problems, where the size of the distribution of droplets within an emulsion was estimated [Hollingsworth and Johns, 2003a, Denkova et al., 2004]. A recurrent problem is the deposition of the droplets as a consequence of the difference in density from the medium. A system capable of producing a constant stirring of the emulsion is required to maintain a good distribution of signal across the sample. Such system was not available and the scanner adopted required a setup time during which the droplets separated. As a consequence, the work on intralipids was adopted for the validation of the optical technique only.

The dNMR measurements providing the results discussed in section 3.3.3 were used in this work. The raw data and the fitting were presented in figure 3.5(b). It should be recognised that the same sample should have been used for both the DOS and dNMR experiments. Nevertheless, the specific emulsion in this work was used because of the standardisation under which the sample was produced. It was considered disproportionate to obtain further measurements given the persistent inability to use the same sample for both the modalities. As a consequence, the single measurements adopted in the previous document were then utilised for a combined modality with the three DOS acquisitions.

4.3.4 Multimodality approach

Signal fitting

The combination of dNMR and a multi-wavelength approach redesigns the approach to the characterisation of microstructural features. The absence of a-priori known parameters as in the previous chapter enables a more extensive application of the approach. Here, we adopt the dNMR approach and data presented in section 3.2.2 and incorporate the information from multi-wavelengths optical data.

Figure 4.19 shows the fitting of signals with the optical model applied in the multimodality approach. The fitting of the apparent scattering spectrum and the echo NMR attenuation are shown with a fitting model adopting a log-normal distribution of sizes. The dNMR signal is noisy, but a clear fitting is observed, spanning over the whole amplitude of the signal. On the opposite,

the optical signal does not have a high level of noise, but the fitting is shifted from the data in the first part of the spectrum.

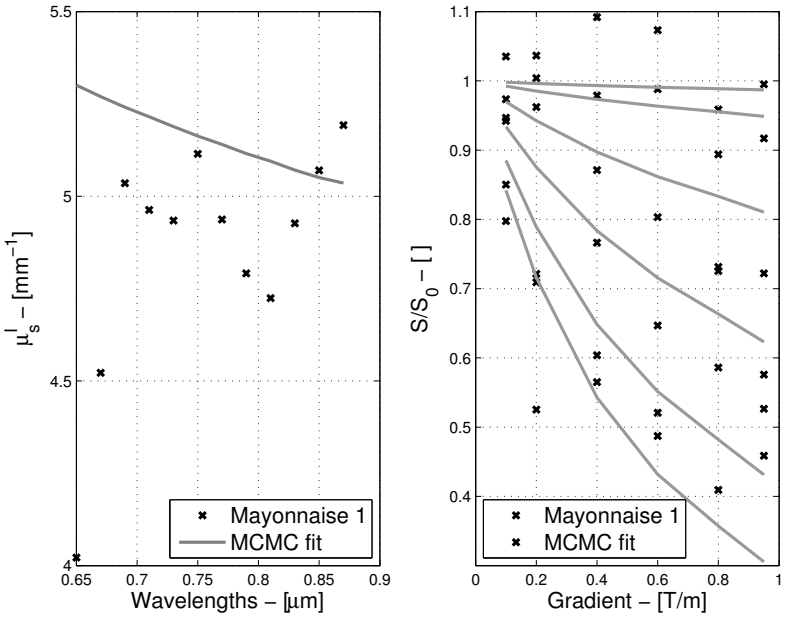

Figure 4.19: Fitting of the experimental data with the multimodality approach. The fitting performed with the log-normal distribution is presented for the sample *Mayonnaise 1*, and both optical and dNMR signals are shown.

Monte Carlo Markov Chain analysis

Figure 4.20 presents the MCMC boxplots obtained from the fitting of the combined model on the data. Data are presented for the four microstructural variables: r, σ, ψ, and m. The estimates of average radius are all compatible with CLSM values despite MCMC chain for sample *Mayonnaise 3* shows a trend to overestimation the parameter. Similarly, the estimates of σ present the same features. Finally, the volume fraction MCMC chain of the samples present a good agreement to the expected value. The amplitude of MCMC chains are considerably reduced by the use of a multimodality approach by at least 45% in the estimation of r, and 37% in the estimation of σ.

Figure 4.21 presents the MCMC chains obtained from the fitting of the combined model on the data. The two chains related to the dimensional prop-

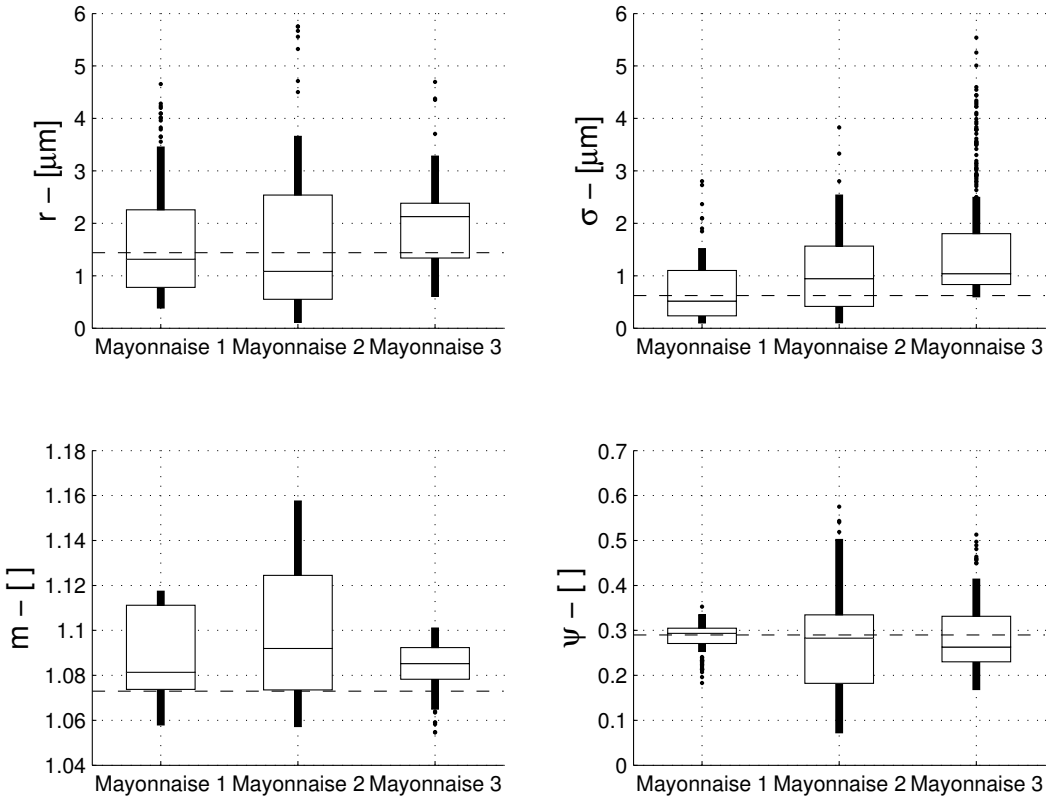

Figure 4.20: Monte Carlo Markov Chain boxplot shows the microstructural estimates of the three samples. MCMC chains were generated using the multimodality approach, and they are made of 5,000 solutions (r, σ, m, and ψ). Dash lines represent the expected values of the parameter defined by CLSM or known chemical composition.

erties of the microstructure (r and σ) present correlated oscillations over the entire set of solutions. An increase in the estimate of r leads to a decrease of σ, expected as they both contribute to the definition of the size distribution. Diffusivity varies over an order of magnitude and the trend also appears related to the microstructural variables.

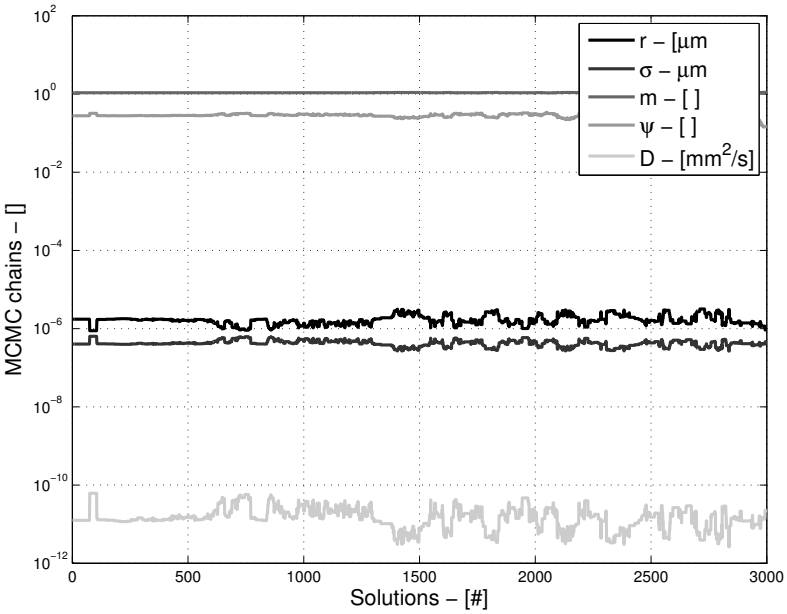

Figure 4.21: Monte Carlo Markov Chains for the sample *Mayonnaise 1*. MCMC chains were generated using the multimodality approach, and they are composed of 2,000 solutions for each parameter.

4.4 Discussion

4.4.1 Validation of the optical modality

The signal expected from intralipids is dominated by scattering [Flock et al., 1992]. The droplets have a dimension in the order of the hundreds of nanometres, and for a concentration of 1%, 90% of the droplets are below 150 nm [Rotenberg et al., 1991, van Staveren et al., 1991]. Intralipids are microstructurally controlled, and stable in time because of their primary pharmacological applications [Michels et al., 2008].

The results show a good reproducibility of measurements between intralipid samples. Both scattering and absorption properties remain within 5% difference between samples where the discrepancies could be related to the noise level in the signals. The fitting of TPSF signals with the model presented in the previous chapter demonstrates that the physics of the problem at all the wavelengths. The scattering spectrum follows the expected exponential decay,

and the magnitude of the coefficient is compatible with the values reported in literature [Michels et al., 2008]. The absorption coefficients measured in the experiments match the values reported in literature for solutions of intralipids at 10% despite the actual solution is at 1% [Michels et al., 2008]. These values could be explained by the similar absorption properties of the two phases which results in a spectrum similar to water's.

The fitting of microstructural model over the scattering spectrum is performed with three size distributions. The spectra from single size and normally distributed size particles are not visually distinguishable, but provide different estimates. The choice of the appropriate model of the microstructure appears fundamental as it characterises the relation between spectrum and microstructure. Single size distribution should be rejected as it does not capture the physics and overestimates the dimension by about 30%. Gaussian distribution estimates the expected distribution. The approach does not require any prior knowledge of optical parameter of the compartment, which is a significant advantage compared to the methods presented in the previous chapter.

4.4.2 Optical modality and multimodality fitting

The emulsion utilised in this work has been previously characterised in section 3.2.5. The presence of a tissue-like microstructure enables the performances of the approach to be tested. Neither the single modality optical technique nor the multimodality technique require known parameters a-priori.

The scattering spectra obtained from the three samples show discrepancies. The presence of a complex microstructure which can present a degree of inhomogeneity may explain the differences between samples. The discrepancies can be observed in the estimation of microstructure which vary over 93% for the value of r regarding *Mayonnaise 3*. Similarly, the difference between the value of σ between sample *Mayonnaise 1* and sample *Mayonnaise 3* is of $0.52\,\mu$m. These discrepancies can be related to the differences between samples, but the amplitude of MCMC chains shows that differences between samples is not statistically significant.

The model presented does not perform equally well as on intralipids. The

oscillations of the spectrum are not captured by the model, as a result of a continuous distribution of sizes considered. The single size distribution model is not able to capture the physics of the spectrum as the model is forced to decrease with the wavelength while the signal increases. The Gaussian and log-normal distributions return different fittings as a result of the structure of the signal which relates to the tails of the distributions.

The multimodality approach improves the accuracy of estimates as shown in figures 4.18 and 4.20. The fittings of the signals from each modality with a multimodality approach show a large discrepancy from experimental results. This is related to the combination of the information from the two modalities which leads to a fitting accounting for the two physics at the same time. Only the multimodality approach is able to produce accurate fittings of the volume fraction showing the fundamental contribution from dNMR signal. Finally, the specificity of the multimodality model is superior as in could be observed by the stability of MCMC chains and by the realistic estimates.

4.4.3 Merits of the two individual approaches and their combination

The DOS and dNMR techniques were selected for this work as a result of the following arguments. The DOS provides a robust approach to determine the optical scattering properties of a sample in the vis-NIR spectrum, and enables reduced sensitivity on the calibration of the experimental setup. Although the signal deconvolution between the calibration TPSF and the signal might present marginal difficulties, the experiments are reproducible. Finally, the parameters required a-priori minimally affect the result, offering a suite for a complete estimation of the properties of the sample.

The advantages of the dNMR techniques have been discussed in section 3.4. dNMR can separate the spectral peaks of water and oil, allowing for an isolation of the signal from the oil phase confined in the droplets. The low diffusivity requires a large diffusion time which can be achieved with a SE. The SE sequences are sensitive to the alignment of the RF pulses and the risk of recording imperfect echoes exists. Nevertheless, in the experiments a set of

echoes was recorded offering a clean signal (SNR = 83) on which the model could be fitted.

Both the techniques rely on the homogeneity of the sample. Despite they could be modified to obtain a spatial discretisation, DOS maximum resolution would be limited to a tenth of a millimetre, and the approach will always be restricted to scattering dominated problems. Conversely, dNMR technique can be converted to a Diffusion MR Imaging (dMRI) technique to obtain better resolution, and to obtain the information estimated on the bulk sample at the voxel level if SNR is sufficiently high.

The decision to adopt the described emulsion in this work arises from the necessity to obtain stable or reproducible samples which are suitable for both DOS and dNMR investigation which were carried on at different times. The difficulty in the selection of the sample resides in the necessity to obtain a dNMR signal from the diffusion of spins contained inside the particles and to obtain an optical signal from the scattering. Standard optical samples with a stable and simple distribution of scatterers (i.e. intralipids or calibrated beads) either do not remain stable in time, or do not offer a diffusion MR signal.

The combination of the two techniques offer a means to obtain repeatable signals in both the modalities. Additionally, the number of parameters in common between the two models to be estimated is maximised, and a limited set of prior information or parameters are required a-priori. Unfortunately, the complexity of the microstructure seems not to be captured in the optical modality, suggesting that a simpler sample might be required.

The two techniques are ideal for a study case as discussed in this chapter, aiming to prove the feasibility of the combination of two techniques. The principle connecting signals to the sample microstructure in both DOS and dNMR can be extrapolated and integrated in many other techniques. Evolution of both is discussed in chapter 5 and chapter 6 respectively for diffusion MR and optical techniques. Nevertheless, the direct application in clinical practice of the combination of DOS and dNMR is hard to foresee. The complexity of pathologies altering the microstructural properties of the tissue, and their connection to the anatomy of the body itself, precludes in-vivo applications as a consequence of the lack of homogeneity in the sample. Even a possible

extension to laboratory investigation of excises tumour masses is unlikely due to the heterogeneity of cancer lesions themselves. The needs for a higher resolution is also present to distinguish between different parts of the same tissue and to apply the most appropriate microstructural model to each of them. An additional limitation to in-vivo applications of DOS is the dependence on absorption which might become relevant in specific tissues and limit the validity of the approach.

4.5 Conclusion

The combination of techniques not requiring a-priori knowledge of parameters offers an increase of the accuracy of the estimates. Along with that, the absence of prior knowledge of the sample reduces the specificity of the model to the signal. The approach presented in this section is general, and any two techniques able to predict correlated microstructural features can be utilised.

This second demonstration of the benefits of a multimodality approach for estimating microstructural material features suggests a full feasibility of application on biological tissue where no prior knowledge could be required. This is a further step toward multimodal microstructure imaging and non-invasive histology.

Part III

Investigation on cancer

Chapter 5

Diffusion MRI investigation of microstructure in colorectal cancer cell lines

5.1 Introduction

Investigation of tissue microstructure with non-invasive histology is a developing research area. Magnetic resonance imaging has been utilised to detect anatomical features and pathological conditions in human body. Diffusion MRI estimates water diffusion within the microstructure of the sample, and consequently offers an additional contrast mechanism to detect acute pathologies such as ischemia, or chronic pathologies such as Alzheimer's disease [Moseley et al., 1990, Does et al., 2003, Rose et al., 2000]. The main field of application of diffusion MRI is the description of brain microstructure, and white and grey matter MR signals have been characterised by many studies [Basser and Pierpaoli, 1996, Assaf and Basser, 2005, Alexander et al., 2007, Shemesh et al., 2009, Zhang et al., 2012]. Another diffusion MRI applications is the diagnosis and staging of tumour lesions and their reaction to treatment [Koh and Collins, 2007, Colvin et al., 2011, Panagiotaki et al., 2014].

A step forward consists in the staging of lesions using direct estimates of microstructural features instead of generic indicators (i.e. ADC, MD, FA).

So far, the majority of researcher utilised data acquired with pulsed gradient spin echo to describe the microstructure. Recently, oscillating gradient spin echo sequences suggest to be able to probe smaller compartments better than PGSE [Does et al., 2003, Colvin et al., 2011, Drobnjak and Alexander, 2011]. Along the work on gradient sequence characterisation, the fitting of MR signals with microstructure specific models became equally relevant, and works have been presented describing different tissues [Panagiotaki et al., 2012, Xu et al., 2009b].

The present work aims to characterise signal models designed to fit diffusion MRI (dMRI) measurements acquired with oscillating gradients. We aim to identify a relation between compartment dimension and oscillation frequency, and to rank the performance of models describing the signal in relation to microstructual elements. Finally a comparison between the estimates from the best model and histological measurements will be conducted on two tumour cell lines grown in xenograft tumours.

5.2 Methods

5.2.1 The problem

Here, we consider xenograft tumours which are biological tissues presenting all the microstructural features of a human colorectal tumour. Three main components can be observed: the nuclei (and organelles), the cytoplasm, and the extracellular collagen. The tissue presents other components such as vasculature, but they are not considered in the models presented in this work. The objective is to rank different signal models in their ability to represent the signal generated by Oscillating Gradient Spin Echo sequences applied on *ex-vivo* xenograft tumours. Additionally, the ability to estimate microstructural such as nuclei size, r, cell size, R, and volume fraction, ψ is also discussed.

The samples

This work utilises two cell lines of xenograft tumours to mimic colorectal tumours. Xenograft tumours are cell cultures grown in a hosting body. Cells are

injected and the culture develops as a compact blob with well defined boundaries, but complete vascular structures can also be observed [Leunig et al., 1992]. Xenograft tumours present a different microstructure from human or animal tumours, as they are generally more dense with a different packing of cells. Nevertheless, they are superior to cultures in matrix or in-vitro and offer a good benchmark to test new modalities.

We adopted two cell lines developing different microstructures. All experiments were performed in accordance with the local ethical review panel, the UK Home Office Animals Scientific Procedures Act 1986, and United Kingdom Co-ordinating Committee on Cancer Research guidelines [Workman et al., 2010]. The first cell line is LS174T (samples indicated as *LS1*, *LS2*, and *LS3*) cell line which shows a well differentiated microstructure, the second is SW1222 (samples indicated as *SW1*, *SW2*, and *SW3*) which develops a glandular microstructure. This study is performed on 6 fixed subcutaneous xenograft tumour samples grown in nude mice: 3 from LS, and 3 from SW cell lines. Mice were sacrified after 7 weeks from the injection of tumour cells and immediately fixated in PFA 4%. Tumours were preserved in-body and exised (1-year) after the sacrifice [Skaer and Whytock, 1976, Fox et al., 1985, Augusteyn et al., 2008].

LS174T The cell line LS174T is a human epithelial cell line. This cell line develops in adenocarcinomas in colorectal epithelium, but when implanted in nude mice they can be grown as xenograft masses. The properties of the microstructure vary if grown in nude mice or collagen gels [Richman and Bodmer, 1988,Fukamachi and Kim, 1989]. LS174T xenografts microstructure does not present glandular differentiation as shown in figure 5.1. Cells are packed in solid cords with numerous signet ring forms. Only xenograft cultures of LS174T cell lines are able to develop a regular microstructure, as colonies in collagen matrix or gels present small aggregates rather than a continuous packing [Richman and Bodmer, 1988]. The blood vessels grow in an organised structure with a capillary density of about 2/3 of the value expected in a striated muscle [Leunig et al., 1992].

SW1222 Cell line SW1222 is a human epithelial cell line. This cell line can be found in different organs of the human body as it is an epithelial cell line. In xenograft tumours the cells the microstructure is characterised by a gland-like structures which can be considered similar to non-pathologic colorectal crypts. The cells show a well-defined polarity and nuclear pleomorphism. The use of xenograft culture instead of collagen matrices tends to provide an increased order to the packing of the cells increasing the size of glands central lumen [Richman and Bodmer, 1988]. The vasculature presents an high tortuosity which is principally due to the glandular structure [Leunig et al., 1992]. Extracellular collagen is also aligned to the glandular rings and consequently to the vasculature.

5.2.2 Data acquisition

Oscillating gradient sequences

The sequence of magnetic field gradients determines the ability of the modality to detect microstructural diffusion. The change in contrast is determined by the position and intensity of gradients in time which is responsible to introduce phase shift in the spin depending on the diffusion pattern.

The experiments aim to prove the specificity to microstructural features of

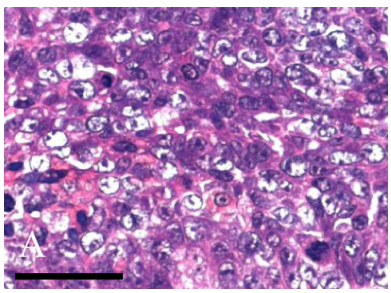

Figure 5.1: Image showing an histological investigation on a LS174T cell line. The image shows the microstructure from one of the xenograft tumours just after the sacrifice of the animal. Optical microscopy with haematoxylin and eosin stain was used to highlight the microstructure. The poorly differentiated microstructure shows the presence of enlarged nuclei in a densely packed structure of cells. (Image courtesy of Dr E. Panagiotaki)

the signals obtained with different parameters of the sequences. In this work we concentrated on two oscillating gradient spin echo sequences. The idea is to characterise the performances of the two families of gradient profiles: a repetition of square lobes, and a sinusoidal shape. The sequences considered are:

- Cosine Wave Oscillating Gradient Spin Echo (CW-OGSE) presented in figure 5.3;
- Square Wave Oscillating Gradient Spin Echo (SW-OGSE) presented in figure 5.4.

Cosine Wave Oscillating Gradient Spin Echo is based on the repetition of sinusoidal lobes. The sequence begins with a fully on gradient and the frequency, f, is the frequency of the sinusoid. The strength of the gradient G, is the intensity of the gradient at the peak, and the echo time TE is the time at which the readout protocols begins the echo acquisition.

Cosine Wave Oscillating Gradient Spin Echo is based on the repetition of square lobes. The sequence alternates fully on gradients in opposite directions, and the frequency f, is related to the full period. The gradient G, becomes the only theoretical magnitude assumed by the gradient, and the echo time TE is identical to the CW-OGSE case.

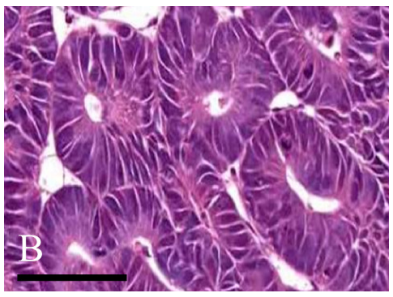

Figure 5.2: Image showing an histological investigation on a SW1222 cell line. The image shows the microstructure from one of the xenograft tumours just after the sacrifice of the animal. Optical microscopy with haematoxylin and eosin stain was used to highlight the microstructure. The highly differentiated microstructure shows the presence of enlarged nuclei, and the cells form a glandular microstructure with the presence of a large lumen around which they are aligned. (Image courtesy of Dr E. Panagiotaki)

The experiment presented aims to provide a wide characterisation of OGSE models. Frequencies and gradients were combined from a large range of values

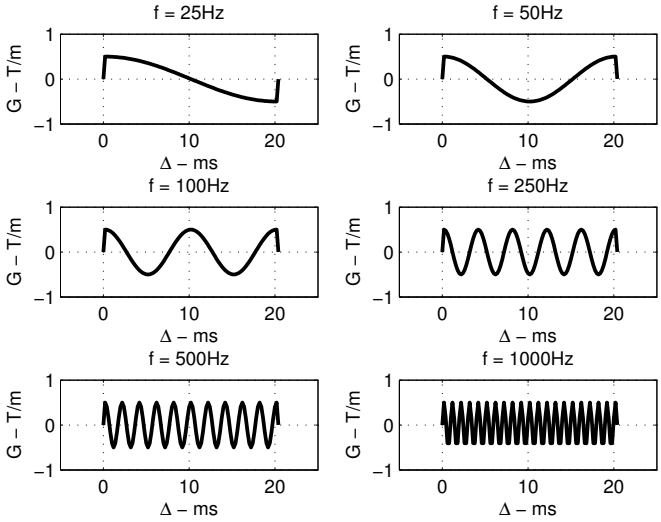

Figure 5.3: Gradient scheme for the CW-OGSE. Gradients and RF pulses are reported with all the definitions of physical parameters describing the sequence.

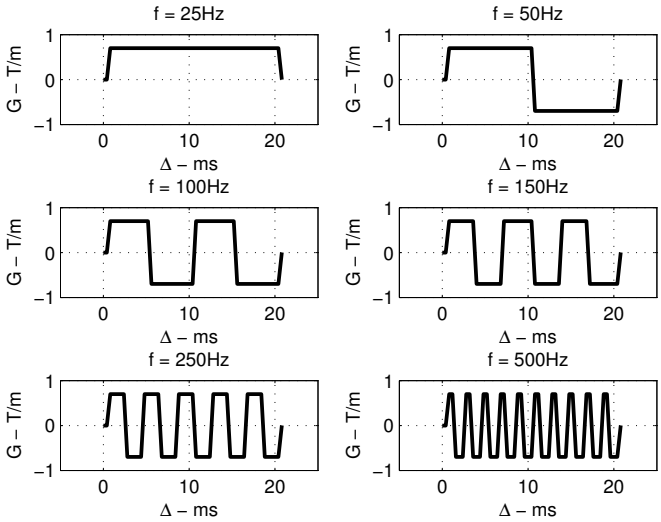

Figure 5.4: Gradient scheme for the SW-OGSE. Gradients and RF pulses are reported with all the definitions of physical parameters describing the sequence.

Frequency Hz	CW-OGSE - s/m^2	SW-OGSE - s/m^2
25	14,502	257,163
50	3,625	46,757
100	906	1,1689
150	-	5,195
250	145	1,870
500	36	467
1,000	9	-

Table 5.1: b-values at each frequency obtained with the maximum intensity of gradient applied. Values have been computed for Cosine Wage OGSE, and Square Wave OGSE with the equations presented in table 2.1.

to provide the ground for a full description of the physics. For the sequence CW-OGSE, G were selected at 0, 0.05, 0.1, 0.15, 0.2, 0.25, 0.3, 0.5 T/m, and frequencies were 25, 50, 100, 250, 500, and 1,000 Hz. For SW-OGSE, G are 0, 0.05, 0.1, 0.15, 0.2, 0.3, 0.4, 0.5, 0.7 T/m and the frequencies were 25, 50, 100, 150, 250, and 500 Hz. The echo time is constant over all the measurement to avoid a bias due to T2 decay.

The b-values reached by the sequences have been reported in table 5.1. It is self-evident that the maximum b-value obtained with a Square Wave OGSE is about two order of magnitude from the values utilised in current clinical applications. The specific sequence corresponds to a PGSE with a gradient duration of 20 ms, and gradient intensity of 0.7 T/m. Nevertheless, higher frequencies present lower b-values comparable to clinical applications, despite they were obtained with higher gradient strengths. Figure 5.5 shows also the comparison between the Square Wave OGSE and a Trapezoid Wave OGSE obtained with the specifications of the system. The system limitations are able to reduce the b-value of 15% in the worst case as the period becomes comparable to the ramp time.

System preparation

In this work, a 9.4T Agilent system was adopted. This is the pre-clinical scanner in service at the Centre for Advanced Biomedical Imaging (UCL), and it is designed for pre-clinical/animal experiments with a small bore, able to

fit different coils. Coils for different purposes can be installed with a 20min procedure. For the experiments described a coil allowing for a $20\phi x 20mm^2$ field view was installed. Gradient up to 1T/m in the three directions can be achieved with a ramp time of 0.2 ms. The pre-clinical nature of the system offers great versatility, but requires a preliminary calibration and performance tests. Such steps are required to adjust the interactions between the sample and the system and to validate the performances.

Samples were placed in a MRI invisible plastic container. Samples were rehydrated using PBS (Phosphate Buffet Solution) for 72h, then wrapped in gauze and fitted in the container. Each sample was marked with suture thread plastic sticks were placed to offer reference in the scanning images. The container was then filled with Formblyn ^{TM} and all the air bubbles extracted from the sample region to avoid susceptibility.

The sample was placed in the coil. The centre of the sample must match the reference line indicating the section with the maximum homogeneity of the magnetic field. The deterioration of the homogeneity in magnetic field occurs

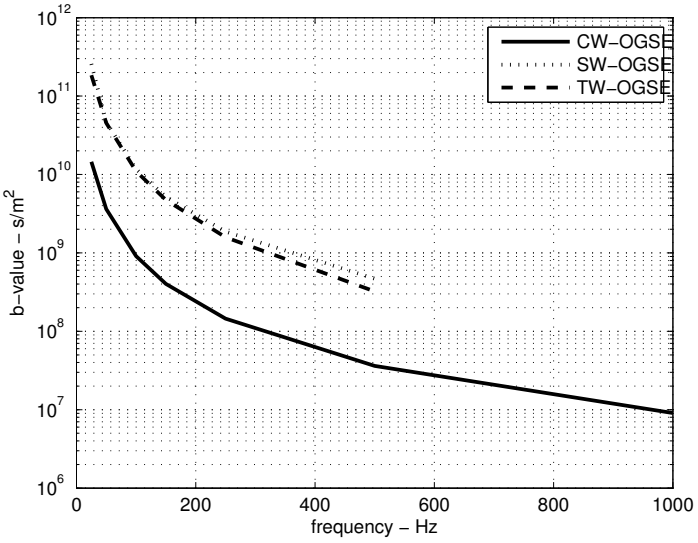

Figure 5.5: b-values at each frequency obtained with the maximum intensity of gradient applied. The figure shows Cosine Wave OGSE, Square Wave OGSE, but also a Trapezoid Wave OGSE obtained with the specifications of the experimental system.

around 15 mm in each directions from the reference line; therefore, the samples should have smaller dimensions to remain in the Field of View (FOV) to avoid artifacts in the signal. Once the internal part of the coil is placed in the magnet, the RF waves are aligned with a multimeter through the appropriate trimmers. To correct for field inhomogeneity due to the sample susceptibility, a shimming is performed. The system enables for the manual correction of magnetic field along three primary axes, three cross axes tunings, and a set of other four, second order corrections.

Imaging protocol

The slice plan is defined over a proton density image, acquired at high resolution (125x125 μm) with a slice separation of 1 mm. From this images, a slice plan was designed to cover the sample with slices separated by 1.5 mm and made of 64x64 pixels over a 16x16 mm^2. To reduce preparation and scanning time, more samples were acquired at the same time with 7 to 12 slices per experiment, depending on number and size of the samples.

Diffusion weighted sequences were programmed in the scanner. Gradient profiles containing the number of lobes, and the diffusion timing are provided through a data file. Direction and intensity of the gradients were set with the internal options of the control software. Four $b0$ acquisitions were performed for each frequency by setting to zero the gradient intensity, at the beginning, in the middle and at the end of the sequence of 28 acquisitions (7 in 3 directions plus null). Acquisition for each frequency were conducted in sequence, from lower to higher frequencies, leaving the larger duty cycles at the beginning. Sample temperature is controlled with a temperature probe, recording a stable temperature within 2 °C above room temperature.

Acquisitions were performed for cosine and square wave with the parameter described in section 5.2.2 and table 5.2. The system has a slew rate below 0.2 μs/T and the real sequences complies with it. The diffusion time Δ, was fixed at 26 ms, the echo time TE, at 42 ms, and the gradient was applied for, δ, 20 ms. Finally a DTI acquisition with 42 directions with a single shell at a b-value of 400 mm^2/s was performed. The acquisitions of each frequency

G (T/m)	CW-OGSE	SW-OGSE	f (Hz)	CW-OGSE	SW-OGSE
0	x	x	25	x	x
0.05	x	x	50	x	x
0.10	x	x	100	x	x
0.15	x	x	150	-	x
0.20	x	x	250	x	x
0.25	x	-	500	x	x
0.30	x	x	1000	x	-
0.40	-	x			
0.50	x	x			
0.70	-	x			

Table 5.2: Table summarising the parameters adopted for each sequence. Gradient intensities G, and frequencies f are reported for each sequence, and all the combinations were acquired.

lasted 26 minutes, and DTI 32 minutes. The total acquisition time is below 4 hours, but the time to prepare and dismiss the scanner raises 6h.

5.2.3 Signal models

The signal from a diffusion MRI experiment offers an insight on the diffusion patterns in the microstructure. The signal depends on the intrinsic diffusion properties of the molecules such as the diffusivity D, and on the barriers to the diffusion imposed by microstructural elements such as cell membranes. Basic signal models have been presented in the sections 2.2.2 and 2.2.3. Only symmetric compartment models discussed in section 2.2.3 have been considered at this stage of the analysis. They are:

- **Ball**: isotropic free diffusion leading to an exponential echo attenuation identical for all the gradient directions;
- **Sphere**: isotropic diffusion confined in a spherical impermeable compartment;
- **Distribution of Spheres**: isotropic diffusion confined in an ensemble of spherical impermeable compartments with a distribution of dimensions;

- **Spherical Shell**: isotropic diffusion confined in an impermeable spherical shell compartment.

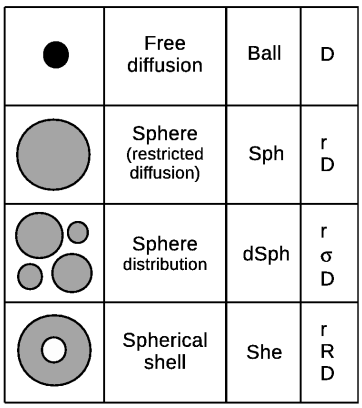

Figure 5.6: Models of diffusion MR signal.

In this analysis we consider eight models which are combinations of the basic models previously described. Three are not directly related to microstructural features, and five model the microstructure with the introduction of explicit geometric compartments as detailed in table 5.3. Structure-unrelated models are:

- **Mono-Exp**: Mono-Exponential echo decay is identical to the Ball model, represent a population of spins with an unique diffusivity;
- **Bi-Exp**: Bi-Exponential echo decay models two populations of spins free to diffuse, which is the simplest representation of two compartments;
- **Tri-Exp**: Tri-Exponential echo decay models three populations of spins free to diffuse, which is the simplest representation of three compartments;

while structure-related models are:

- **Sph+Ball**: Sphere + Ball is the combination of a Sphere compartment representing cells with identical size, and a Ball compartment representing the water molecules outside the cells;

Model	Compartments	Parameters	# par.
Mono-Exp	1 ball	D_1	1
Bi-Exp	2 ball	D_1, D_2, ψ	3
Tri-Exp	2 ball	D_1, D_2, D_3, ψ_1, ψ_2	5
Sph+Ball	1 sphere, 1 ball	D_1, D_2, r, ψ	4
NormSph + Ball	1 sphere, 1 ball	r, σ, D_1, D_2, ψ	5
LognSph + Ball	1 sphere, 1 ball	r, σ, D_1, D_2, ψ	5
Sph + Sph + Ball	2 sphere, 1 ball	r, R, D_1, D_2, D_3, ψ	6
She + Sph + Ball	1 sphere, 1 shell, 1 ball	r, R, D_1, D_2, D_3, ψ	6

Table 5.3: Table summarising the models of signal considered. In the upper part, structure-unrelated models are considered while the lower part shows structure-related models. Description of compartments, name and number of free parameters are reported as well as the name of the model.

- **NormSph + Ball**: Normal Distribution of Spheres + Ball mimics cells with a normally distributed size, and an extracellular compartment where free diffusion occurs;
- **LognSph + Ball**: LogNormal Distribution of Spheres + Ball mimics cells with a normally distributed size, and an extracellular compartment where free diffusion occurs;
- **Sph + Sph + Ball** : Sphere + Sphere + Ball models a cell as the nucleus (modelled by the first sphere) and the cytoplasm (modelled by the second sphere), and an extracellular compartment where free diffusion occurs;
- **She + Sph + Ball**: Shell + Sphere + Ball models a cell as the nucleus (modelled by a sphere) and the cytoplasm (modelled by a spherical shell sphere), and an extracellular compartment where free diffusion occurs.

Mean diffusivity from OGSE sequences Additionally to the previous models, the mean diffusivity has been computed using the oscillating gradient echoes. At a selected frequency f, the echoes from all the gradient intensities G are fitted on the three gradient directions. The diffusivity over each gradient

direction is the coefficient MD_j from the fitting of the mono-exponential model

$$S/S_0 = \exp(-b_i MD_j) \tag{5.1}$$

over the b-values b_i corresponding to each gradient G and depending on the waveform selected. Given the hypothesis of a low fractional anisotropy, the mean diffusivity is considered as

$$MD = \frac{MD_1 + MD_2 + MD_3}{3} \tag{5.2}$$

which estimates the actual apparent diffusivity in a voxel of the sample.

Non structure-related models

Mono-exponential The mono-exponential model is the classical model estimating a signal attenuation described y a single coefficient. We will refer at a mono-exponential compartment signal as S_{Ball}, as discussed in section 2.2.3. This is a pure representation of diffusion in a free condition or in a tourtuos medium.

Bi-exponential The bi-exponential model requires a second compartment described by mono-exponential decay model. The signal is represented as

$$S_{Bi-Exp} = S/S_0 = \psi S_{Ball,1} + (1-\psi) S_{Ball,2} \tag{5.3}$$

where the parameters are the volume fraction ψ and the diffusivities in the two compartments: D_1 and D_2. This signal model aims to fit the different diffusivities due to the co-existence of different populations of spins or different microstructures.

Tri-exponential The tri-exponential model requires a third compartment in addition to a *Bi-Exp*. The signal is represented as

$$S_{Tri-Exp} = S/S_0 = \psi_1 S_{Ball,1} + \psi_2 S_{Ball,2} + (1-\psi_1-\psi_2) S_{Ball,3} \tag{5.4}$$

where the parameters are the three diffusivities D_1, D_2, and D_3 while the volume fractions for the first and second compartments are ψ_1 and ψ_2.

Structure-related models

Sphere + ball The combination of a spherical restricted and a free diffusion compartment represents the description of cells and an extracellular component. The signal becomes

$$S_{Sph+Ball} = S/S_0 = \psi S_{Sph} + (1-\psi)S_{Ball} \tag{5.5}$$

where the parameters are the diffusivity in the spherical compartment D_{Sph}, the diffusivity outside D_{Ext} and size r_{Sph} and volume fraction ψ of the internal compartments. This model aims to describe the cells with the internal compartments, while the external compartment models the sum of the tortuous diffusion occurring in the connective tissue [Panagiotaki et al., 2009, Panagiotaki et al., 2012].

Distribution of sphere + ball An additional model consist in an ensemble of spherical compartments of different dimension immersed in an extracelluar mono-exponential compartment. Here the distribution of dimensions $p(a; r, \sigma)$ describes the numeric density of spheres with a specific size a. The signal becomes

$$S_{DSph+Ball} = S/S_0 = \psi S_{DSph} + (1-\psi)S_{Ball} \tag{5.6}$$

where the signal S_{dSph} averages the signal from each size of spheres at different dimensions weighted on the distribution. The actual distribution will be

$$p_V(x) = \frac{\int a^3 p(a; r, \sigma)\mathrm{d}a}{\int p(a; r, \sigma)\mathrm{d}a} \tag{5.7}$$

where the signal is effectively dependent on the number of spins in each compartment. Different distributions $p(a; r, \sigma)$ are considered. A normal distribution $p(a; r, \sigma) \sim \mathcal{N}(a; r, \sigma)$ and a log-normal distribution $p(a; r, \sigma) \sim log\mathcal{N}(a; r, \sigma)$. Here the parameters are the size of the average size r, the

spread of the distribution σ, the volume fraction of the inner compartment, ψ and the diffusivity in the spherical compartments D_{Sph} outside D_{Ext}.

Sphere + sphere + ball This model aims to describe the effect of nuclei and cellular membranes when the nuclei occupy a reduced portion of the cell. The signal is described as

$$S_{Sph+Sph+Ball} = S/S_0 = \psi(\psi_r S_{Sph,r} + \psi_R S_{Sph,R}) + (1-\psi)S_{Ball} \tag{5.8}$$

where the volume fractions ψ_r and ψ_R are related by the size of the spherical compartments as

$$\psi_r = \frac{r^3}{R^3} \qquad \psi_R = \frac{R^3 - r^3}{R^3}, \tag{5.9}$$

and the volume fraction, ψ, indicates the total volume occupied by the intracellular compartment. The parameters to be estimated are the inner radius, r, the outer radius, R, the diffusivities in the three compartments D_{nuc}, D_{cyt}, and D_{ext}, and the volume fraction ψ.

Shell + sphere + ball This model is composed of an internal spherical compartment representing the cell nucleus, an external spherical shell representing the cytoplasm, and the extracellular compartment. The signal is described as

$$S_{She+Sph+Ball} = S/S_0 = \psi(\psi_r S_{She,r} + \psi_R S_{Sph,R}) + (1-\psi)S_{Ball} \tag{5.10}$$

where the parameters are the size of the nuclei, r, the size of cells, R, the diffusivities in the nuclei, in the cytoplasm and outside, D_{nuc}, D_{cyt}, and D_{ext}, and the volume fraction of cells, ψ. The volume fractions of nuclei and cytoplasm are defined in equation 5.9. This model is the full representation of MR signal geometrically related to the cytoarchitecture.

5.2.4 Parameter estimation

This work discusses the ability of the models presented to fit oscillating gradient diffusion MRI signals, and to estimate microstructural features. The

ranking of models were conducted on the signal averaged on all the voxels in the samples. Alternatively, the studies on the estimation of microstructural parameters were performed voxel by voxel.

Samples from the two cell lines were also acquired with a DTI protocol. Estimation of mean diffusivity and fractional anisotropy over these data were performed with the Camino Toolkit [Cook et al., 2006]. Additional MD masks were generated from the DTI data to isolate the ROI. Two MD masks were considered, a high pass mask eliminating extremely low diffusivity regions probably related to bad fixation, and a low pass mask eliminating voxels above free water diffusivity value.

Models fitting the CW-OGSE signals were implemented in `Matlab` based on the work from [Xu et al., 2009a], while SW-OGSE derive from [Ianuş et al., 2013]. The SW-OGSE models consider an effective trapezoid waveform only for modelling the mean diffusivity. All other SW-OGSE related models are implemented using a square waveform. Parameter estimation was performed with a Levenberg-Marquardt (L-M) algorithm minimising the difference between experimental signal and synthetic signal generated by the model.

5.3 Results

5.3.1 Description of the samples

In xenograft tumours, a degree of inhomogeneity in the microstructure should be expected. The samples were fixated, preserved, and rehydrated before the experiments. Fixation and rehydration could introduce deterioration of the microstructure on the edges of the sample or in accessible inner regions. All these possible artifacts could be observed on a diffusivity map, but it could be difficult to distinguish them from natural microstructural variability.

Figure 5.7 shows the mean diffusivity computed as described in section 5.2.3 over the Square Wave OGSE data. The protocol includes only three gradient directions; consequently, the mean diffusivity is an average over the apparent diffusion coefficients over the three directions. In both the cell lines, areas of low diffusivity can be observed on the edges (see samples *LS1*, *SW2*, and

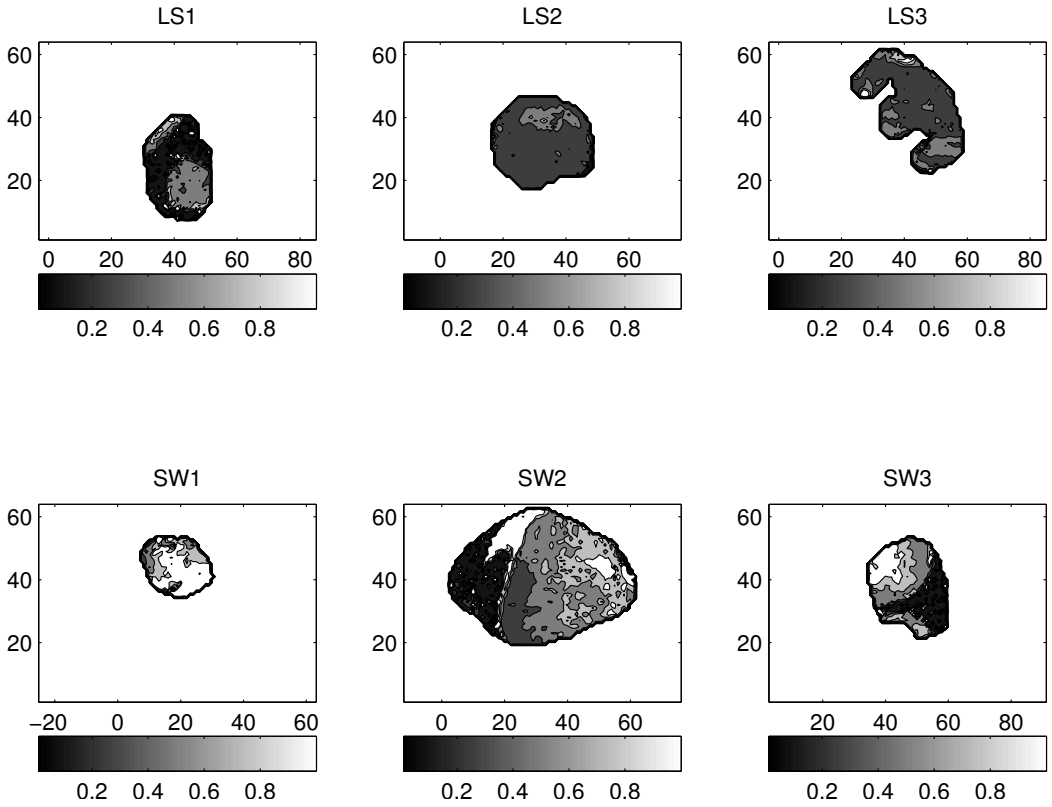

Figure 5.7: Mean diffusivity (MD) obtained with a SW-OGSE at 50 Hz. The most representative slide is selected for each sample to show the pattern of MD expressed in $\mu m^2/s$.

SW3). A more regular MD pattern can be observed on LS samples, mainly in *LS2*, and *LS3*. Figure 5.8 shows the identical information on Cosine Wave OGSE data. The mean diffusivity is higher than in the SW-OGSE. Similar patterns can be recognised on the maps obtained from the two sequences, and low diffusivity areas persist in position. The increase in the estimated MD values from the CW-OGSE data arises from the higher b-values obtainable from the SW-OGSE acquisitions at 50 Hz. The diffusion propagator is not perfectly Gaussian so the signal is not mono-exponential, which causes lower apparent diffusivity at higher b-values.

The MD maps show the presence of different regions in the sample. The regions show a continuity across the slides (data not shown) and present a degree of change not directly associable with susceptibility effects. The mi-

crostructure of a xenograft tumour is expected to be homogeneous despite a vascular tissue is developed. The evolution of the tumour might create regions of hypoxia, where the microstructure might degrade creating variations in the confinement. Additionally, fixation might not have penetrated through the whole sample, creating regions where the sample degraded with time. Finally, the xenograft tumours were grown subcutaneously in this experiment, and connective tissue might be present. The presence of regions with low MD in this case is likely to be related to poor fixation.

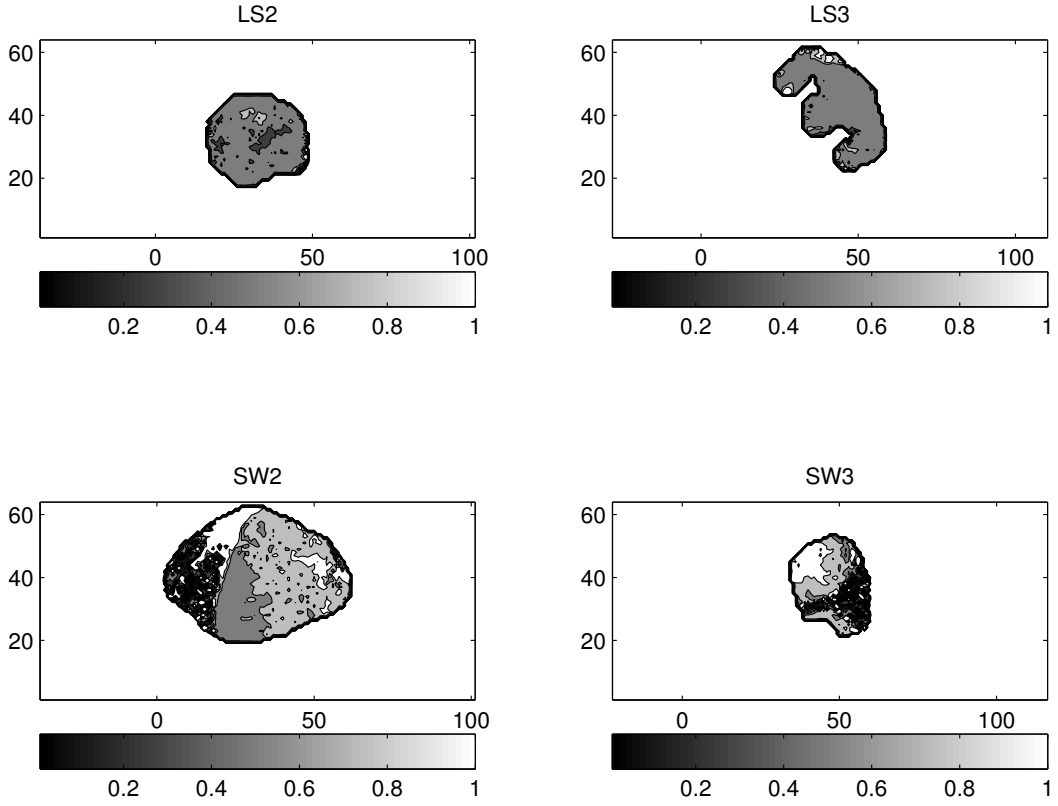

Figure 5.8: Mean diffusivity (MD) obtained with a CW-OGSE at 50 Hz. The most representative slide is selected for each sample to show the pattern of MD expressed in $\mu m^2/s$.

Figure 5.9 shows the fractional anisotropy estimated from the DTI protocol. The protocol includes 42 directions, and data were processed with *Camino Toolkit*. The FA is above 0.2 in 22% of the pixels in the worst case sample (*SW2*) where only 6% of the pixels are above 0.25. The other samples show

an average FA of 0.104 and a standard deviation of 0.044. The low mean diffusivity regions of figure 5.7 are no longer observed in the pattern of FA, but the highest FA values are located in such regions. No substantial difference is observed between the two cell lines.

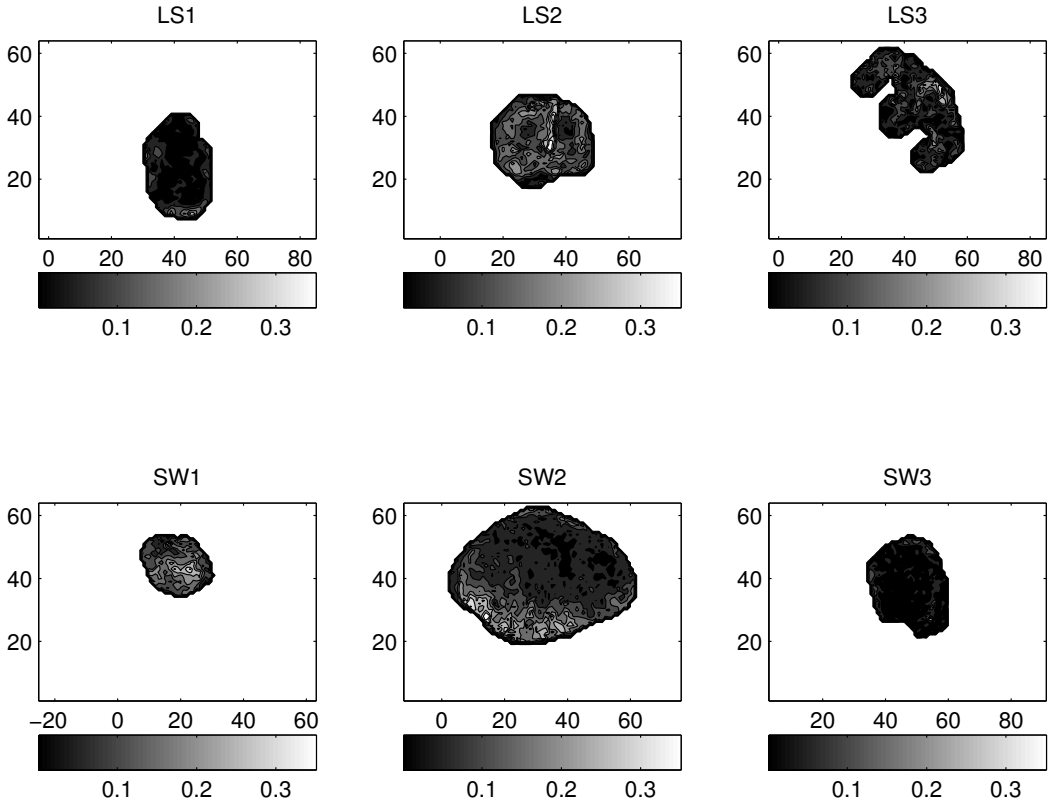

Figure 5.9: Fractional anisotropy (FA) in a FOV of a DTI acquisition. The map is generated with *Camino Toolkit* over a single slices of LS and SW samples.

5.3.2 Diffusivity with frequency

Figure 5.10 shows the increase of mean diffusivity with the frequency from SW-OGSE data. The plot presents the average of mean diffusivities from the samples of each cell line, and their standard deviation. Mean diffusivity increases with the frequency, despite a larger ratio is observed at lower frequencies. The two cell line cannot be distinguished using the MD only, but

LS cell line has a lower mean value on all the frequencies. All the MD values are below the diffusivity in-vivo, always below 1.1 μm^2/s. Frequencies of 25 and 500 Hz were excluded from the plot. The waveform at 25 Hz is a PGSE with clinically unfeasible b-value (see table 5.1) while the waveform at 500 Hz shows preponderant waveform implementation imperfections.

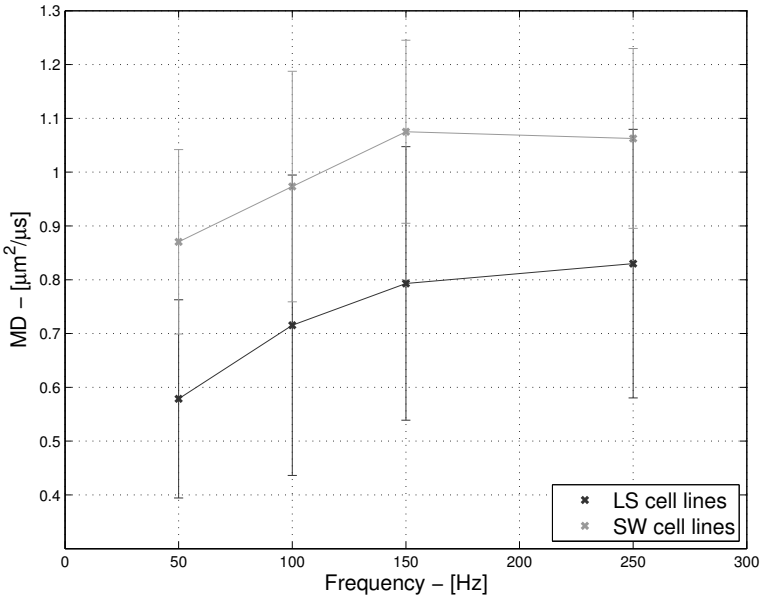

Figure 5.10: Mean diffusivity estimate at different frequencies. The estimate was generated from the signal from all the voxels of every sample, and the mean diffusivity from the samples of each cell line were used to compute the mean value and the standard deviation.

Figure 5.11 shows the map of MD over the different frequencies on sample *SW1*. The values of MD shows a slight decrease from 25 to 50 Hz, and a constant increase over the other frequencies. The map at 500 Hz provides unrealistically high values of diffusivity over the entire sample, and the high homogeneity suggests an inappropriate fitting. Along that, areas at very low diffusivity (MD<0.1 μm^2/s) persist for all the frequencies, suggesting presence of corrupted microstructure. Over the frequencies from 50 to 250 Hz, an increase of mean diffusivity can be observed despite a significant component of noise appears.

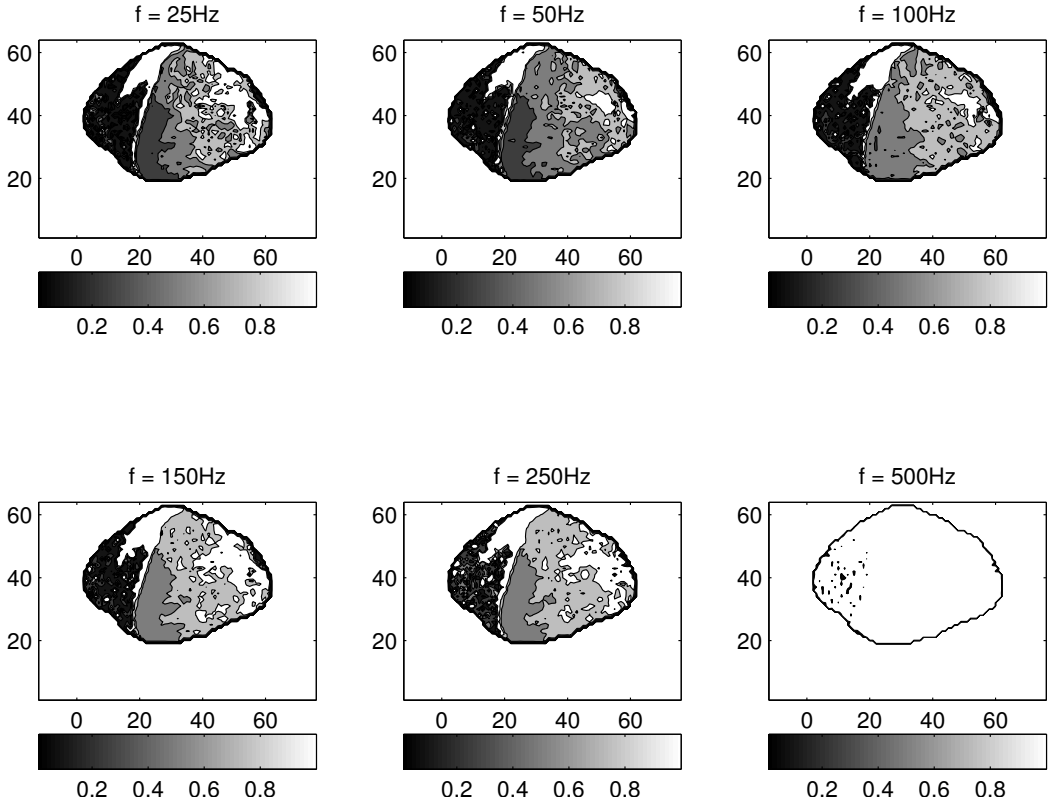

Figure 5.11: Mean diffusivity maps different frequencies for sample SW1.

5.3.3 Models ranking

The models of signal were fitted on the signals from all the sample slices for each cell line. The signal from each sequence parameter pair (f,G) on each voxel was added to generate a single echo decay profile. Bayesian information criterion (BIC) offers an indication of the ability of the model to fit the signal as discussed in appendix A.2.2. Fitting was performed excluding data acquired with 25 Hz and 500 Hz.

Table 5.4 presents the BIC for all the models applied to each cell line. The three models not related to the microstructure (*Mono-*,*Bi-*, and *Tri-exponential*) perform worse in the ranking. Models with a single sphere follows in the ranking, and finally the distribution of spheres and the cells model. The values of BIC are always negative, indicating a good fitting of the echoes for all the models. The models perform very similarly on both the cell lines, de-

Rank	BIC	LS	# par	BIC	SW	# par
1	-160.2	She+Sph+Ball	6	-162.0	She+Sph+Ball	6
2	-158.8	Sph+Sph+Ball	6	-161.5	Sph+Sph+Ball	6
3	-158.2	normDSph+Ball	5	-159.1	lognDSph+Ball	5
4	-156.8	lognDSph+Ball	5	-155.4	normDSph+Ball	5
5	-151.3	Ball+Sph	4	-146.0	Ball+Sph	4
6	-133.6	BiExp	3	-132.1	BiExp	3
7	-130.2	TriExp	5	-127.0	TriExp	5
8	-97.2	MonoExp	1	-101.8	MonoExp	1

Table 5.4: Rank of fitting performances of the models over the two cell lines.

spite the SW introduces a larger separation between the best ranked model and the ones modelling distribution of spheres. On both the cell lines, the use of a single restricted compartment is not sufficient to offer a good fitting. The BICs calculated for the models using restricted compartments are very similar to each other. The signal has a very high SNR leading to larger variations of the criterion as a consequence of small reductions in the error, which can dominate the penalisation for the introduction of extra-parameters might be compensated. Such small variations would probably not be observable on a signal with an SNR compatible to clinical practice.

Figure 5.12 presents the fitting of the model to the measured data for the samples *LS1* and *SW1*. Both the datasets the sequences acquired at 50 Hz and 250 Hz are fitted more accurately by non-exponential models. Additionally, a better fitting of the *She + Sph + Ball* model can be observed compared to the *lognDSph + Ball* model only in the lower frequencies in the fitting of *SW1*. Additional models were not reported due to the similarity of their fitting to the shown models. It must be recognised that the ideal condition (very high SNR) might not be expected during in-vivo acquisitions. Generally, a better fitting is observed on the dataset *SW1* mainly in relation to the ability of the model to fit the data acquired with a sequence with a frequency of 150 Hz.

5.3.4 Parameter fitting

The best ranked models fit the signal by representing different microstructural features of a biological tissue explicitly. Here, we show estimates obtained voxel

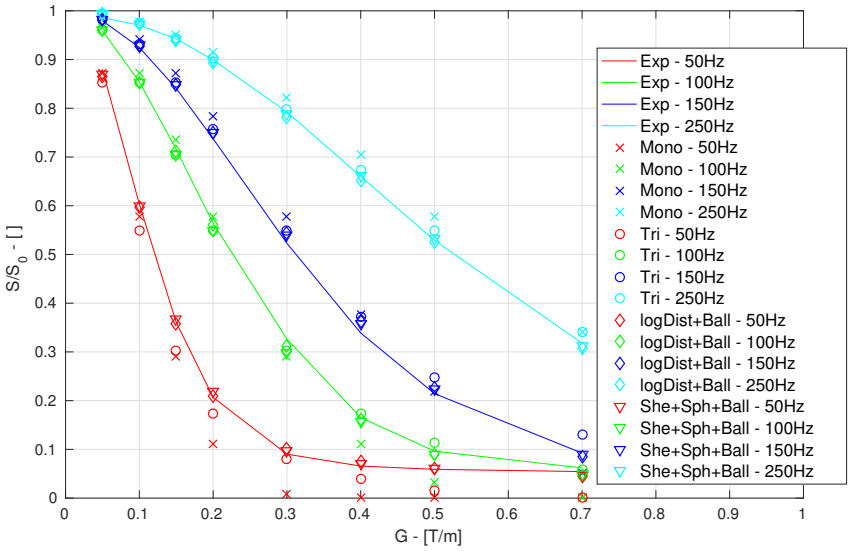

(a) LS1

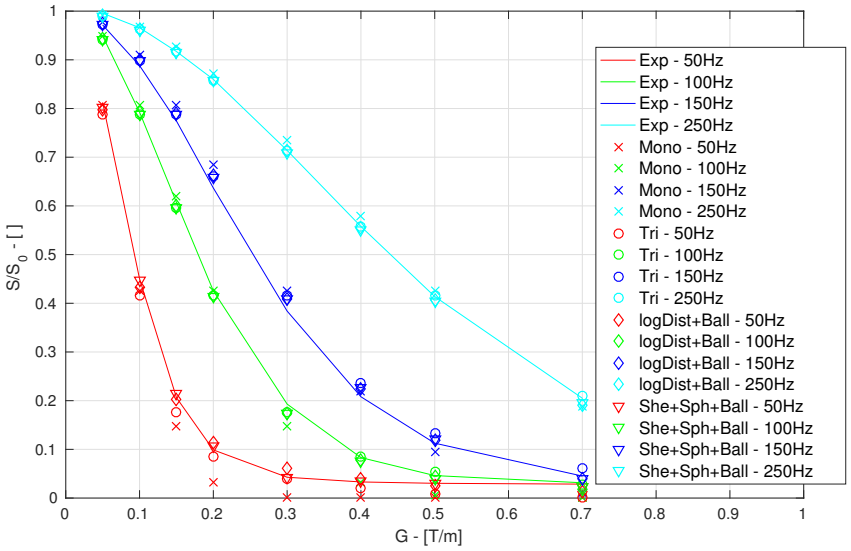

(b) SW1

Figure 5.12: Fitting of *MonoExp*, *TriExp*, *lognDSph + Ball* and *She + Sph + Ball* models on the data. The fittings to the signal obtained from sample *LS1* in (a) and *SW1* in (b) are presented.

by voxel, and we describe the variability of the estimates across the different samples. Because of its generality, the first indicator of the microstructure is the mean diffusivity then we move to structure-related models. Each voxel in each slice is considered, but two mean diffusivity masks were applied to eliminate voxels with a MD less than 0.1 $\mu m^2/\mu s$, and with a MD larger than 2 $\mu m^2/\mu s$. The MD masks are necessary to isolate the artifacts related to the fixation process.

Figure 5.13 presents the distribution of mean diffusivity over the voxels of each sample. The plots were obtained with the application of the MD masks over data acquired with SW-OGSE at $f = 150$ Hz. The two cell lines maintain a difference in MD, and SW voxels tend to present higher values. Half of *SW1* sample voxels are above 1.2 $\mu m^2/\mu s$, suggesting the presence of possible artifacts as well as large internal pools. Samples *LS2* and *LS3* present a limited variability confirming the visually observed absence of artifacts in the slices. Samples *LS1* and *SW1* were acquired together, and both present higher value and larger spread of the distribution of MD compared to the others. Finally, table 5.5 presents the average and the standard deviation of MD estimates for each sample. Similar considerations as discussed could be applied.

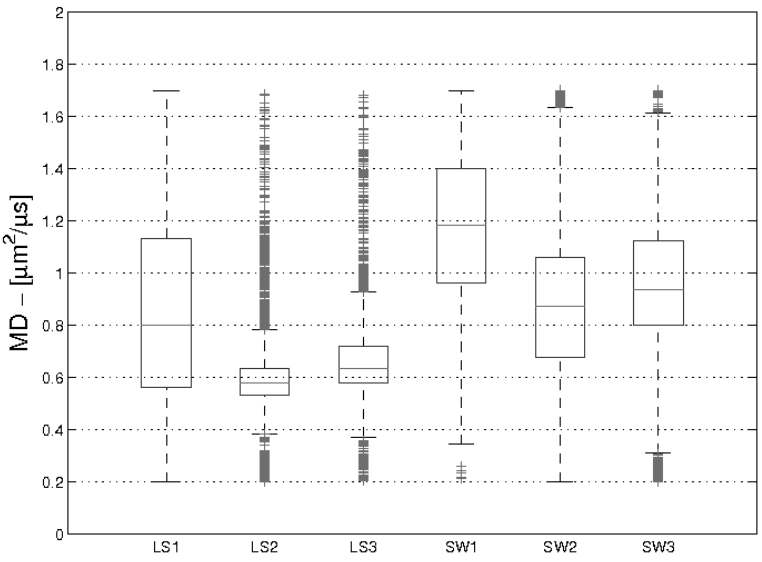

Figure 5.13: Mean diffusivity boxplots for the different samples. Distributions were obtained after MD masking with a waveform frequency of 150 Hz.

	LS1	LS2	LS3	SW1	SW2	SW3
mean MD - [$\mu m^2/\mu s$]	0.603	0.522	0.557	1.180	0.868	0.828
std. MD - [$\mu m^2/\mu s$]	0.509	0.250	0.418	0.407	0.429	0.504

Table 5.5: Mean diffusivity statistics over each sample. Average value and standard deviation of mean diffusivity across the voxels on each sample is obtained by fitting the SW-OGSE data with a frequency of 150 Hz.

Figure 5.14 presents the estimates obtained from the model *DSph + Ball* with a normal distribution of radii. The average radius r, varies between the samples, but remains below 1.2 μm. The standard deviation of the distribution σ allows to discriminate between the two cell lines as it has larger values in SW samples. The combination of a low value of r and a large variance implicates that the negative tail of the normal distribution is not negligible. As a consequence, the distribution fitting the data cannot be considered Gaussian anymore. As a second consequence, the actual average size value will be larger than the parameter r and directly related to the value of σ. Finally, the volume fraction occupied by the intracellular compartment is compatible with histology only in sample *LS2* (histology: SW = 0.80 $\pm$ 0.02; LS =0.79 $\pm$ 0.01 [Panagiotaki et al., 2014]), but the model underestimates ψ in the other cases .

Figure 5.15 presents the estimates of microstructural features obtained with the best ranked model *She+Sph+Ball*. The estimates of the radius of the inner spherical compartment r remain between 1.65-2.44 μm for all the samples, and no discrimination between the cell lines exists. Conversely, the estimates of the cell size R show larger differences between LS and SW samples. SW samples present average values of R between 4.57-5.00 μm, while LS samples between 2.86-4.11 μm (histology: SW = 8.0$\pm$0.4 μm; LS = 11.2$\pm$2 μm). The estimates of volume fraction ψ, are compatible with histology for all the samples except *LS2*, which estimates an unrealistic value of ψ.

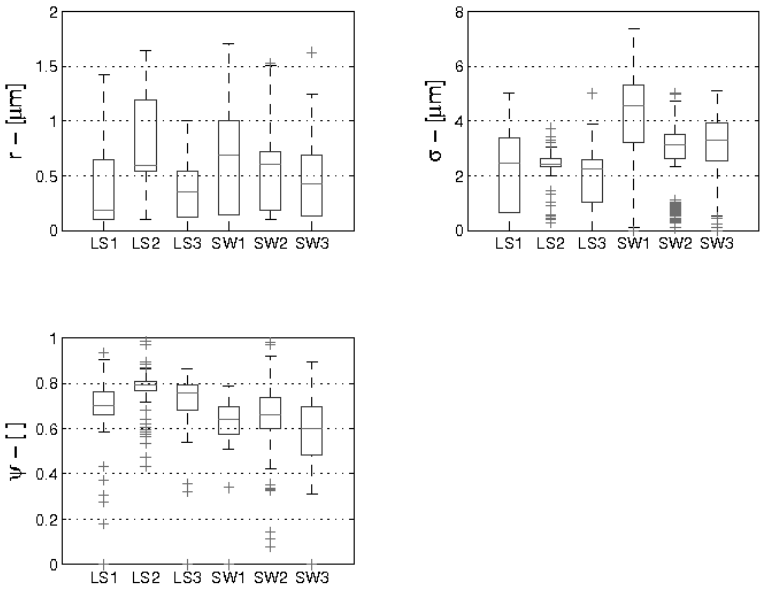

Figure 5.14: Microstructural estimates from a normal distribution of radii model. Boxplot representing the estimated average radius r, the spread of radii distribution σ, and the volume fraction ψ.

5.4 Discussion

The samples acquired during the experiments are characterised by a strong inhomogeneity of the microstructure. The coexistence of physiologically different areas in tumours and of the fixation process makes difficult to separate artifacts from the natural microstructural variability. Low diffusivity (diffusivity below 0.1 $\mu m^2/\mu s$) areas localised on the edges, or in sharply-delimited portions of the sample (i.e. in samples *LS2* and *SW2*), suggests the presence of a deterioration of the microstructure due to fixation or rehydration. Molecules of PFA bind with collagen to stop deterioration which reduces diffusivity, but also preserves the architecture of the microstructure within a limited shrinkage (less than 10%) [Skaer and Whytock, 1976,Augusteyn et al., 2008]. Conversely, improper fixation could lead to strong alterations of microstructure and protein texture which might enable a further reduction of apparent diffusivity. A second artifact can be related to a not appropriate preparation of samples when blood residuals can cause susceptibility artifacts at high gradients.

The mean diffusivity is the first parameter considered in this study. The

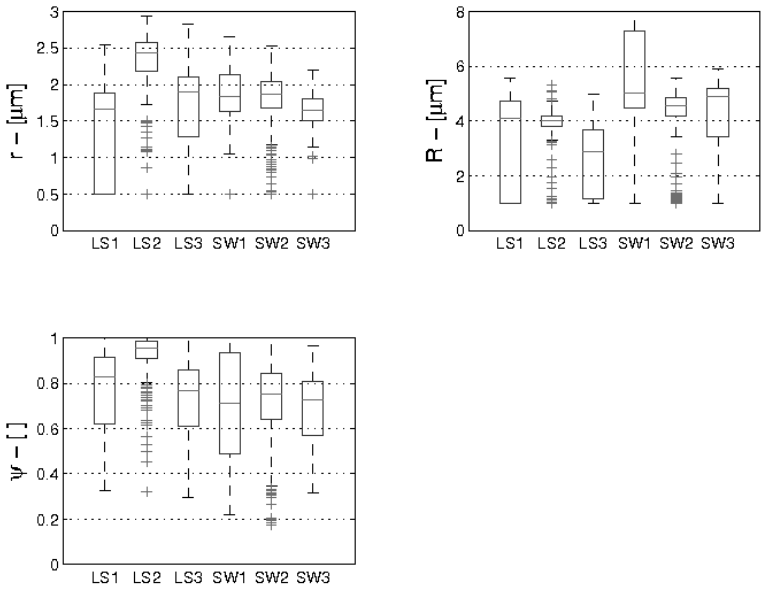

Figure 5.15: Estimates of microstructural parameters from the model *Shell + Sphere + Ball*. Only the geometrical estimates of the microstructure are shown in this plot, since the variability of the diffusivity does not provide additional discrimination criterion.

first analysis was performed on all the pixels of each sample, while too high and too low diffusivity pixels were excluded in the second analysis. The attempt to exclude artifacts using MD masks offers a partial solution, but failed to perform well when higher order models were fitted. When all the pixels were considered, the presence of a large number of upper outliers suggests the presence of fitting errors due to susceptibility artifacts. The diffusivity of water molecules in-vivo is generally below $1.2\,\mu\text{m}^2/\mu\text{s}$, but the fixation process with PFA introduces a reduction of diffusivity as the MD distributions remain consistently below except for the sample *SW1*. Sample *SW1* should be considered an outlier as the estimated MD values are not expected in dense microstructure such as a xenograft tumour.

The values of the fractional anisotropy indicate the presence of an anisotropic microstructure for all the samples. DTI data offer a description of the sample based on 42 gradient directions, and FA maps show a FA mean value of less than 0.1 for all the samples. The low FA enables to dismiss any anisotropic

model such as Cylinders or Zeppelin. Despite results (not shown) indicate a random orientation of fibers in the largest part of samples, small regions have a coherent orientation of anisotropy. These regions can be observed on the edges of the sample (epithelial tissue) or on internal separations of tumour regions where large blood vessels can be found.

The models ranked in this work can be separated between generic and structure related. The models not related to the microstructure perform worst as they are not able to fit the signals at different frequencies. This limitation is observed for the mono-, bi- and tri-exponential decay models, and it suggests that additional not restricted signal components would not be able to overcome the bad fitting. Conversely, the use of restricted compartments improves the fitting of signal as they explicitly model the effect of confinement due to barriers in the microstructure. This element becomes essential when very different frequencies are considered at the same time. The BIC values show a large improvement when restricted compartments are introduces, and the presence of at least two parameters describing the dimensions of the restriction provides an additional benefit. The study of model performances was conducted on signals with a SNR above 65 for both the cell lines. A good signal is reasonably fitted by models with a large number of degrees of freedom, but for in-vivo applications we should expect to see a different model ranking due to the lower SNR.

The best performing model is *Sph + She + Ball*. The compartments included in the representation correspond to the biological components of the cytoarchitecture, but no structure-specific extracellular compartment is considered. The second best model is *Sph + Sph + Ball*, and it performs very similarly to the first when nuclei have a much smaller dimension than the cell membrane. The *Distribution of Sphere + Ball* models are a continuous representation of different scales of confinement, and they score a slightly larger BIC value (2-3 points). A retrospective interpretation could suggest that these models represent a continuous distribution of sizes of nuclei and cell membranes. In conclusion, all the most performing models are able to consider at least two confinement length scales.

The ultimate target of this work is to discuss the ability of the models to

estimate microstructural features from the signal. The model *Sph + She + Ball* estimates larger values of cell radii R, in the SW cell line while histology recorded that the average radius in LS cells is 2 μm larger than SW's. This discrepancy, along with the underestimation of the cell size for both the cell lines suggests that additional constraints should be posed to the model. The model appears to underestimate R by increasing the extracellular and the cytoplasm diffusivity; consequently, an a-priori knowledge of cytoplasm diffusion coefficient could improve the accuracy of the estimates. At the same time, histology has been performed by colleagues on freshly excised tumours, and the shrinkage due to fixation could have reduced the cellular dimension before the present MR acquisitions. Finally, the manual redefinition of the ROI over parts of sample not deteriorated would help to explain outliers such as the volume fraction estimates of sample *LS2*.

The inversion in the trend between the estimates of the cell size in the two cell lines against the histological data ought to be discussed further. In a first instance, it must be observed that a variability across the samples can be observed also within the same cell line, showing a possible histological variability which is not considered in this model. The extracellular microstructure might also play a role, showing a confinement in the SW cell lines which might be masked in the LS signal. This second consideration might suggest that the glandular extracellular component in the SW samples is playing a role in the determination of the signal, offering a significant confinement at larger scales of the nuclear membrane, which is not observed in the poorly differentiated microstructure in the LS cell lines. Finally, a possible different effect due to spin-spin exchange might have caused an artifact in the signal.

The model *Sph + She + Ball* is a simplified representation of the microstructure. The microstructure in a xenograft tumour can introduce additional elements such as cells with multiple nuclei, showing a diffusion confined in small regions but occupying a larger volume. Additionally, in-vivo extracellular component should account for vascularity, necrotic regions, and variations in the cell packing.

5.5 Conclusions

This work discussed an ex-vivo study aiming to describe the performances of high order microstructural models for oscillating gradient spin echo protocols. The selection of different frequencies of gradient waveform shows that the estimates of mean diffusivity are related to the frequency itself; consequently, the frequency of the waveform is able to selectively probe a microstructural scale. Finally, the ranking of the models based on BIC suggests an explicit correspondence between the cytoarchitecture and the compartments in the MR signal model.

The present work is limited by the samples available. As a matter of fact, it is not able to offer a generic indication on the ability of the high order models to estimate microstructural features as the artifacts might alter the results. A manual selection of the ROI, based on cross-information between OGSE and DTI data, is required as well as an additional histological validation performed over fixated samples.

The use of oscillating gradients can offer a non-invasive insight of the microstructure of a biological tissue. The work presented in this chapter finds its evolution in the combination with an optical technique able to probe nuclei dimension and numerical density. Their combination is a work in preparation, and a deeper description of the approach is provided in section 8.1.

Chapter 6

Multimodality investigation of microstructure in colorectal cancer cell lines

6.1 Introduction

The investigation of the human body using non-invasive diagnostic techniques is a research area with extensive clinical applications. This field has been of great interest in the last decades, and it was pushed by the attempt to obtain information about the microstructure of the samples. This might enable localised pathologies to be characterised or to offer useful information in other disciplines (i.e. colloids and food science, material engineering). The focus on obtaining enhanced understanding of the microstructure using separate techniques, offered the ground for a combination of two or more different contrast mechanisms from separate techniques.

One additional technique adopted for the diagnosis of pathological conditions on skin and epithelial tissues is the optical spectroscopy applied in the visible and NIR range [Yodh and Chance, 1995, Kurhanewicz et al., 2002, Schuele et al., 2005, Itzkan et al., 2007]. An introduction to these techniques was provided in section 4.1 where medical and industrial applications were discussed. Furthermore, the study of polarisation properties of the light may provide

additional information on the microstructure [Baba et al., 2002, Lie et al., 2008,Schmitt et al., 1992,Gurjar et al., 2001,Feng et al., 2013]. Polarised light has been extensively adopted in industrial applications and quality assurance to determine the dimension of the microstructural elements in industrial products. In industrial applications, the microstructure tends to be composed of well determined components with optical properties significantly different from the background, contrary to biological media where such differences are not equally marked [Diko et al., 1995, Mali et al., 2002].

The application of polarised light for biological tissues began less than two decades ago. Pathologies affecting epithelial cells such as different forms of cancer are connected to significant changes in the histology of the tissue [Jass et al., 1986]. A large-scale early detection of skin or epithelial lesions requires a practical and possibly inexpensive technique able to isolate the signal from superficial layers where the pathology is initially located [Arifler et al., 2003]. The presence of several components in the microstructure presenting different optical properties could be responsible for the alterations in the polarisation of light emerging from the tissue [Sokolov et al., 1999]. In the case of densely packed cells, the polarisation of a light beam can be changed by the interaction with a few centimetres of material, and become randomly polarised after a few scattering events [Schmitt et al., 1992]. The use of different states can be used to select different a depth of investigation in the sample, and it can isolate the properties from scattering events on the surface [Feng et al., 2013].

The characterisation of the microstructure of a tissue based on scattering properties generally assumes that the microstructure is composed by a set of separated scatterers. The scatterers are determined by the difference in refractive indexes that the biological tissues tend to show between cytoplasm and nuclear material [Mourant et al., 1998,Beuthan et al., 1996,Pu et al., 2012, Xu et al., 2006]. Variations in the refractive index can be exploited under the assumption that extracellular material and cytoplasm have different properties compared to nuclei and organelles such that the latter could be identified as the scatterers [Mourant et al., 2000]. The contribution to the scattering signal of the cellular membranes is generally negligible, and the reduced difference in refractive index between cytoplasm and extracellular component leaves the

dimension of nuclei the most important and easiest parameter to estimate given the high refractive index of the chromosomes [Maier et al., 1994, Brunsting and Mullaney, 1974]. The design of a model able to predict the optical signal often requires a prior knowledge of the microstructure [Whateley et al., 1984, van Staveren et al., 1991].

The visible and NIR light backscattered from the interesting layer of the sample could only be isolated and studied to extract information on the microstructure [Flock et al., 1992, Nachabé et al., 2010, Sankaran et al., 1999, Xu et al., 2009a, Feng et al., 2013]. *Gurjar et al.* presented an approach to determine the dimension of nuclei and organelles in cells from epithelial tissues by subtracting the signals obtained from two channels detecting orthogonal linear polarisation states [Gurjar et al., 2001]. The difference between the two spectra isolates the contribution from ballistic photons while the remaining part of light represents the contribution from the scattering in deeper layers [Sokolov et al., 1999, Backman et al., 1999, Perelman et al., 1998, Gurjar et al., 2001, Schuele et al., 2005].

The combination of different techniques is a step forward in developing a non-invasive diagnosis approach. The contrast mechanisms from two techniques can be exploited to obtain a set of information which cannot be obtained separately. The work in chapter 5 discussed the investigation of the microstructure of a sample with diffusion MRI adopting an Oscillating Gradient Spin Echo. In this chapter, a work is presented to determine the feasibility of the combination of Laser Scattering Spectroscopy (LSS) and MR techniques to characterise the microstructure of a tumour cell line.

6.2 Methods

6.2.1 The design of the experiment

The objective of this work is to develop a model informed with data obtained from Laser Scanning Spectroscopy (LSS) and diffusion MR signals. The experimental work was separated in two stages, one for each technique. In a first stage, the experimental procedure described in section 5.2 was performed. In

a second stage, a set of optical measurements was taken on the same samples acquiring a spectroscopic signal in the vis-NIR range.

The samples

This second stage of the experimental work was separated into a preliminary phase where the emulsion already described in section 3.2.1 was adopted, and in the actual experiment performed on a set of six xenograft tumours, three grown from LS174T and three from SW1222 cell lines. A detailed presentation of the tumour samples can be found in section 5.2.1.

The optical measurements were performed in a period of time between a few days and two months after the MR experiments. Immediately after the MR experiments, the tumour samples were unwrapped from the gauze in which they were contained and washed with PBS (Phosphate Buffet Solution) to remove traces of Formblyn ^{TM}, in which the samples had previously been submerged during the MR scans. The Paraformaldehyde (PFA) solution in which the samples had been preserved was mechanically filtered and the tumours were re-submerged into it and preserved in smaller containers.

LSS experimental setup

The objective of the optical experiments is to use polarised light to isolate the component of the signal related to the scattering from superficial layers. An optical system was assembled to be able to illuminate the sample with linear polarised light and to detect the backscattered light either with a polarisation parallel or orthogonal to the incident beam. The selection of the first (parallel) or the second (orthogonal) channel was performed by rotating a polarising filter placed in front of the detector. The subtraction between the two channels isolates the linearly polarised component of backscattered light generated by the superficial layers only [Gurjar et al., 2001]. Figure 6.1 provides a scheme of the experimental setup which is also partially captured in figures 6.2 and 6.3. The light generated by a lamp was collimated, linearly polarised and deflected towards the sample by a beamsplitter. The backscattered light was then transmitted through the beamsplitter, filtered with a second polarising filter and

detected by a spectrometer. The optical system was prepared on an optical bench and left assembled for the duration of the experimental campaign. The experimental setup was designed to enable ready interchange of the detection system, between the spectrometer that has been adopted and an eventual camera. The measurements conducted with the camera were incomplete and will not be discussed in this work but were used to investigate possible sources of experimental error.

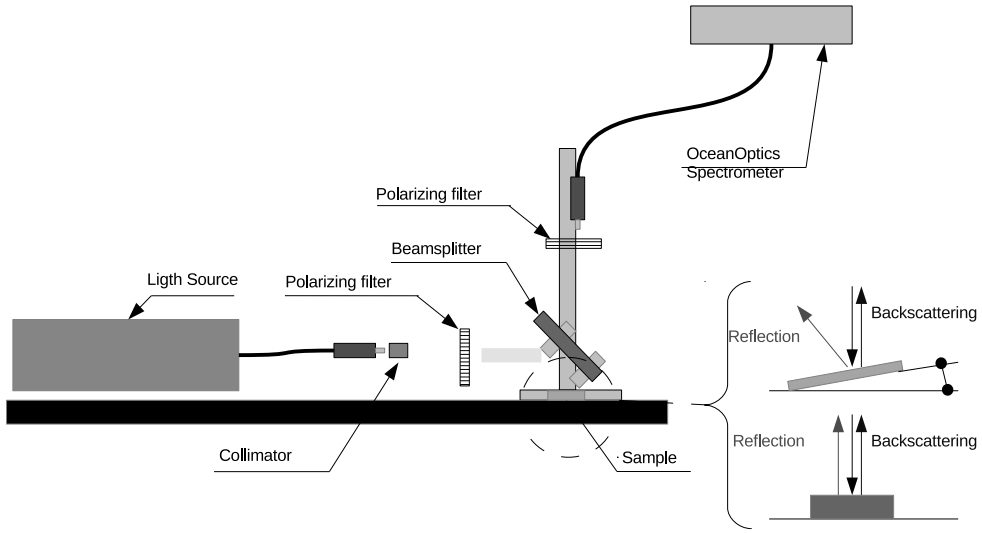

Figure 6.1: Scheme of the experimental setup adopted during the polarimetric measurements.

An *Ocean Optics* HL-2000 broadband lamp was adopted as the light source. The device consisted of a Tungsten Halogen bulb with 5 W of nominal power, offering a stable illumination in the range 360–2400 nm, and providing 6.8 mW of output power through the optical fibre. The light was transmitted with an optical fiber integrated in the lamp, and subsequently passed through a collimator. The collimator was produced by *Thorlab Inc*, designed with a fixed focus aligned at 633 nm, and with an anti-reflex coating optimised

between 650–1050 nm.

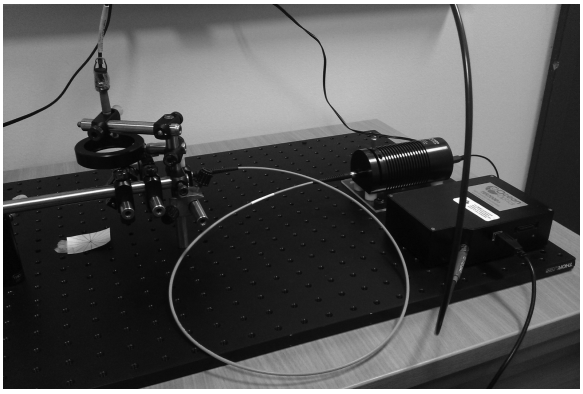

Figure 6.2: Photography of the optical bench prepared for the experimental work.

A plate beamsplitter (12.5 x 17.5 mm) offered a 50:50 split with an optimal application range between 500–700 nm. It was used to deflect light from the source towards the sample and to transmit the light emerging from the sample. Figure 6.3 shows the setup of the beamsplitter in the current experimental work. The specific design of the experiment did not require highly performing beamsplitters given that the discrepancy of transmissivity and reflectivity from the nominal rating at the different wavelengths was corrected through signal calibration. Two polarising filters were also adopted. They were designed to be mounted on a 22.5 mm gear to be promptly installed on a camera lenses and optimised for applications between 400–800 nm with an efficiency profile decaying immediately after 800 nm. The beamsplitter and the polarising filters were produced by *Edmund Optics Ltd.*

The detection was performed with an *Ocean Optics* HR+C1689 spectrometer, detecting light spanning between 188–1109 nm and producing a spectrum subdivided in 2048 channels. The spectrometer has an embedded optical fibre with a NA = 0.14.

The experimental equipment was set up as described in figure 6.1. The elements were aligned to avoid direct reflection by introducing an angle slightly above 45 degrees between the source beam and the beamsplitter. Subsequently, the detector optical fibre was aligned to enable a reading from that direction

only. The other possible sources of light were shielded to avoid noise or bias in the signal, and the bench was covered with a cloth of dark fabric to exclude room light.

LSS experimental procedure and signal post-processing

The experiments were composed of two phases. The first phase consisted of the study of the emulsion described in section 3.2.1. The emulsion was placed in a glass container of approximately 80 mm of diameter and 40 mm of depth, and the surface of the emulsion was smoothed to avoid localised direct reflection caused by heterogeneity. The second phase required the study of tumour samples. The tumours were extracted from the containers where preserved and then washed with saline solution to eliminate films of fixative on the surface. The samples were subsequently placed on a glass slide, and the slide was held around 30 mm from the base of the optical bench to avoid reflection from the surface of the optical bench. Signals from the tumour samples were acquired from each of them.

In each of the two phases, the samples were placed as discussed, and the

Figure 6.3: Photography of the experimental setup utilised for the measurements with polarised light.

light source was warmed up for around ten minutes before starting measurements. A first set of calibration measurements was performed to acquire reference signals by orienting the polarisation filter in front of the detector in 18 directions to map the profile against a polarisation preserving mirror oriented to offer direct reflection. Previous measurements on the broadband dielectric mirror suggested that a constant reflection was expected between 400–800 nm. Subsequently, two calibration spectra were recorded from a white diffusive surface. Signals which originated from the samples were then investigated.

The system contained a significant degree of complexity determined by the presence of multiple optical components utilised in sequence. Each component has been designed to work in a range of wavelengths discussed in section 6.2.1. A possible approach would be to characterise the system utilising the manufacturer calibration curves to obtain the cumulative fingerprint, but the large number of components and the uncertainty on data should discourage such an approach. In this work, calibration measurements were used instead.

The signals obtained from the parallel and orthogonal channels were calibrated during the post-processing. The two calibration measurements previously taken were subtracted from the signals obtained from respective channels independently. The necessity to eliminate the spectral signature of the system from the spectrum and the complexity of the system which presents different properties in the two different channels required a disjointed approach in each channel.

Diffusion MRI experiments and post-processing

The experimental results presented in chapter 5 were adopted in the present work. Only the echoes obtained with a Square Wave OGSE waveform were included in this study. The frequencies of 50, 100, 150 and 250 Hz and the gradient intensities of 0.05, 0.10, 0.15, 0.20, 0.25, 0.30, 0.40, 0.50, 0.70 T/m were paired to generate 36 datapoints. A more detailed description of the imaging protocol has been presented in section 5.2.2.

The data obtained from the different slices of each sample were filtered with a Mean Diffusivity mask to exclude voxels of corrupted signal. The signal from

all the voxels was cumulated to represent the entire sample and the obtained spectra were used in this work.

6.2.2 The microstructural model

Mathematical models can be designed to link the microstructure of the sample to the signals observed in both the modalities. Here, we define *microstructural model* as the set of assumptions on the geometry of the microstructure which the signal models rely on. Several microstructural models were considered in the previous chapters (see sections 4.2.2 and 5.2.3) and each of them tried to capture different aspects of the mictrostructure (i.e. distribution of droplets size, presence of nuclei in cells).

In this final part of the work, the geometry represented by the microstructural model is illustrated in figure 6.4. The model represents the tissue as a collection of spherical cells. The cell nucleus is a spherical compartment, the cytoplasm is a concentric spherical shell, and a homogeneous extracellular compartment is included. In both the LSS and the dMRI model, the nuclei all have the same radius, r, with an inner diffusivity, D_{nuc}, and refractive index, n_{nuc}. The LSS model considers all the volume outside the nuclei as a single compartment with refractive index, n_{cyt} while, in the dMRI model, the cytoplasm is contained in a cellular membrane with radius, R, and diffusivity D_{cyt}. The extracellular compartment in the dMRI model has a diffusivity, D_{ext}. The microstructural model binds LSS and dMRI models which represent the radius of the nucleus r, with a single parameter. Alongside that, the dMRI model can estimate the radius R, and the volume fraction, ψ, occupied by the cells in the tissue while the LSS model can estimate the ratio between the refractive indexes of nucleus and cytoplasm.

LSS signal model

The LSS experimental procedures were designed to enable the interpretation of the signal using the mathematical framework presented in section 2.1.4. The Mie Theory (MT) was adopted to generate the diagonal parameters of the scattering matrix, S_1 and S_2, required by equation 2.37. The parameters

S_1 and S_2 are related to the size of the nuclei r, and the refractive indexes n_{nuc}, and n_{cyt}. A single value of r was considered for all the scatterers, and the model was not considered suitable to estimate the numerical density of scatterers as the intensity of incident light was unknown. The equation 2.37 was fitted to the normalised experimental signal obtained by subtracting the spectra obtained from the orthogonal to the one from the parallel channel.

MT relates the microstructure to the scattering optical properties. This is implemented in the function M_{LSS} which connects a microstructure with the average scatterer radius r, the spread of the distribution of radii, σ, and refractive indexes ratio $m = n_{nuc}/n_{cyt}$, to a normalised scattering spectrum as

$$I_{\parallel-\perp}(\lambda) = M_{LSS,type}(r, \sigma, m), \tag{6.1}$$

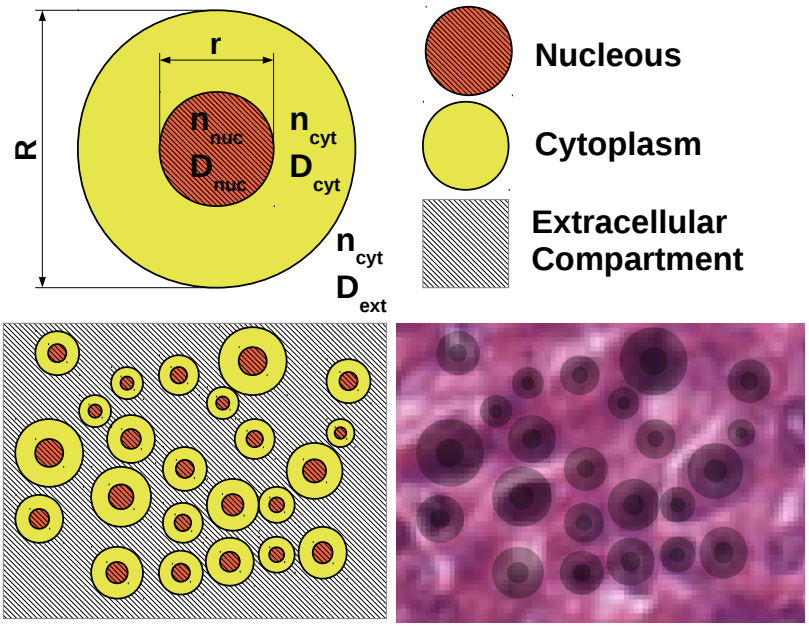

Figure 6.4: Scheme of the model representing the microstructure of the tissue adopted for the multimodality approach combining diffusion MRI Oscillating Gradient Spin Echo and Laser Scanning Spectroscopy.

where the intensity of the signal obtained by the subtraction of the two channels is $I_{\parallel-\perp}(\lambda)$ for each wavelength, λ. The subscription *type* indicates the distribution of sizes expected in the microstructure, and it could be set equal to *single* for a population of scatterers with the same radius (not requiring the parameter σ), *norm* for a Gaussian distribution, and *log-Norm* for a log-normal distribution of sizes. In the combined model, only the distribution *single* will be adopted.

The mathematical algorithm adopted to fit the signal requires a numerical integration of the contributions from scatterers of different dimensions to calculate the cumulative signal. The oscillations observable during the integration of several solutions of Mie theory have been studied in the past, suggesting that an integration over a discrete set of scatterer dimensions defined on a logarithmic set of intervals starting from the dimension of 100 nm and ending at 20 μm would offer a sufficient numerical accuracy [Wolf and Voshchinnikov, 2004]. The lower limit was established by considering that the microstructure below that threshold is outside the possible tail of the distribution of organelles of interest in this work. The upper limit is imposed by the degradation of computational efficiency in the approximation of Mie theory solutions for large shape factors ($x \gg 1$).

The selection of the initial guess in the minimisation algorithm is essential due to the periodicity of the functions obtained from Mie Theory which impedes a smooth minimisation process. The initial guess is defined by selecting the parameters corresponding to the spectrum from a pre-populated table closest to the experimental signal. Spectra were pre-calculated for 40 values of radius, and 60 values of refractive index ratio in order to populate the table. The final microstructural parameters were obtained in the LSS modality by fitting equation 6.1 to the scattering spectrum using a Levenberg-Marquardt with initial value of the parameter, λ_{L-M}, equal to 0.01. The parameters were fitted over a spectrum defined over 61 wavelengths originated by averaging bands of wavelengths obtained from the 2048 datapoints from the spectrometer measurement.

Diffusion MRI signal models

The signal obtained from the MR measurements was processed as discussed in chapter 5. The only signal model considered in this work is *Sph + She + Ball* where a spherical compartment represents the nuclei, the shell compartment the cytoplasm, and the extracellular compartment is described as an isotropic compartment. The model has been extensively discussed in 5.2.3. Although a variety of other microstructural models were discussed in the previous works, the only feasible approach enabling us to estimate both the dimension of radii and of cell membranes was to adopt the *Sph + She + Ball* dMRI model. Here, it is recognised that also the *Sph + Sph + Ball* model would offer a similar performance but the former was preferred as it ranked best in terms of BIC (see table 5.4) and there is no other advantage, at this stage of this work, in using other models studied in the previous chapter.

6.2.3 The combined model

The aim of this work is to develop a model informed by Laser Scattering Spectroscopy and diffusion MRI relying on Oscillating Gradient Spin Echo. Both techniques can characterise certain dimensional properties of the microstructure. LSS relies on a contrast mechanism based on the scattering properties while diffusion MR looks at the signal attenuation due to the confined diffusion of spins in the microstructure.

The combined model fits a linear combination of normalised signal errors calculated from the two modalities. The object function is a combination of the errors obtained by subtracting the signal generated with the modelled microstructural parameters, and the experimental signals as

$$\begin{aligned} Err(r, R, \psi) = w \, \| M_{LSS,single}(r, m) - C_{EXP} \| \\ + (1 - w) \, \| S_{Sph+She+Ball}(r, R, D_{nuc}, D_{cyt}, D_{ext}, \psi) - S_{EXP} \| \end{aligned} \tag{6.2}$$

where w is the weighting coefficient, $C = M_{LSS,single}(r, m)$ is the theoretical difference in intensity between the two channels generated by Mie theory, and

C_{EXP} the spectrum obtained from LSS measurements. The signal attenuation obtained in the diffusion MR experimental is S_{EXP}, and $S_{Sph+She+Ball}$ $(r, R, D_{nuc}, D_{cyt}, D_{ext}, \psi)$ is the echo attenuation modelled as described in section 5.2.3.

The combined model is described in figure 6.5. The object function in equation 6.2 is minimised by choosing the optimal microstructural parameters which reduce the discrepancy between synthetic signals and experimental measurements. The only parameter in common between the geometry of the LSS and dMRI models is the dimension of the cell nuclei r.

6.3 Results

6.3.1 Laser Scanning Spectroscopy experiments

Emulsion samples

The signals obtained from the emulsion samples are presented in figure 6.6. The experimental spectra measured through the two channels (parallel polarisation and orthogonal polarisation) are reported for the sample *Emulsion 1* in

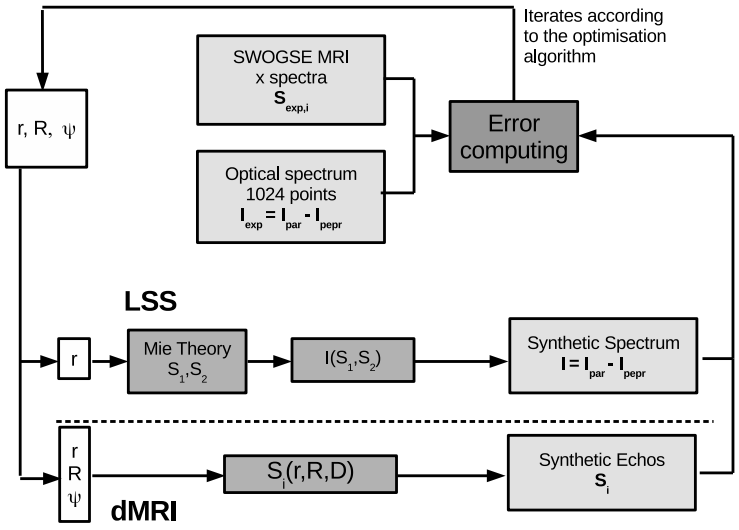

Figure 6.5: Scheme of the combined model adopted to extract microstructural information from the sample adopting LSS and diffusion MR.

figure 6.6(a). The data present the intensity of light measured at each wavelength, and multiple intensity peaks can be observed although a preliminary subtraction of a background spectrum had been performed. The presence of multiple narrow peaks reproduced in several spectra at similar wavelengths is likely to be related to electric noise in the detection device. Tests were performed to investigate the light background in the room which showed that the peaks are not related to background light. Note also the similarity between the two channels, suggesting that the scattering properties of the different layers might be similar.

The signal obtained by the subtraction of the two channels (orthogonal to parallel polarisation) is reported in figure 6.7(b). In these data, no filtration was introduced to eliminate signal noise. The spectra obtained from *Emulsion 1* and *Emulsion 2* are both similar with a maximum discrepancy of 5.1% at 787 nm principally related to noise. Sample *Emulsion 3* presents a marked curvature and the lower part of the spectrum (between 500-680 nm) shows larger fluctuations possibly compatible with the theoretical spectrum expected to be generated by a cluster of spheres according to Mie theory. The difference observed in sample *Emulsion 3* compared to the other two could tentatively be explained by the presence of a component of direct reflection from the surface of the sample.

The signals obtained from LSS were fitted with the signal model described in the previous sections and results are presented in figure 6.7. Here, instead of using the raw spectra as previously presented, signals were averaged to obtain a smoother spectrum and to reduce the number of wavelengths to be evaluated with Mie theory in order to improve computational efficiency. Data were initially filtered with an averaging floating window (5 nm wide) to eliminate the spikes discussed previously. Subsequently, a second averaging was performed and a spectrum defined on a subset wavelength was calculated. An example of inaccurate signal filtering could be observed at 582 nm where a remaining spike can be identified.

The fitting of an optical model assuming a microstructure with scatterers all of the same dimension is shown in figure 6.7(a). The fitting of the LSS signal is highly dependent on the choice of the initial guess due to the periodic

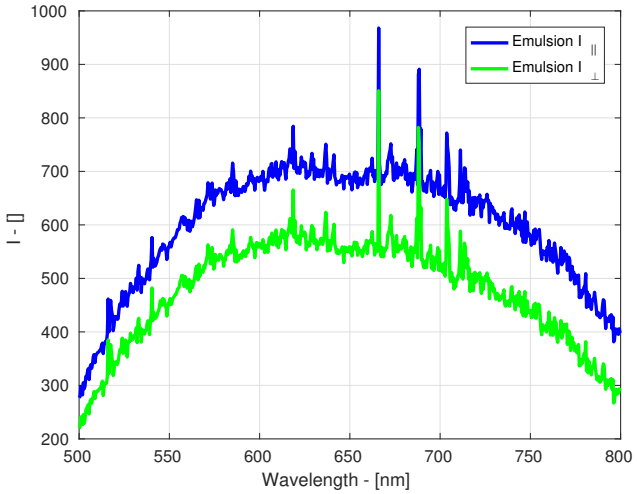

(a) Raw signal from each single channel

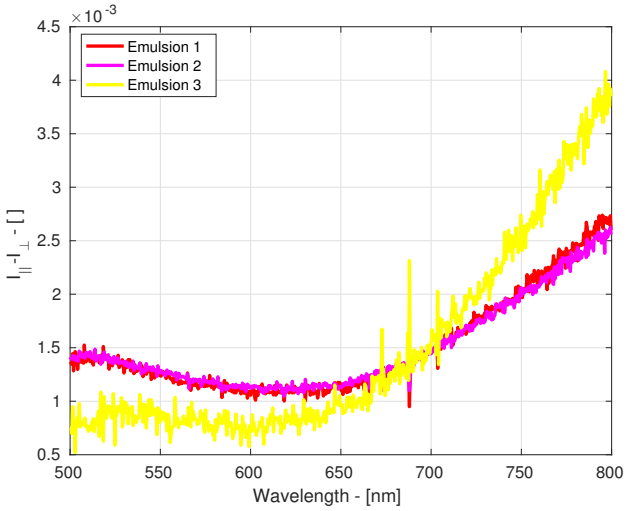

(b) Spectra obtained from the channel subtraction

Figure 6.6: Signals obtained from the measurements on three emulsion samples. In figure (a), the raw signals obtained from the two channels are reported, showing the number of counts per second at each wavelength with the spectrometer for sample *Emulsion 1* only. In figure (b), the spectra obtained from the subtraction of the two channels, calibrated and normalised, are presented for the three samples.

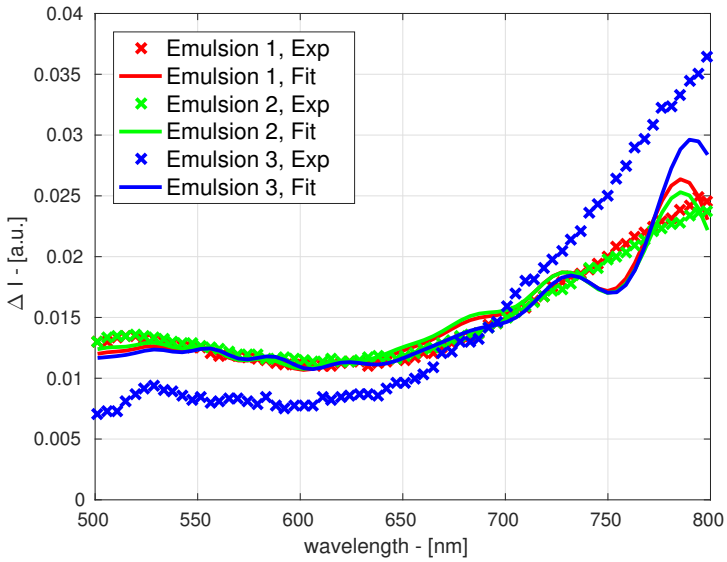

(a) Microstructure with all the scatterers of a single dimension

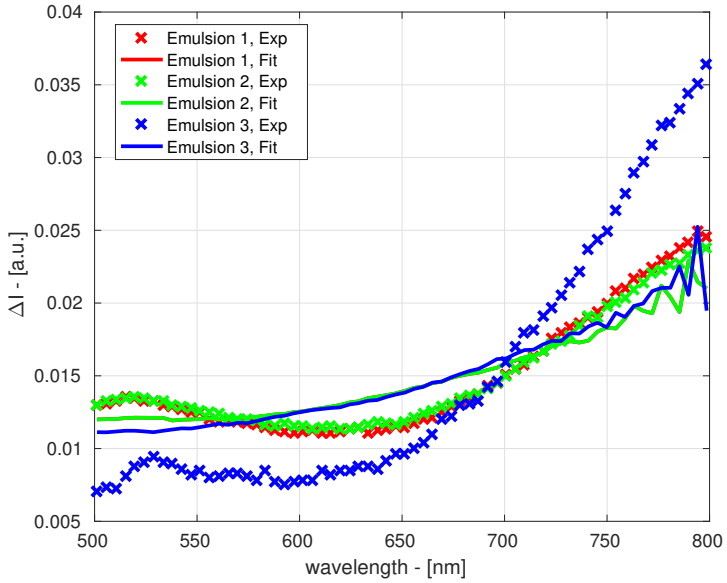

(b) Microstructure with the scatterers dimension assumed as a log-Normal distribution

Figure 6.7: The three signals obtained from the three emulsion samples were fitted with two signal models. In figure (a) Signals obtained from the measurements on three emulsion samples over the interval wavelength range between 500–800 nm. In figure (a), the fitting obtained assuming a population of scatterers with the same dimension is assumed. In figure (b), a population of scatterers with a dimension distributed according to a log-Normal distribution is presented.

nature of the solutions from Mie theory. The solutions obtained for the first and second sample differ minimally, but they fail to capture the continuity of signal by introducing large oscillations especially for larger wavelengths. The fitting of the signal from *Emulsion 3* is unable to capture the signal.

The fitting of an optical model assuming scatterers log-Normally distributed is shown in figure 6.7(a). For all the three samples, the model does not capture the oscillations at lowest frequency in the experimental signals as the initial increase of intensity with wavelength before 570 nm is not modelled. A set of spectra generated with the Mie theory model for the range of dimensions of scatterers expected was plotted (when the pre-compiled table was produced to facilitate the choice of the initial guess) showing that the model itself cannot generate suitable spectra to fit the signal in the present case.

Xenograft tumour samples

The experimental measurements obtained with LSS from the tumour samples *LS* and *SW* are reported in figure 6.8. Only marginal differences are observable between the signals obtained from the two cell lines below 680 nm. The spectra were initially normalised, and the differences in slope observed in the plots are partially related to the normalisation which weights also the signal at higher wavelengths. The spectrum recorded from *SW2* presents a higher noise connected to a lower intensity of light detected from each single channel, and it presents a maximum at about 700 nm preceded by a progressive increase of intensity at the lower wavelengths. The sample *SW2* is also the largest tumour adopted in the experiment, this should have improved the signal quality by eliminating any accidental effect from the background, suggesting that either the sample is partially corrupted or the presence of an excess of PBS might have deteriorated the signal. LSS measurements of the sample *SW2* will not be included in the following studies.

Literature suggested that an exponential decay in backscattering spectra should be expected from tumour tissues for wavelengths below 700 nm [Schuele et al., 2005, Hunter et al., 2006, Jacques, 2013]. The LSS technique is able to highlight important features from the microstructure in the superficial layers

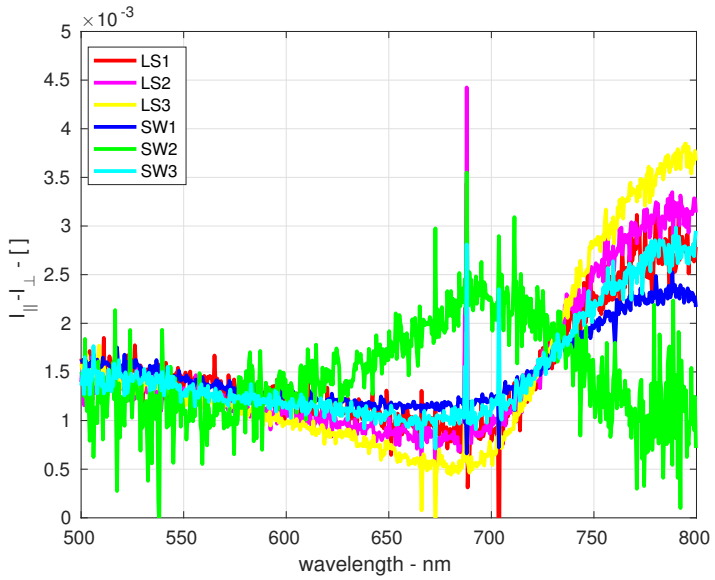

Figure 6.8: Signals obtained from the spectroscopic measurements in the *LS* and *SW* samples. A filtered version of the signals can be found in figure 6.9.

of the sample such as cellular organelles. This can lead to elaborate spectra where larger oscillations are present [Backman et al., 1999]. Given the prior knowledge of the spectra, it was considered appropriate to limit the study to wavelengths between 500-700 nm with the attempt to neglect the contribution to signal from components not directly related to nuclei.

The fittings of the LSS signal model over the filtered and reduced experimental spectra are presented in figure 6.9. The model assumed a Gaussian distribution of scatterer sizes. Preliminary investigations proved that the LSS signal model representing scatterers of a unique size was inappropriate due to the smoothness of the spectrum; therefore, a Gaussian distribution of scatterers size was assumed. *LS* samples present a steeper decay of the spectrum than the *SW*, and the model provides a good fitting for four samples although the experimental spectra show minimal oscillations which are not captured. The model cannot fit *LS3* accurately as the LSS signal model cannot reach the sufficient slope observed in the experimental spectrum. This is possibly caused by a contribution in the signal from scatterers larger than the ones predicted from the present distribution.

The ability of the LSS model to estimate the microstructural parameters by fitting a spectrum was further investigated with a MCMC algorithm. Results are presented in figure 6.10 where the average radius of the nuclei r, the standard deviation of the nuclei size distribution σ, and the ratio of the refractive indexes were analysed. The model suggests cells in the LS samples present nuclei with a smaller average dimension (LS: 1.09 μm, SW: 1.82 μm) while the spread of the distribution does not provide significant information. The large variability in the size distribution spread might indicate a reduced importance of the parameter r given the small range of dimensions on which the distribution is evaluated (10 nm–10 μm). The cell lines also appear to present different refractive indexes where the SW spectra were fitted to obtain an average value of 1.1205(0.003) while LS of 1.076(0.004). The expected refractive indexes of cytological components has been extensively discussed in literature, and the expected values of the parameter m should range between 1.03-1.11 [Maier et al., 1994, Brunsting and Mullaney, 1974]. This would suggest a estimate for m higher than expected for the SW cell lines. Finally, for the variables

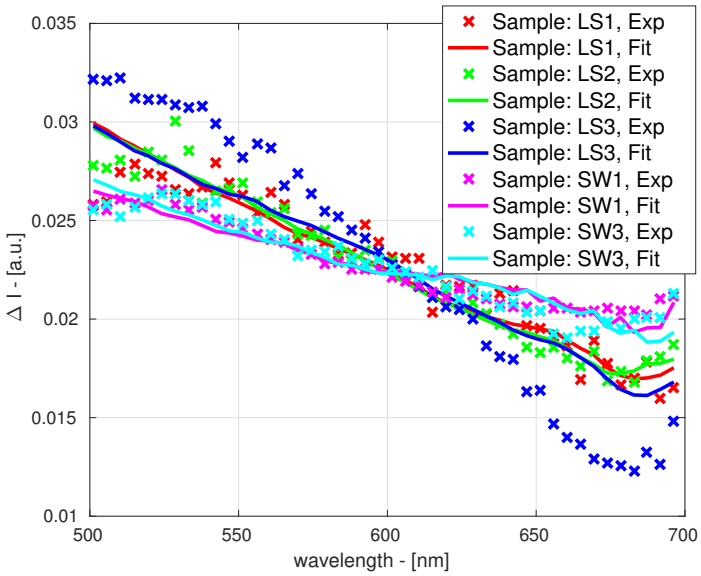

Figure 6.9: The five signals (limited to 500–700 nm) obtained from the tumour samples were fitted with a signal model representing a Gaussian distribution of scatterers.

representing the dimensions of the scatters, it should be observed that the experimental setup and the natural differences between the samples offer a larger variability than the uncertainty related to the LSS model.

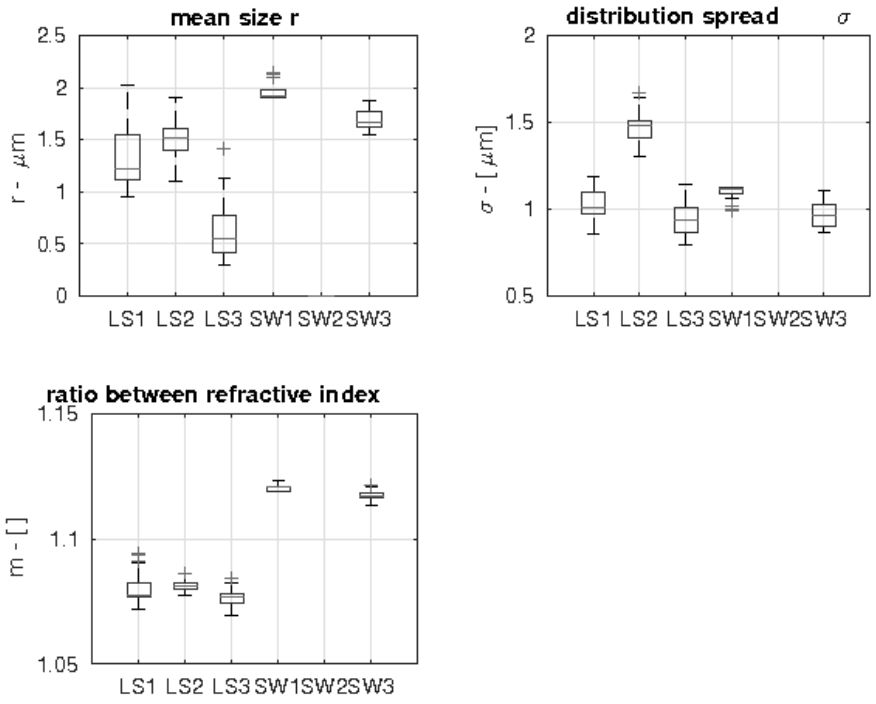

Figure 6.10: Analysis of the specificity of the LSS model performed with a MCMC algorithm. Results were calculated on a chain of 10,000 solutions.

6.3.2 Combined model applied on xenograft tumour samples

The experiments performed on the oil in water emulsion samples were only designed to attempt a validation of the technique and to estimate its accuracy. Consequently, Oscillating Gradient Spin Echo diffusion MRI measurements on the emulsion samples were not performed. Data were available from the work in chapter 3 where a Stimulated Echo gradient sequence was adopted, but the substantial differences in the nature of the two sequences introduces a

difficulty in comparing the two approaches. Finally, the application of OGSE to estimate the dimension of the oil droplets might be inappropriate given the low diffusivity (D = 0.0098 m^2/s) observed in oil.

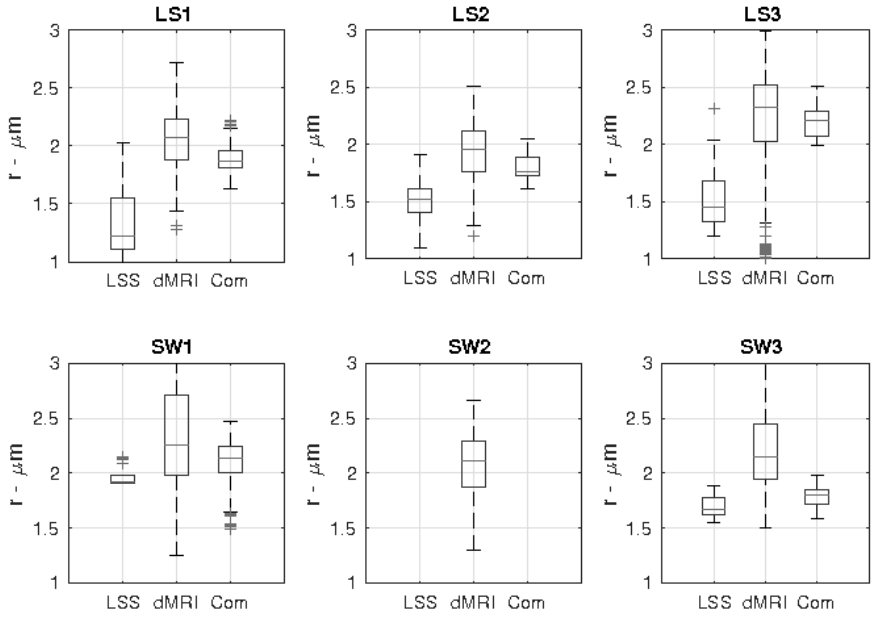

Figure 6.11: Analysis of the performance of the three models in estimating the size of the cell nuclei r (radius) in the samples. The analysis was performed with a MCMC algorithm where a chain of 10,000 solutions was studied. (*SW2* information is reported only when the dMRI signal model is required)

Figures 6.11, 6.12 and 6.13 show the results of the analysis performed with an MCMC algorithm on the variability of the estimates from the three models (LSS, dMRI and Combined). The only microstructural parameter in common between the LSS and the dMRI model is the size of the nuclei r, but the radius of the cell membranes R (from the dMRI signal model) and the ratio between the refractive indexes m (from the LSS signal model) are also presented. The boxplots obtained from the estimation of the dMRI signal are conceptually different from the information reported in figures 5.13-5.15 (chapter 5) where the variability of the fitting across the voxels of the sample was described. Here, the MCMC algorithm estimates the ability of the model to characterise

the microstructure from the experimental signals obtained by averaging over all the available voxels from each slide.

The results presented in the previous section were obtained from an LSS signal model assuming a Gaussian distribution of the scatterers dimension. Although it has been stated that the LSS signal model relying on a single dimension of the scatterers does not provide an accurate fitting, the combined model assumes that all the nuclei have the same dimension. Assuming a distribution of dimensions would have lead to a number of the nuclei in the tail of the distribution larger than the cell itself which would create an unrealistic geometrical mismatch between the two models.

Figure 6.11 shows the variability of the estimates of the nuclei radius r obtained with the three models. The LSS signal model separates the two cell lines, but the very low variability of the estimates of refractive index ratios

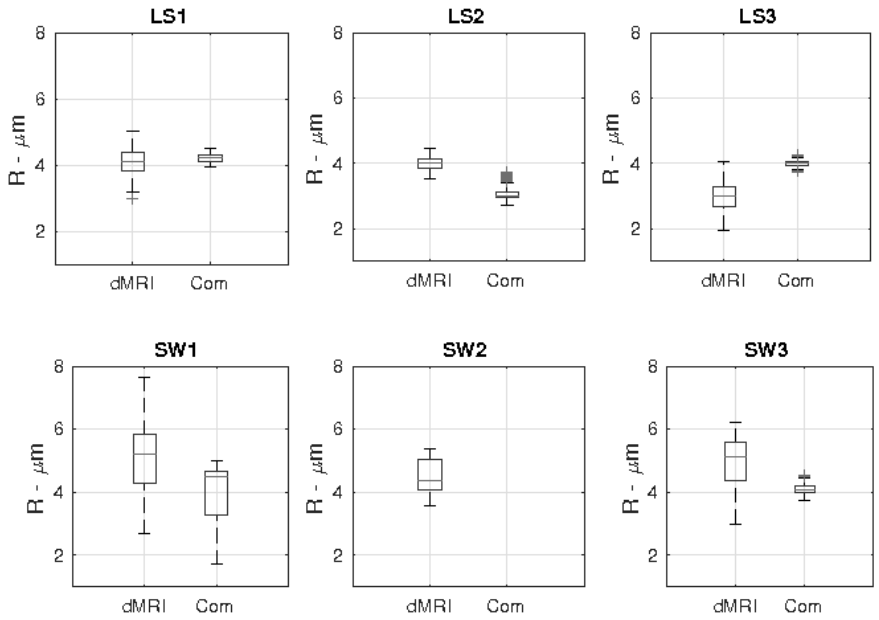

Figure 6.12: Analysis of the performance of the three models in estimating the size of the cell membrane R (radius) in the samples. The analysis was performed with a MCMC algorithm where a chain of 10,000 solutions was studied. (*SW2* information is reported only when the dMRI signal model is required)

m presented in figure 6.13 suggests that the model has been unable to obtain a global minimum despite the different L-M scaling factors selected in the investigation. The sensitivity of the estimates of m from the quality of the signal increases in the combined model where the information obtained from the dMRI measurements force the solution outside the local minimum. The accuracy of the estimates of the nuclei radius is instead improved by the information offered by the LSS signals as reported in table 6.1.

The figure 6.12 shows that the variability of the cell membrane radius estimate R in the combined model is reduced compared to the dMRI model. This could be related to the effect on constraining the dimension of the inner (nucleus) radius in the dMRI model by adopting additional information obtained from the LSS signal. The work presented in chapter 5 suggested that SW cells

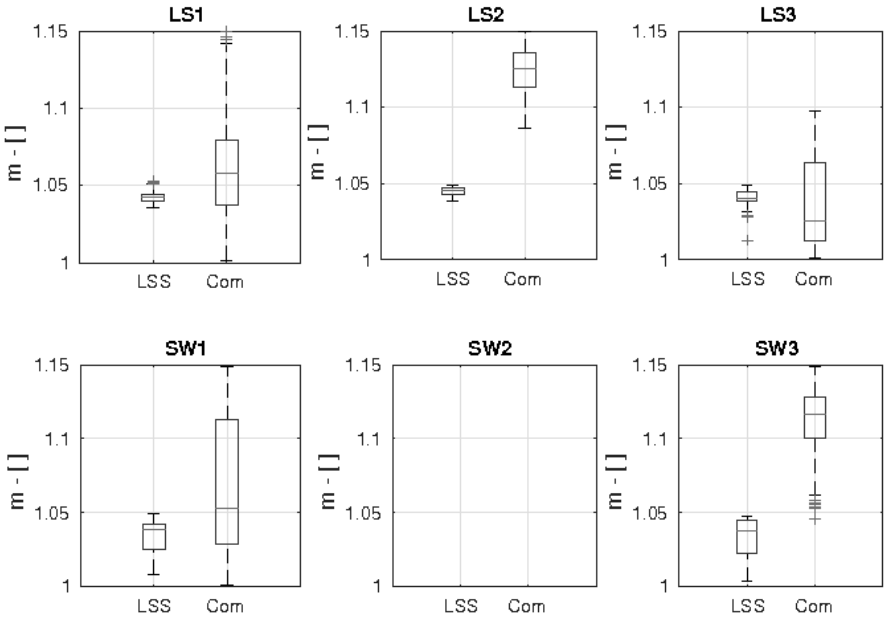

Figure 6.13: Analysis of the performance of the three models in estimating the ratio between the refractive indexes of nuclei and cytoplasm in the samples. The analysis was performed with a MCMC algorithm where a chain of 10,000 solutions was studied. (*SW2* information is reported only when the dMRI signal model is required)

	LS1	LS2	LS3	SW1	SW2	SW3
Opt r [μm]	1.34(0.30)	1.51(0.18)	1.50(0.26)	1.96(0.08)	N/A	1.70(0.11)
Opt m []	1.042(0.004)	1.045(0.003)	1.041(0.006)	1.034(0.011)	N/A	1.034(0.012)
dMRI r [μm]	2.06(0.25)	1.93(0.25)	2.20(0.55)	2.30(0.50)	2.09(0.30)	2.21(0.38)
dMRI R [μm]	4.14(0.38)	3.99(0.20)	3.22(0.46)	5.06(1.036)	4.49(0.51)	4.90(0.83)
Com r [μm]	1.89(0.11)	1.81(0.10)	2.22(0.14)	2.09(0.22)	N/A	1.78(0.09)
Com R [μm]	4.21(0.14)	3.06(0.19)	3.99(0.08)	3.956(1.040)	N/A	4.10(0.15)
Com m []	1.061(0.033)	1.124(0.016)	1.036(0.028)	1.067(0.046)	N/A	1.113(0.020)

Table 6.1: Table summarising the best estimate and the variability of the estimates (in brackets) for the microstructural parameters studied in the three models. The estimates of the nucleus radius r, the cell radius R, and the refractive index ratio m are presented for the LSS, the dMRI and the combined (Com) model.

were larger than *LS* on average, with an estimated difference of 2.0 μm. Previous histological investigations did not support this statement suggesting that this trend was inverted. Here, the estimates from the combined model do not enable a separation of the two cell lines based on their size. This degradation of performance is possibly connected to the limitation of the LSS signal model.

The figure 6.13 reports the results of the MCMC on the refractive index ratio m. The values of m estimated by the combined model result are unrealistic for the samples *LS2*, *SW1*, and *SW3*. This is a clear indication of the limitation of the LSS signal model assuming a single dimension of the scatterers to fit the signal.

6.4 Discussion

Previous works presented backscattering spectra from phantoms and tumours acquired with both a polarised technique isolating superficial layers and spectroscopic techniques [Amelink et al., 2004, Schuele et al., 2005, Ramachandran et al., 2007, Kiyotoki et al., 2013, Amelink et al., 2003]. Over the years, LSS had been evolved to extrapolate additional information on the cytological microstructure of the sample. Validations of these techniques were generally reliant on phantoms where scattereres with a single dimension were adopted, and the obtained spectra easily matched the predictions from Mie theory. Those spectra were showing sinusoidal oscillations at shape factors close to unity ($x = 1$) which progressively disappeared for larger shape factors [Backman et al., 1999, Amelink et al., 2004]. Here, the emulsion sample shows a large

distribution of scatterer dimensions ranging from the hundreds of nanometres to a maximum size that could be in the order of the tens of microns (i.e. $x \approx 10$). The nature of the emulsion adopted makes it difficult to retrieve similar experiments in literature.

The emulsion adopted in this work was discussed in the previous chapters. It has been selected for its relatively well-known microstructure, for its homogeneity and because it offers contrast both for dMRI experiments through the diffusion of oil in the droplets, and for optical scattering techniques. As discussed in section 6.3.1, the experiments suggest that homogeneity might persist in all the layers of the sample. This is unusual in LSS applications which aim to separate different parts of the tissue.

The results highlighted the difficulty for the LSS models to fit the spectra obtained from the experiments on the emulsion. The measured signals show a smooth spectrum generally indicating a continuous distribution of scatterers at the smaller sizes, but the large (low frequency) oscillations seem also to indicate that part of the signal originates from a limited number of scatterers with a single dimension higher than the range of expected sizes. If this argument is accepted, the oscillations are connected to scatterers with a size in the order of the tens of microns which can be explained by a possible clusterisation of the droplets in the superficial layers as already observed in the Confocal Laser Scanning Microscopy images presented in section as a consequence of temperature instability 3.3.4 [Vanapalli et al., 2002]. Previous indicative CLSM showed that no alterations were observed in the dimension of the droplets with the evolution of time while the droplets in close contact might have moved and clusters disassembled.

In consequence of the reported arguments, although an analysis of the specificity of the estimates on the experimental data was performed on the experimental data, we consider it inappropriate to rely on its results. The ability of a model to extrapolate information from a measurement depends on the ability of the model to fully represent the mictrostructure of the sample, and the strong dependence on the choice of the initial guess might produce misleading conclusions by suggesting an unrealistically good performance.

The spectra obtained from the tumour samples follow a quasi-exponential

decay below 700 nm, then an increase appears at higher wavelengths. A smooth spectrum showing a linear or logarithmic decay has been partially observed in previous works on real tissues while an oscillating spectrum was observed on epithelial tissues where the isolation of backscattering from large nuclei was possible [Backman et al., 1999, Kiyotoki et al., 2013, Amelink et al., 2003]. Similarly to emulsions, xenograft tumours can be expected to have a degree of homogeneity of the cytological structure as a consequence of the biology. Xenograft tumours might become inhomogeneous when they grow to a dimension where vascularisation creates area of hypoxia [Weinberg, 2013, Laufer et al., 2012]. In the present study, cells were injected sub-cutaneously, and tumours grew progressively with a dense cellular packing being encapsulated within connective tissue. The xenograft tumours have a well defined boundary enabling us to consider the surface of the tumours to be microstructurally representative of the inner part of the tumours.

The characterisation of the microstructure adopting an LSS technique presents a first challenge to avoid the direct reflection of light. While in the experiments on the emulsion samples direct reflection was avoided by tilting the beamsplitter to an angle larger than 90 deg, the rounded shape of the tumoural samples forbid a full avoidance of direct reflection in all the points. The presence of layers of water from the PBS solution was minimised to avoid reflection from water and a visual inspection was conducted showing that no evident reflection was observable. Nevertheless, the presence of a minimum component of direct reflection should be expected, but a dependence of the spectrum on the refractive index of water (contained in the PBS) is not observed in the signal [Thormählen et al., 1985]. In all the cases, the spot of light was fully projected onto the sample, and where possible, it was pointed at obliquous parts of the surface to avoid reflection. The cumulative signal was collected through an optical fibre with a numerical aperture sufficient to avoid the collection of unwanted light from external sources, but the detection of unwanted light from elements in the experimental setup was possible as a second collimator was not available for excluding the detection of light outside a specific angle.

A second challenge is that LSS techniques rely on an accurate calibration.

Additionally, the small differences between the spectra measured from the two channels require a high SNR in order to be able to discriminate the contribution from the superficial layers. The limitations in the experimental setup, including the quality of the optical components, suggested an application limited to a range of wavelengths between 500–800 nm. This limitation is mainly introduced by the operative ranges of the parts and it is often related to the performances of the anti-reflex coating. Finally, the distance of the sample from the detector due to the dimension of the parts reduced the power of the signal detected introducing a low SNR.

The presence of a contribution of absorption to the spectrum was disregarded in this work following a well established approach in literature for LSS [Backman et al., 1999]. The subtraction of the signals from the two channels would lead us to observe only the contribution of light from the superficial layers which are generally not characterised by a high concentration of dyes. Additionally, haemoglobin is expected to be removed in ex-vivo measurements, eliminating the peaks around 800 nm.

The work conducted on the tumours should accept that the microstructure contains a higher degree of complexity than in epithelial tissues. The latter tend to be composed by densely packed layers of cells with minimal extracellular structures. Here, the LLS model is likely to fit the signal generated by additional features in the sample. The smoothness of the signal suggests that a large number of small sized components (i.e. collagen and organelles) contribute to it. The large oscillations observed after 700 nm might be a final indication that the extracellular microstructure is another key contributor which is also supported by a larger difference in the maximum in the *LS* cell lines compared to *SW*. The spectrum obtained from the sample *SW2* should also be a warning to indicate the complexity in the use of this technique on samples which are not epithelial tissues.

The work suggests that the use of a model informed by two modalities might improve the accuracy of microstructural estimates. The work relied on six fixated xenograft tumour samples, and the preliminary results suggested that the poor fitting of LSS models does not enable us to draw specific conclusions. The combination of the two models reduces the uncertainty on the estimate

of the nuclei size r, but also reduces the uncertainty on the cell size obtained from the dMRI model only. This is potentially related to the limited influence of the dMRI signal originated from the nuclei compared to the component from the cytoplasm. The best estimate of the cellular size obtained from the MCMC algorithm is similar in magnitude to the average estimate obtained pixel-wise in chapter 5, but it fails to capture a difference between the two cell lines. The LSS modality is unable to capture the effects of the microstructure on the signal, generating large variations which are increased by the use of a combined model proving that the fitting of the model is obtained by non-physical alterations of the refractive index parameters.

The combination of the two modalities suggest that the quality of the sample might be sub-optimal. Possibly, in-vivo or freshly excised tissue might provide a more clear understanding of the dMRI signal being able to rule out a possible effect from the fixation or the deterioration of the tissue. Additionally, both the single modality signal models, and the combined model appear to predict similar nuclei dimension with variations across the different cell lines that become statistically significant. The dimension of the nuclei in histology is a key indication of the state of the tumour, but it is a fact that the presence of multiple nuclei and the different shapes or position that nuclei can have in the cell can alter the dMRI signal and require a completely different model. Additionally, the refractive index of the nuclei tends to vary according to the type of cell and their expression. In conclusion, the dimension of nuclei might not be optimally investigated by this method.

6.5 Conclusions

The work presented cannot draw robust and generalisable conclusions. In a first instance, a sample with a simpler microstructure should be adopted to validate the LSS technique. A test object with microscopic globules suspended in a matrix which is stable over time and offers both optical and MR contrast is required. Secondly, the method should be applied to tissues freshly excised where the fixative has not risked corrupting the microstructure. Finally, the homogeneity of the tumour sample should be tested to enable an accurate

segmentation of the information contained in the data. These conditions are required along with a more careful design of the detection system to avoid any unexpected contamination of the spectrum detected from other sources.

Part IV

Conclusions and future work

Chapter 7

Conclusions

This work aimed to describe the advantages in combining optics and MR physics to characterise the microstructural features of samples. Chapters 3 and 4 discuss the advantages of combining diffuse optical spectroscopy and diffusion NMR, and chapter 5 analyses different signal models to fit diffusion MRI and oscillating gradients echo on ex-vivo colorectal tumours.

7.1 Investigation of multimodality approaches on samples

The approach presented in chapter 3 requires a-priori knowledge of optical absorption properties of the microstructure. This work proved the enhanced accuracy of microstructural estimates offered by a combination of dNMR and DOS over the separate modalities, but it can only be applied when simple microstructural models can be applied. The accuracy of the estimate of the the radius r, in common between the two modalities, shows a substantial improvement when the two modalities are combined. This suggests a mechanism of mutual correction of fitting, tunable on the strength of each modality. Additionally, the volume fraction ψ and the distribution spread σ. estimated by a single modality only, show an increase in accuracy in prediction when a multimodality approach is applied. This second element is related to the introduction of constraints over the common parameter r, due to the additional

modality. Finally, the reduction of MCMC chains amplitude indicates that the multimodality approach leads to additional specificity of the model over the data.

The approach discussed in chapter 4 removes the necessity of a-priori known parameters. The implementation of an optical model based on the spectrum of apparent scattering coefficient enables the volume fraction ψ, along with the mean r and spread σ of the distribution of microspheres radii to be estimated. The combination of optical signal with the dNMR echo attenuation measurements improves robustness and accuracy as occurred in chapter 3. The absence of a-priori known parameters reduces the estimate accuracy compared to the previous approach, but allows to apply this method to generic samples.

The diffuse optical spectroscopy technique presents resolution limitations. The signal, in order to be in a diffuse regime, requires a sample of at least 10-20 mm depending on the scattering properties. As a consequence, inhomogeneities in the microstructure will be averaged over voxels with edges of around one centimetre. Technology limits the resolution also as a consequence of the time resolution of photon pulses generated by *MONSTIR* systems. Alternatively, different optical modalities can be considered, such as laser scattering spectroscopy which is able to map down to few hundreds microns below the the surface.

The sample presented in these works have a tissue like microstructure. The presence of microspheres ranging over dimensions from hundreds of nanometers to few microns mimics the presence of nuclei and organelles and proves the concept over spherical scatterers such as cells. Additionally, the presence of proteins in the dispersion medium introduces the scattering related to collagen and extracellular structures in a real tissue. At the same time, the complexity of the microstructure in the sample proved to be excessive for offering a ground truth for the validation of the performances of the combined approach. The charateristics of the signal offered in the optical modalities could not be completely matched to the microstructure, introducing an uncertainty in itself.

7.2 Investigation of signal models for oscillating gradients spin echo MR sequences

Chapter 5 discusses a set of microstructural models fitting oscillating gradient spin echoes MR measurements over fixed xenograft tumours. Fixation alters the diffusivity within the microstructure, but it preserves the geometry of the microstructure. A gradient sequence based on a repeated pattern enables to tune its properties to study the microstructure at different scales. The first result suggests that the two cell lines cannot be distinguished by their mean diffusivity only, but higher order models are required. A ranking based on Bayesian information criterion shows that restricted diffusion compartments are necessary to describe the signal accurately. The models performing best are those directly related to geometrical features of the microstructure. Finally, the microstructural parameter estimates obtained from the the best model fail to match histology, but they show differences between the two cell lines.

The work presented shows the advantage in considering integrated multimodality approaches to obtain a new paradigm in microstructural imaging. Chapter 5 sets the basis for the combination with optical spectroscopy performed with colonoscopy. The work, which is already at an advanced stage, will be discussed in section 8.1. The accurate knowledge of the physics from each imaging technique enables to exploited the strength of each modality in the estimation of portion of microstructural features. The difference in cost and timing between diffusion MR and optical spectroscopy offers room for connecting the protocol to save time and improve accuracy. Optics can provide broad information over the entire sample at larger resolutions while MRI can offer very high resolutions but long acquisition times. Moreover, optics offers contrast from the nano- to the microscale while diffusion MRI offers contrast at larger scales such as the microns and tenth of microns.

7.3 Investigation of multimodality approaches on tumours

The work presented in chapter 6 aimed to extend the approach introduced on the samples to a real tissue. The approach fails to reduce the uncertainty on the estimates of the common parameter, but enables to obtain a reduced uncertainty on the additional parameters obtained with the dMRI technique only. This is a proof in principle that the performances of a model informed by multiple techniques is dependent on the ability of the single modality models to interpreter the problem. A model with a reduced ability to interpreter the microstructure or an experimental approach which is sensitive to calibration or lacks of repeatibiliy can penalise the performances of the combined model.

The model informed by LSS and dMRI still shows the potentiality to prove that the combination of information from two modalities can improve the accuracy of microstructural characterisation. Here, the complexity of the emulsion phantom did not enable a complete understanding of the properties of the optical modality, and the sensitivity of the LSS experimental work to calibration suggested that further work is required. Finally, the choice of ex-vivo non-epithelial tissue proved to be sub-optimal, where both the complex cytological microstructure of a fully developed cancer lesion and the possible effects of fixation did not enable to draw a full set of conclusions.

Chapter 8

Future works

8.1 Multimodality on in-vivo colorectal tumors

The work presented in chapter 6 suggests that the combination of diffusion MR relying on oscillation gradients spin echoes and Laser Scattering Spectroscopy may be a viable approach to diagnose colorectal cancer. Two interesting directions of work are the investigation of the cytological structure in more detail and the study of the vascularisation in the model.

The work presented a focus on microstructural properties limited to a cytological scale and to the dimension of the nuclei. The complexity of a tumour tissue would suggest an investigation of additional elements in the cells such as organelles [Schuele et al., 2005]. The dimension of organelles are an indication of the pathological condition of the tissue [Weinberg, 2013]. A work was presented as a continuation of the optical approach adopted in chapter 6, where a microscopic spectroscopy technique, single-cell partial-wave spectroscopy, provided insights into the statistical properties of the nanoscale architecture of biological cells [Subramanian et al., 2008]. This additional approach, along with the possible information that could be fed into the diffusion MRI model, might provide additional insight on tumours at early stages, when a differentiation has not yet occurred. Unfortunately, due to the well-know heterogeneity of colorectal cancer at later stages, an optical modality looking only at a superficial layer might not be sufficient to cross-inform a multimodality approach.

A second approach could constitute in the use of information on the vascularisation of the lesion to improve diagnosis at following stages. The vascular structure is a good indication of the evolution of the tumour and has been extensively studied [Weinberg, 2013, Leunig et al., 1992]. Photoacoustic techniques have already been used to investigate the evolution of blood vessels during tumour treatments and provided a good mapping of the lesion and of the vascular properties [Laufer et al., 2012]. Similarly, studies were performed on prostate diagnosed patients with an approach named VERDICT, able to provide a cytometry with diffusion weighted MRI able to offer information on introduced vascular, extracellular, and restricted Diffusion in tissue [Panagiotaki et al., 2015]. A photoacoustic technique and the VERDICT approach might provide scope for an integrated model able to stage tumours with accuracy. A possible combined model might require a more complex conceptualisation of tissue than the one presented in chapter 6, and a mathematical model of the evolution of the tumour might be required.

8.2 Fast histology device

Computer aided surgery is becoming a standard for in many hospitals. Along with the computer support to the actual surgery, computer aided diagnosis, and surgery or treatment planning are becoming an important field of research. One of the main topics is the identification of tissues condition during surgery. At the present time, tissues extracted during surgery, require to be examined with classic histology, but allows results to be obtained only when the surgery is over.

The combination of two modalities can be considered for the real time characterisation of the microstructure in surgery excised tissues. The characterisation of microstructure on a homogeneous sample can be performed using a combination of diffusion NMR and diffuse scattering spectroscopy. An efficient measurement, can offer an automatised indication of the tumour and of the stage.

The approach would exploit an *ad-hoc* system with optimised wavelengths and gradient sequences. The acquisition time of dNMR data can be reduced

down to few minutes with the use of an high field, high gradient and less expensive NMR system instead of a standard MRI system. The selection of appropriate sequence parameters could offer additional reduction of time, which will offer intra-surgery information which can be used, real time, by the surgeons.

To obtain a reliable system, direct study and characterisation of the performances of the model over the tissues of interest is required. Tumour staging is already performed with the use of histology, and a correspondence of the results from a potential fast histology device should be proved.

Appendix A

Appendix

A.1 Optical properties

A.1.1 Cross-sections from Mie theory

Absorption and scattering coefficients can be derived from a solution of Maxwell equations of the field around scatterers. Mie theory provides a solution of electromagnetic field around spherical (or elliptical) particles, and ultimately the values of cross-section for scattering and absorption.

Cross-sections are computed starting from an expansion of Maxwell equation solution in spherical harmonics. Its solution leads to the series a_n and b_n of expansion coefficients [Ishimaru, 1978]. Consequently, the absorption cross-section becomes

$$\sigma_{abs} = \frac{\pi}{x^2} \sum_{n=1}^{N} (2n+1)[Re(a_n) - |a_n|^2 + Re(b_n) - |b_n|^2] \tag{A.1}$$

and the scattering cross section

$$\sigma_{sca} = \frac{2}{x^2} \sum_{n=1}^{N} (2n+1)(|a_n|^2 + |b_n|^2). \tag{A.2}$$

Here, x is the wave factor which is proportional to the ratio between scatterer size and wavelength (see section 2.1.3), and N is the number of terms in the

expansion [Graaff et al., 1992, Hill, 2003, Ishimaru, 1978]. As a matter of fact, the main dependence occurs on x and m, but works from [Graaff et al., 1992] suggest that, on a limited interval of values such as $g > 0.90$, $5 < x < 50$ and $1 < m < 1.1$, approximated versions of the expression A.2 exist.

Also the extinction coefficient is can be derived directly from Mie theory as

$$\sigma_{ext} = \frac{2}{x^2} \sum_{n=1}^{N} (2n+1) Re(a_n + b_n) \tag{A.3}$$

or as the sum of absorption and scattering cross sections [Bohren and Huffman, 2008, Ishimaru, 1978].

All the previous cross sections can be related to the actual size of scatterers as

$$Q_{sca} = \frac{\sigma_{sca}}{\pi a^2} \qquad Q_{abs} = \frac{\sigma_{abs}}{\pi a^2} \qquad Q_{ext} = \frac{\sigma_{ext}}{\pi a^2}, \tag{A.4}$$

where a is the radius of the scatterer, and Q indicates the normalised cross-section [Ishimaru, 1978].

A.1.2 Phase function

The phase function is the analytical representation of the distribution of directions of scattered photons. Phase function formulations depend on the physics of the problem, but historically, the first fields requiring a model of scattering based on phase functions were meteorology and astronomy [Henyey and Greenstein, 1940, Hulst and Van De Hulst, 1957]. The complexity of scatter in biological media, and the presence of multiple scattering reduces the advantage of using advanced models [Ishimaru, 1978]. Henyey–Greenstein (H–G) phase function, $PH-G$, is commonly adopted across many disciplines, and it is obtained from the expansion of Legendre polynomial as

$$P(cos\theta) = \sum_{l=0}^{2N-1} (2l+1) \chi_l P_l(cos\theta) \tag{A.5}$$

where θ is the angle between incident and scattered photon, P_l are Legendre polynomial of order l and χ_l are linear coefficients. For Henyey-Greenstein,

setting $\chi_l = g^l$ and considering the first terms of the expansion, the well-know expression

$$P_{H-G}(\theta) = \frac{(1-g^2)}{4\pi} \frac{1}{(1+g^2-2g\,cos\theta)^{3/2}} \tag{A.6}$$

is obtained where we have

$$g = \langle cos\theta \rangle = \frac{\int P(u) cosu \mathrm{d}u}{\int P(u) \mathrm{d}u}, \tag{A.7}$$

and $0 < g < 1$ [Prahl et al., 1989, Henyey and Greenstein, 1940, Ishimaru, 1978].

Modified version of equation A.6 can improve modelling of specific problems. A first work presents a backscattering model with a linear combination of two Henyey–Greenstein phase functions, P_{DHG}, as

$$P_{DHG}(\theta, \alpha, g_1, g_2) = \alpha P_{HG}(\theta, g_1) + (1-\alpha) P_{HG}(\theta, g_2)$$

where α is a weighting factor and the other parameters can be intended as in equation A.6 [Toublanc, 1996]. An advanced model has been presented by Cornette and Shanks [Cornette and Shanks, 1992] expressed in Legendre series

$$\begin{aligned} P_{HG*}(\theta, g) = \frac{3}{2} \frac{1}{2+g^2} \sum_{i=0}^{\infty} \Bigg(& \frac{l(l-1)}{2l-1} g^{l-2} \\ & + \left[\frac{5l^2-1}{2l-1} + \frac{(l+1)^2}{2l+3} \right] g^2 + \frac{(l+1)(l+2)}{2l+3} g^{l+2} \Bigg) P_l(\theta) \end{aligned} \tag{A.8}$$

where P_l are Legendre polynomials of order l. The number of terms in the series increases with the complexity of the geometry. Simulation of slabs with thin multiple-layers can achieve a neglectable error using one or two terms only. Asymmetric geometries require additional terms [Irvine, 1965].

In conclusion, many authors have presented studies on the anisotropy of scattering. Complex models tend to be necessary in specific applications, but biological tissues are highly scattering which tend to randomise photon propagation. As a consequence, H–G model presented in equation A.6 is generally the standard for photon migration in biological materials.

A.2 Model and statistics

A.2.1 Probability distribution functions

This work aims to define the distribution of size of different elements in the microstructure. The best approach is to describe the distribution of their size based on the concept of probability distribution function (PDF) [Johnson and Wichern, 2002]. These functions represent the probability to observe an element of a certain size in the sample. The size of each element is defined by the variable a, specifically representing the radius of the sphere. Consequently, the average size of the particle, r, and the spread of the distribution, σ, are the two parameters of interest.

Single value

The simplest probability distribution is the degenerate case where all the extraction have a single value r. Given the value r as the only possible value, the distribution of probability becomes

$$p_{Single}(a; r) = \delta_r(a) \tag{A.9}$$

where $\delta_r(a)$ is the delta function centered in r [Khuri, 2004]. As definition of the delta function itself, the variance of the distribution tends to zero; therefore, $\sigma = 0$.

Gaussian distribution

The most common PDF is the Gaussian distribution. The Gaussian distribution is

$$p_{Normal}(a; r, \sigma) = \frac{1}{\sigma\sqrt{2\pi}} \exp(-\frac{(a-r)^2}{\sqrt{2\sigma^2}}) \tag{A.10}$$

where the distribution of a is centred in r and with a spread represented by the standard deviation of the Gaussian distribution, set to σ.

Log-normal distribution

The log-normal distribution is very common in emulsion and is a transformation of the Gaussian distribution. The log-normal PDF is

$$p_{logNormal}(a;\theta_1,\theta_2) = \frac{1}{\theta_2\sqrt{2\pi}}\exp(-\frac{(lna-\theta_1)^2}{\sqrt{2\theta_2^2}}) \tag{A.11}$$

where the two parameters (θ_1, θ_2) are related to r and σ through the transformations

$$r = log(\frac{m^2}{\sqrt{\theta_2^2+\theta_1^2}})\sigma = \sqrt{log(\frac{\theta_2^2}{\theta_1^2+1})} \tag{A.12}$$

providing the parameters required.

Gamma distribution

The final distribution considered is the Gamma distribution. It is an asymmetric distribution defined only for positive values of a. The probability distribution function is defined as

$$p_{Gamma}(a;k,\theta) = \frac{1}{\Gamma(k)\theta^k}a^{k-1}\exp(-\frac{a}{\theta}) \tag{A.13}$$

and the parameters (k, θ) can be described as

$$r = k\theta\sigma = \sqrt{k}\theta \tag{A.14}$$

providing the final values of microstructural parameters [Papoulis and Pillai, 2002]. Gamma distribution finds good applications because of its only-positive definition, suitable to describe dimensions.

A.2.2 Bayesian information criterion

The Bayesian Information Criterion (BIC) is utilised in the ranking of teh performances of models within a finite set. The BIC indicates the ability of the model to fit the data, and it weights the likelihood and the number of degrees of freedom of the model. The BIC penalises models with a high

Figure A.1: Probability distribution functions for the four cases considered with a mean $r = 2$, and $\sigma = 1$.

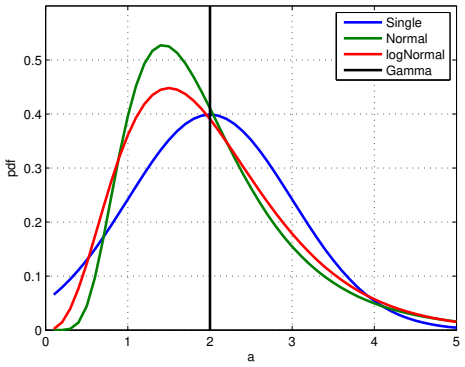

number of free parameters as they will tend to overfit. On the opposite, BIC favorites models leading to small fitting error.

The definition of BIC varies depending on the application. In this work, the definition based on the Mean Square Error (MSE) is considered. The BIC is obtained as

$$BIC = N_{DATA}\, log(MSE) + k log(N_{DATA}) \tag{A.15}$$

where MSE is the MSE over all the data in the dataset. The number of points in the dataset is indicated as N_{DATA}, and the number of degrees of freedom is k. Lower values of BIC correspond to a better performing models.

A.2.3 Numerical and experimental computations

The experimental signals are characterised by the Signal Noise Ratio (SNR). The definition of SNR depends case case by case, but the main two distinctions occur when there is a model fitting the signal or when the signal is standing-alone. When a model is defined, say the experimental signal M_i and t_i the variable changing between the different measurements at the measured condition i.e. time or diffusion time. Say exists a model $S_i = S(t_i)$ the signal, the

value of SNR can be expressed as

$$SNR = \sum_i \frac{M_i}{|M_i - S_i|}, \tag{A.16}$$

otherwise, SNR becomes

$$SNR = \frac{mean(M)}{std(M)} \tag{A.17}$$

where M is the collection of all the datapoints M_i, and $mean(M)$ the mean value of M, and $std(M)$ the standard deviation.

Bibliography

[Alexander et al., 2007] Alexander, A. L., Lee, J. E., Lazar, M., and Field, A. S. (2007). Diffusion tensor imaging of the brain. *Neurotherapeutics*, 4(3):316–329.

[Alexander, 2008] Alexander, D. C. (2008). A general framework for experiment design in diffusion MRI and its application in measuring direct tissue-microstructure features. *Magnetic Resonance in Medicine*, 60(2):439–448.

[Alexander et al., 2010] Alexander, D. C., Hubbard, P., Hall, M., Moore, E., Ptito, M., Parker, G., and Dyrby, T. (2010). Orientationally invariant indices of axon diameter and density from diffusion MRI. *NeuroImage*, 52(4):1374–1389.

[Amelink et al., 2003] Amelink, A., Bard, M. P., Burgers, S. A., and Sterenborg, H. J. (2003). Single-scattering spectroscopy for the endoscopic analysis of particle size in superficial layers of turbid media. *Applied optics*, 42(19):4095–4101.

[Amelink et al., 2004] Amelink, A., Sterenborg, H. J., Bard, M. P., and Burgers, S. A. (2004). In vivo measurement of the local optical properties of tissue by use of differential path-length spectroscopy. *Optics letters*, 29(10):1087–1089.

[Arifler et al., 2003] Arifler, D., Guillaud, M., Carraro, A., Malpica, A., Follen, M., and Richards-Kortum, R. R. (2003). Light scattering from normal and dysplastic cervical cells at different epithelial depths: finite-difference time-

domain modeling with a perfectly matched layer boundary condition. *Journal of biomedical optics*, 8(3):484–494.

[Arridge, 1995a] Arridge, S. (1995a). Photon-measurement density functions. Part I: Analytical forms. *Applied Optics*, 34(31):7395–7409.

[Arridge, 1995b] Arridge, S. R. (1995b). Photon-measurement density functions. Part II: Finite-element-method calculations. *Applied Optics*, 34(34):8026–8037.

[Assaf and Basser, 2005] Assaf, Y. and Basser, P. J. (2005). Composite hindered and restricted model of diffusion (CHARMED) MR imaging of the human brain. *NeuroImage*, 27(1):48–58.

[Assaf et al., 2008] Assaf, Y., Blumenfeld-Katzir, T., Yovel, Y., and Basser, P. J. (2008). AxCaliber: a method for measuring axon diameter distribution from diffusion MRI. *Magnetic Resonance in Medicine*, 59(6):1347–1354.

[Assaf and Pasternak, 2008] Assaf, Y. and Pasternak, O. (2008). Diffusion Tensor Imaging (DTI)-based White Matter Mapping in Brain Research: A Review. *Journal of Molecular Neuroscience*, 34(1):51–61.

[Augusteyn et al., 2008] Augusteyn, R. C., Vrensen, G., and Willekens, B. (2008). The effect of paraformaldehyde fixation and pbs storage on the water content of the human lens. *Molecular vision*, 14:90.

[Baba et al., 2002] Baba, J. S., Chung, J.-R., DeLaughter, A. H., Cameron, B. D., and Cote, G. L. (2002). Development and calibration of an automated mueller matrix polarization imaging system. *Journal of biomedical optics*, 7(3):341–349.

[Backman et al., 1999] Backman, V., Gurjar, R., Badizadegan, K., Itzkan, I., Dasari, R., Perelman, L., and Feld, M. (1999). Polarized light scattering spectroscopy for quantitative measurement of epothelial cellular structures in situ. *Journal of Selected Topics in Quantum Electronics*, 5(4):1019–1026.

[Basser et al., 2000] Basser, P. J., Pajevic, S., Pierpaoli, C., Duda, J., and Aldroubi, A. (2000). In vivo fiber tractography using DT-MRI data. *Magnetic resonance in medicine*, 44(4):625–632.

[Basser and Pierpaoli, 1996] Basser, P. J. and Pierpaoli, C. (1996). Microstructural and physiological features of tissues elucidated by quantitative-diffusion-tensor MRI. *Journal of Magnetic Resonance, Series B*, 111(3):209–219.

[Behrens et al., 2003] Behrens, T., Woolrich, M., Jenkinson, M., and Johansen, H. (2003). Characterization and propagation of uncertainty in diffusion-weighted MR imaging. *Magnetic Resonance in Medicine*, (50):1077–1088.

[Berrocal et al., 2007] Berrocal, E., Sedarsky, D., Paciaroni, M., Meglinski, I., and Linne, M. (2007). Laser light scattering in turbid media Part I: Experimental and simulated results for the spatial intensity distribution. *Optic Express*, 15(17):10649–10665.

[Beuthan et al., 1996] Beuthan, J., Minet, O., Helfmann, J., Herrig, M., and Müller, G. (1996). The spatial variation of the refractive index in biological cells. *Physics in medicine and biology*, 41(3):369.

[Bihan, 1995] Bihan, D. L. (1995). Molecular diffusion, tissue microdynamics and microstructure. *NMR in Biomedicine*, 8(7):375–386.

[Blonk and van Aalsh, 1993] Blonk, J. and van Aalsh, H. (1993). Confocal scanning light microscopy in food research. *Food Research International*, (26):297–311.

[Bloom and Richardson, 1957] Bloom, H. and Richardson, W. (1957). Histological grading and prognosis in breast cancer: a study of 1409 cases of which 359 have been followed for 15 years. *British Journal of Cancer*, 11(3):359.

[Bohren and Huffman, 2008] Bohren, C. F. and Huffman, D. R. (2008). *Absorption and scattering of light by small particles*. Wiley. com.

[Bower et al., 1999] Bower, C., Gallegos, C., Mackley, M., and Madiedo, J. (1999). The rheological and microstructural characterisation of the non-linear fow behaviour of concentrated oil-in-water emulsions. *Rheol Acta*, (38):145–159.

[Brunsting and Mullaney, 1974] Brunsting, A. and Mullaney, P. F. (1974). Differential light scattering from spherical mammalian cells. *Biophysical journal*, 14(6):439.

[Callaghan et al., 2003] Callaghan, P., Godefroy, S., and Ryland, B. (2003). Use of the second dimension in PGSE NMR studies of porous media. *Magnetic resonance imaging*, 21(3):243–248.

[Callaghan and Xia, 1991] Callaghan, P. and Xia, Y. (1991). Velocity and Diffusion Imaging in Dynamic NMR Microscopy. *Journal of Magnetic Resonance*, (2):326–352.

[Callaghan, 1997] Callaghan, P. T. (1997). A simple matrix formalism for spin echo analysis of restricted diffusion under generalized gradient waveforms. *Journal of Magnetic Resonance*, 129(1):74–84.

[Callaghan and Jolley, 1983] Callaghan, P. T. and Jolley, K. W. (1983). Diffusion of Fat and Water in Cheese As Studied by Pulsed Field Gradient Nuclear Magnetic Resonance. *Journalof Colloidand Interface Science*, 93(12):521–529.

[Carr and Purcell, 1954] Carr, H. and Purcell, E. (1954). Effects of Diffusion on Free Precession in Nuclear Magnetic Resonance Experiments. *Phys. Rev.*, 94:630–638.

[Chalut et al., 2008] Chalut, K. J., Giacomelli, M. G., and Wax, A. (2008). Application of mie theory to assess structure of spheroidal scattering in backscattering geometries. *JOSA A*, 25(8):1866–1874.

[Chantrapornchai et al., 1999] Chantrapornchai, W., Clydesdale, F., and McClements, D. (1999). Influence of droplet characteristics on the optical prop-

erties of colored oil-in-water emulsions. *Colloids and Surfaces A: Physicochemical and Engineering Aspects*, (155):373–382.

[Chapman and Cowling, 1970] Chapman, S. and Cowling, T. G. (1970). *The mathematical theory of non-uniform gases: an account of the kinetic theory of viscosity, thermal conduction and diffusion in gases*. Cambridge university press.

[Chu and Churchill, 1955] Chu, C.-M. and Churchill, S. (1955). Representation of the angular distribution of radiation scattered by a spherical particle. *Journal of the Optical Society of America*, 45(11):958–962.

[Colvin et al., 2011] Colvin, D. C., Loveless, M. E., Does, M. D., Yue, Z., Yankeelov, T. E., and Gore, J. C. (2011). Earlier detection of tumor treatment response using magnetic resonance diffusion imaging with oscillating gradients. *Magnetic resonance imaging*, 29(3):315–323.

[Contini et al., 1997] Contini, D., Martelli, F., and Zaccanti, G. (1997). Photon migration through a turbid slab described by a model based on diffusion approximation. i. theory. *Applied optics*, 36(19):4587–4599.

[Cook et al., 2006] Cook, P. A., Bai, Y., Nedjati-Gilani, S., Seunarine, K. K., Hall, M. G., Parker, G. J., and Alexander, D. C. (2006). Camino: Open-Source Diffusion-MRI Reconstruction and Processing. *14th Scientific Meeting of the International Society for Magnetic Resonance in Medicine*.

[Cornette and Shanks, 1992] Cornette, W. and Shanks, J. (1992). Physically reasonable analytic expression for the single-scattering phase function. *Applied Optics*, 31(16):3152–3160.

[Dahm and Dahm, 2001] Dahm, D. J. and Dahm, K. D. (2001). The physics of near-infrared scattering. *Near-Infrared Technology in the Agricultural and Food Industries*, 2.

[Damadian, 1971] Damadian, R. (1971). Tumor Detection by Nuclear Magnetic Resonance. *Science*, (171):1151–1153.

[Denkova et al., 2004] Denkova, P., Tcholakova, S., Denkov, N., Danov, K., Campbell, B., Shawl, C., and Kim, D. (2004). Evaluation of the Precision of Drop-Size Determination in Oil/Water Emulsions bi Low-Resolution NMR Spectroscopy. *American Chemical Society*, (20):11402–11413.

[Di Ninni et al., 2011] Di Ninni, P., Martelli, F., and Zaccanti, G. (2011). Intralipid: towards a diffusive reference standard for optical tissue phantoms. *Physics in medicine and biology*, 56(2):N21.

[Diko et al., 1995] Diko, P., Pelerin, N., and Odier, P. (1995). Microstructure analysis of melt-textured yba 2 cu 3 o 7- x ceramics by polarized light microscopy. *Physica C: Superconductivity*, 247(1):169–182.

[Ding et al., 2005] Ding, H., Lu, J. Q., Jacobs, K. M., and Hu, X.-H. (2005). Determination of refractive indices of porcine skin tissues and intralipid at eight wavelengths between 325 and 1557 nm. *JOSA A*, 22(6):1151–1157.

[Does et al., 2003] Does, M. D., Parsons, E. C., and Gore, J. C. (2003). Oscillating gradient measurements of water diffusion in normal and globally ischemic rat brain. *Magnetic Resonance in Medicine*, 49(2):206–215.

[Douek et al., 1991] Douek, P., Turner, R., Pekar, J., Patronas, N., and Le Bihan, D. (1991). MR color mapping of myelin fiber orientation. *Journal of computer assisted tomography*, 15(6):923–929.

[Douglass and McCall, 1958] Douglass, D. C. and McCall, D. W. (1958). Diffusion in paraffin hydrocarbons. *The Journal of Physical Chemistry*, 62(9):1102–1107.

[Drezek et al., 1999] Drezek, R., Dunn, A., and Richards-Kortum, R. (1999). Light scattering from cells: finite-difference time-domain simulations and goniometric measurements. *Applied Optics*, 38(16):3651–3661.

[Drobnjak and Alexander, 2011] Drobnjak, I. and Alexander, D. C. (2011). Optimising time-varying gradient orientation for microstructure sensitivity in diffusion-weighted mr. *Journal of Magnetic Resonance*, 212(2):344–354.

[Edge and Compton, 2010] Edge, S. B. and Compton, C. C. (2010). The american joint committee on cancer: the 7th edition of the ajcc cancer staging manual and the future of tnm. *Annals of surgical oncology*, 17(6):1471–1474.

[Enfield and Gibson, 2012] Enfield, L. and Gibson, A. (2012). A review of mechanisms of contrast for diffuse optical imaging of cancer. *Journal of Near Infrared Spectroscopy*, 1(20):185–202.

[Everett and Auty, 2008] Everett, D. W. and Auty, M. A. (2008). Cheese structure and current methods of analysis. *International Dairy Journal*, (18):759–773.

[Fang and Boas, 2009] Fang, Q. and Boas, D. A. (2009). Monte carlo simulation of photon migration in 3d turbid media accelerated by graphics processing units. *Optics express*, 17(22):20178–20190.

[Fantini et al., 1994] Fantini, S., Franceschini, M. A., and Gratton, E. (1994). Semi-infinite-geometry boundary problem for light migration in highly scattering media: a frequency-domain study in the diffusion approximation. *JOSA B*, 11(10):2128–2138.

[Fass, 2008] Fass, L. (2008). Imaging and cancer: A review. *Molecular oncology*, (2):115–152.

[Faye, 2008] Faye, J. (2008). Copenhagen interpretation of quantum mechanics. *Stanford Encyclopedia of Philosophy*.

[Feng et al., 2013] Feng, X., Sun, L., and Zhang, E. (2013). Depth selectivity for the assessment of microstructure by polarization studies. *Biomedical optics express*, 4(6):958.

[Filler, 2009] Filler, A. G. (2009). The history, development and impact of computed imaging in neurological diagnosis and neurosurgery: Ct, mri, and dti. *Nature Precedings*, 7(1):1–69.

[Fishkin and Gratton, 1993] Fishkin, J. B. and Gratton, E. (1993). Propagation of photon-density waves in strongly scattering media containing an ab-

sorbing semi-infinite plane bounded by a straight edge. *JOSA A*, 10(1):127–140.

[Flock et al., 1992] Flock, S. T., Jacques, S. L., Wilson, B. C., Star, W. M., and van Gemert, M. J. (1992). Optical properties of intralipid: a phantom medium for light propagation studies. *Lasers in Surgery and Medicine*, 12(5):510–519.

[Ford, 1992] Ford, B. J. (1992). From dilettante to diligent experimenter, a reappraisal of leeuwenhoek as microscopist and investigator. *Biology History*, 5(3).

[Fox et al., 1985] Fox, C. H., Johnson, F. B., Whiting, J., and Roller, P. P. (1985). Formaldehyde fixation. *J Histochem Cytochem*, 33(8):845–853.

[Frangioni, 2008] Frangioni, J. V. (2008). New technologies for human cancer imaging. *Journal of clinical oncology*, 26(24):4012–4021.

[Fukamachi and Kim, 1989] Fukamachi, H. and Kim, Y. S. (1989). Glandular structure formation of ls174t human colon cancer cells cultured with collagen gels. *Development, growth & differentiation*, 31(2):107–112.

[Gao and Zhao, 2010] Gao, H. and Zhao, H. (2010). Multilevel bioluminescence tomography based on radiative transfer equation Part 1: l1 regularization. *Optics Express*, (18):1854–1871.

[Gibson and Dehghani, 2009] Gibson, A. and Dehghani, H. (2009). Diffuse optical imaging. *Philosophical Transcripts of Royal Society*, (367):3055–3072.

[Gibson et al., 2005] Gibson, A. P., Hebden, J. C., and Arridge, S. R. (2005). Recent advances in diffuse optical imaging. *Physics in Medicine and Biology*, (50):1–43.

[Graaff et al., 1992] Graaff, R., Aarnoudse, J., Zijp, J. R., Sloot, P., De Mul, F., Greve, J., and Koelink, M. (1992). Reduced light-scattering properties for mixtures of spherical particles: a simple approximation derived from Mie calculations. *Applied optics*, 31(10):1370–1376.

[Gurjar et al., 2001] Gurjar, R., Backman, V., Perelman, L., Georgakoudi, I., Badizadegan, K., Itzkan, I., Dasari, R., and Feld, M. (2001). Imaging human epithelial properties with polarized light–scattering spectroscopy. *Nature Medicine*, 7(11):1245–1248.

[Haacke et al., 1999] Haacke, E. M., Brown, R. W., Thompson, M. R., and Venkatesan, R. (1999). Magnetic resonance imaging. *Physical principles and sequence design*.

[Haario et al., 2006] Haario, H., Laine, M., Mira, A., and Saksman, E. (2006). DRAM: Efficient adaptive MCMC. *Stat. Comput.*, (16):339–354.

[Hall and Alexander, 2009] Hall, M. and Alexander, D. (2009). Convergence and Parameter Choice for Monte-Carlo Simulations of Diffusion MRI. *Medical Imaging, IEEE Transactions*, 28(9):1354–1364.

[Hebden et al., 2012] Hebden, J. C., Varela, M., Magazov, S., Everdell, N., Gibson, A., Meek, J., and Austin, T. (2012). Diffuse optical imaging of the newborn infant brain. In *Biomedical Imaging (ISBI), 2012 9th IEEE International Symposium on*, pages 503–505. IEEE.

[Henkelman et al., 1994] Henkelman, R. M., Stanisz, G. J., Kim, J. K., and Bronskill, M. J. (1994). Anisotropy of nmr properties of tissues. *Magnetic resonance in medicine*, 32(5):592–601.

[Henyey and Greenstein, 1940] Henyey, L. and Greenstein, J. (1940). Diffuse radiation in the galaxy. *Annales d'Astrophysique*, pages 117–137.

[Hill, 2003] Hill, S. C. (2003). Method for integrating the absorption cross sections of spheres over wavelength or diameter. *Applied optics*, 42(21):4381–4388.

[Hollingsworth and Johns, 2003a] Hollingsworth, K. and Johns, M. (2003a). Measurement of emulsion droplet sizes using pfg nmr and regularization methods. *Journal of colloid and interface science*, 258(2):383–389.

[Hollingsworth and Johns, 2003b] Hollingsworth, K. and Johns, M. (2003b). Measurement of emulsion droplets sizes using PFG NMR and regularization methods. *Journal of Colloid and Interface Science*, (258):383–389.

[Hollingsworth et al., 2004] Hollingsworth, K., Sederman, A., C.Buckley, Gladden, L., and Johns, M. (2004). Fast emulsion droplet sizing using NMR self-diffusion measurements. *Journal of Colloid and Interface Science*, (274):244–250.

[Hulst and Van De Hulst, 1957] Hulst, H. C. and Van De Hulst, H. (1957). *Light scattering by small particles*. Courier Dover Publications.

[Hunter et al., 2006] Hunter, M., Backman, V., Popescu, G., Kalashnikov, M., Boone, C. W., Wax, A., Gopal, V., Badizadegan, K., Stoner, G. D., and Feld, M. S. (2006). Tissue self-affinity and polarized light scattering in the born approximation: a new model for precancer detection. *Physical review letters*, 97(13):138102.

[Huppert et al., 2008] Huppert, T., Diamond, S., and Boas, D. (2008). Direct estimation of evoked hemoglobin changes by multimodality fusion imaging. *Journal of Biomedical Optics*, 13(5).

[Ianuş et al., 2013] Ianuş, A., Siow, B., Drobnjak, I., Zhang, H., and Alexander, D. C. (2013). Gaussian phase distribution approximations for oscillating gradient spin echo diffusion mri. *Journal of Magnetic Resonance*, 227:25–34.

[Ingle and Crouch, 1988] Ingle, J. D. and Crouch, S. R. (1988). Spectrochemical analysis. *Englewood Cliffs, NJ*, page 106.

[Irvine, 1965] Irvine, W. (1965). Multiple scattering by large particles. *The Astrophysical Journal*, pages 1563–1574.

[Ishimaru, 1978] Ishimaru, A. (1978). *Wave Propagation and Scattering in Random Media*, volume 1. Academic Press, Inc.

[Itzkan et al., 2007] Itzkan, I., Qiu, L., Fang, H., Zamann, M., Hanlon, E., and Perelman, L. (2007). Cofocal light absorption and scattering spectroscopic

microscopy monitors organelles in live cells with no exogenous labels. *PNAS*, 104(44):17255–17260.

[Jacques, 2013] Jacques, S. L. (2013). Optical properties of biological tissues: a review. *Physics in medicine and biology*, 58(11):R37.

[Jass et al., 1986] Jass, J., Atkin, W., Cuzick, J., Bussey, H., Morson, B., Northover, J., and Todd, I. (1986). The grading of rectal cancer: historical perspectives and a multivariate analysis of 447 cases. *Histopathology*, 10(5):437–459.

[Jennions et al., 2006] Jennions, D., Gibson, A., Everdell, N., Hebden, J., and Becker, W. (2006). Fast time-resolved optical tomography for 3D neonatal functional imaging. *Biomed Opt Technical Digest*, (SH45).

[Jensen et al., 2011] Jensen, J. H., Falangola, M. F., Hu, C., Tabesh, A., Rapalino, O., Lo, C., and Helpern, J. A. (2011). Preliminary observations of increased diffusional kurtosis in human brain following recent cerebral infarction. *NMR in Biomedicine*, 24(5):452–457.

[Jensen et al., 2005] Jensen, J. H., Helpern, J. A., Ramani, A., Lu, H., and Kaczynski, K. (2005). Diffusional kurtosis imaging: The quantification of non-gaussian water diffusion by means of magnetic resonance imaging. *Magnetic Resonance in Medicine*, 53(6):1432–1440.

[Johansen-Berg and Behrens, 2009] Johansen-Berg, H. and Behrens, T. E. (2009). *Diffusion MRI: From quantitative measurement to in-vivo neuroanatomy*. Academic Press.

[Johns, 2009] Johns, M. (2009). NMR studies of emulsions. *Current Opinion in Colloid and Interface Science*, (14):178–183.

[Johns et al., 2005] Johns, M., Giller, C., German, D., and Liu, H. (2005). Determination of reduced scattering coefficient of biological tissue from a needle-like probe. *Optics express*, 13(13):4828–4842.

[Johnson and Wichern, 2002] Johnson, R. A. and Wichern, D. W. (2002). *Applied multivariate statistical analysis*, volume 5. Prentice hall Upper Saddle River, NJ.

[Jones, 2011] Jones, D. (2011). *Diffusion MRI. Theory, Methods, and Applications*, volume 1. Oxford University Press.

[Jones et al., 2013] Jones, D. K., Knösche, T. R., and Turner, R. (2013). White matter integrity, fiber count, and other fallacies: the do's and don'ts of diffusion mri. *Neuroimage*, 73:239–254.

[Junqueira et al., 1977] Junqueira, L. C. U., Carneiro, J., and Contopoulos, A. N. (1977). Basic histology.

[Kaiser et al., 1997] Kaiser, K., Guggenberger, G., Haumaier, L., and Zech, W. (1997). Dissolved organic matter sorption on subsoils and minerals studied by 13C-NMR and DRIFT spectroscopy. *European Journal of Soil Science*, (48):301–310.

[Kaplan et al., 1994] Kaplan, P., Dinsmore, A., and Yodh, A. (1994). Diffuse–transmission spectroscopy: A structural probe of opaque colloidal mixtures. *Physical Review E*, 50(6):4827–4836.

[Khan et al., 2003] Khan, M., Walsh, P., Miller, M., Bales, W., Epstein, J., Mangold, L., Partin, A., and Veltri, R. (2003). Quantitative alterations in nuclear structure predict prostate carcinoma distant metastasis and death in men with biochemical recurrence after radical prostatectomy. *Cancer*, 12(98):2583–91.

[Khuri, 2004] Khuri, A. I. (2004). Applications of Dirac's delta function in statistics. *International Journal of Mathematical Education in Science and Technology*, 35(2):185–195.

[Kiyotoki et al., 2013] Kiyotoki, S., Nishikawa, J., Okamoto, T., Hamabe, K., Saito, M., Goto, A., Fujita, Y., Hamamoto, Y., Takeuchi, Y., Satori, S., et al. (2013). New method for detection of gastric cancer by hyperspectral imaging: a pilot study. *Journal of biomedical optics*, 18(2):026010–026010.

[Koh and Collins, 2007] Koh, D. and Collins, D. (2007). Diffusion-Weighted MRI in the Body: Applications and Challenges in Oncology. *American Journal of Roentanology*, 188(6):1622–1635.

[Kramer et al., 2010] Kramer, C., Sinusas, A., Sosnovik, D., French, B., and Bengel, F. (2010). Multimodality imaging of myocardial injury and remodeling. *The Journal of Nuclear Medicine*, 51(5):108–560.

[Kruse et al., 2000] Kruse, S. A., Smith, J. A., and et al. (2000). Tissue characterization using magnetic resonance elastography: preliminary results. *Phys. Med. Biol.*, (45):1579–1590.

[Kurhanewicz et al., 2002] Kurhanewicz, J., Swanson, M., Nelson, S., and Vigneron, D. (2002). Combined Magnetic Resonance Imaging and Spectroscopic Imaging Approach to Molecular Imaging of Prostate Cancer. *Journal of Magnetic Resonance Imaging*, (16):451–463.

[Kurjak, 2000] Kurjak, A. (2000). Ultrasound scanning – Prof. Ian Donald (1910–1987). *European Journal of Obstetrics and Gynecology and Reproductive Biology*, (90):187–189.

[Laufer et al., 2012] Laufer, J., Johnson, P., Zhang, E., Treeby, B., Cox, B., Pedley, B., and Beard, P. (2012). In vivo preclinical photoacoustic imaging of tumor vasculature development and therapy. *Journal of biomedical optics*, 17(5):0560161–0560168.

[Lauterbur, 1973] Lauterbur, P. (1973). Image Formation by Induced Local Interactions: Examples of Employing Nuclear Magnetic Resonance. *Nature*, (242):190–191.

[Le Bihan et al., 1985] Le Bihan, D., Breton, E., et al. (1985). Imagerie de diffusion in-vivo par résonance magnétique nucléaire. *Comptes-Rendus de l'Académie des Sciences*, 93(5):27–34.

[Lee et al., 1997] Lee, S. J., Jeon, I. J., and Harberns, L. H. (1997). Near-Infrared Reflectance Spectroscopy for Rapid Analysis of Curds during Cheddar Cheese Making. *Journal of Food Science*, 62(1):53–56.

[Leunig et al., 1992] Leunig, M., Yuan, F., Menger, M. D., Boucher, Y., Goetz, A. E., Messmer, K., and Jain, R. K. (1992). Angiogenesis, microvascular architecture, microhemodynamics, and interstitial fluid pressure during early growth of human adenocarcinoma ls174t in scid mice. *Cancer Research*, 52(23):6553–6560.

[Lie et al., 2008] Lie, X., Ranasinghesagara, J. C., and Yao, G. (2008). Polarization-sensitive reflectance imaging in skeletal muscle. *Optics Express*, 16(13):9927–9935.

[Lin et al., 1997] Lin, S.-P., Wang, L., Jacques, S. L., and Tittel, F. K. (1997). Measurement of tissue optical properties by the use of oblique-incidence optical fiber reflectometry. *Applied optics*, 36(1):136–143.

[Lucchinetti et al., 2000] Lucchinetti, C., Bruck, W., Parisi, J., Scheithauer, B., Rodriguez, M., Lassman, H., et al. (2000). Heterogeneity of multiple sclerosis lesions: implications for the pathogenesis of demyelination. *Annals of neurology*, 47(6):707–717.

[MacKintosh et al., 1989] MacKintosh, F., Zhu, J., Pine, D., and Weitz, D. (1989). Polarization memory of multiply scattered light. *Physical Review B*, 40(13):9342.

[Mahdjoub et al., 2003] Mahdjoub, R., Molegnana, J., Seurin, M.-J., and Briguet, A. (2003). High Resolution Magnetic Resonance Imaging Evaluation of Cheese. *Journal of Food Science*, 68(6):1982–1984.

[Maier et al., 1994] Maier, J. S., Walker, S. A., Fantini, S., Franceschini, M. A., and Gratton, E. (1994). Possible correlation between blood glucose concentration and the reduced scattering coefficient of tissues in the near infrared. *Optics letters*, 19(24):2062–2064.

[Mali et al., 2002] Mali, S., Grossmann, M. V. E., Garcia, M. A., Martino, M. N., and Zaritzky, N. E. (2002). Microstructural characterization of yam starch films. *Carbohydrate Polymers*, 50(4):379–386.

[Martelli et al., 1997] Martelli, F., Contini, D., Taddeucci, A., and Zaccanti, G. (1997). Photon migration through a turbid slab described by a model based on diffusion approximation. ii. comparison with monte carlo results. *Applied optics*, 36(19):4600–4612.

[Matcher et al., 1999] Matcher, S., Cope, M., and Delpy, D. (1999). Use of the water absorption spectrum to quantify tissue chromophore concentration changes in near-infrared spectroscopy. *Physics in Medicine and Biology*, 39(177):177–196.

[McRobbie et al., 2006] McRobbie, D. W., Moore, E. A., Graves, M. J., and Prince, M. R. (2006). *MRI from Picture to Proton*. Cambridge University Press.

[Michels et al., 2008] Michels, R., Foschum, F., and Kienle, A. (2008). Optical properties of fat emulsions. *Optics Express*, 16(8):5907–5925.

[Michette, 2003] Michette, A. (2003). X-ray optics. *The Optics Encyclopedia*.

[Mie, 1908] Mie, G. (1908). Beiträge zur Optik trüber Medien, speziell kolloidaler Metallösungen. *Annalen der physik*, 330(3):377–445.

[Miller, 1924] Miller, C. C. (1924). The stokes-einstein law for diffusion in solution. *Proceedings of the Royal Society of London. Series A*, 106(740):724–749.

[Moseley et al., 1990] Moseley, M., Cohen, Y., Mintorovitch, J., Chileuitt, L., Shimizu, H., Kucharczyk, J., Wendland, M., and Weinstein, P. (1990). Early detection of regional cerebral ischemia in cats: comparison of diffusion- and t2-weighted mri and spectroscopy. *Magnetic Resonance in Medicine*, 14(2):330–346.

[Mourant et al., 2000] Mourant, J. R., Canpolat, M., Brocker, C., Espondo-Ramos, O., Johnson, T. M., Matanock, A., Stetter, K., and Freyer, J. P. (2000). Light scattering from cells: the contribution of the nucleus and the effects of proliferative status. In *BiOS 2000 The International Symposium*

on Biomedical Optics, pages 33–42. International Society for Optics and Photonics.

[Mourant et al., 1998] Mourant, J. R., Freyer, J. P., Hielscher, A. H., Eick, A. A., Shen, D., and Johnson, T. M. (1998). Mechanisms of light scattering from biological cells relevant to noninvasive optical-tissue diagnostics. *Applied optics*, 37(16):3586–3593.

[Mulvey, 1962] Mulvey, T. (1962). Origins and historical development of the electron microscope. *Brit. J. Appl. Phys*, 13.

[Murday and Cotts, 1968] Murday, J. and Cotts, R. (1968). Self-diffusion coefficient of liquid lithium. *The Journal of Chemical Physics*, 48(11):4938–4945.

[Nachabé et al., 2010] Nachabé, R., Sterenborg, H. J., Hendriks, B. H., Desjardins, A. E., van der Voort, M., and van der Mark, M. B. (2010). Estimation of lipid and water concentrations in scattering media with diffuse optical spectroscopy from 900to1600nm. *Journal of biomedical optics*, 15(3):037015–037015.

[Neuman, 1974] Neuman, C. (1974). Spin echo of spins diffusing in a bounded medium. *The Journal of Chemical Physics*, 60(11):4508–4511.

[Neumann-Haefelin et al., 1999] Neumann-Haefelin, T., Wittsack, H.-J., Wenserski, F., Siebler, M., Seitz, R., Modder, U., and Freund, H.-J. (1999). Diffusion- and perfusion-weighted mri. the dwi/pwi mismatch region in acute stroke. *Neuroimage*, 30(8):1591–1597.

[Ntziachristos et al., 2000] Ntziachristos, V., Yodh, A., Schnall, M., and Chance, B. (2000). Concurrent MRI and diffuse optical tomography of breast after indocyanine green enhancement. *Nature*, 97(6):2767–2772.

[Orchard, 2011] Orchard, G. (2011). Histopathology (fundamentals of biomedical science) author: Guy orchard, brian nation, publisher: Oxford university press.

[Panagiotaki et al., 2015] Panagiotaki, E., Chan, R. W., Dikaios, N., Ahmed, H. U., O'Callaghan, J., Freeman, A., Atkinson, D., Punwani, S., Hawkes, D. J., and Alexander, D. C. (2015). Microstructural characterization of normal and malignant human prostate tissue with vascular, extracellular, and restricted diffusion for cytometry in tumours magnetic resonance imaging. *Investigative radiology*, 50(4):218–227.

[Panagiotaki et al., 2009] Panagiotaki, E., Fonteijn, H., Siow, B., Hall, M. G., Price, A., Lythgoe, M. F., and Alexander, D. C. (2009). Two-compartment models of the di usion MR signal in brain white matter. *Medical Image Computing and Computer Assisted Intervention (MICCAI)*, 1:329–336.

[Panagiotaki et al., 2012] Panagiotaki, E., Schneider, T., Siow, B., Hall, M., Lythgoe, M., and Alexander, D. (2012). Compartment models of the diffusion MR signal in brain white matter: A taxonomy and comparison. *NeuroImage*, (59):2241–2254.

[Panagiotaki et al., 2014] Panagiotaki, E., Walker-Samuel, S., Siow, B. M., Johnson, P., Rajkumarc, V., Pedley, R. B., Lythgoe, M. F., and Alexander, D. C. (2014). Non-invasive quantification of solid tumor microstructure using verdict mri. *Cancer research*, pages canres–2511.

[Papoulis and Pillai, 2002] Papoulis, A. and Pillai, S. U. (2002). *Probability, random variables, and stochastic processes*. Tata McGraw-Hill Education.

[Park et al., 2001] Park, B. H., Saxer, C., Srinivas, S. M., Nelson, J. S., and de Boer, J. F. (2001). In vivo burn depth determination by high-speed fiber-based polarization sensitive optical coherence tomography. *Journal of Biomedical Optics*, 6(4):474–479.

[Patterson et al., 1989] Patterson, M., Chance, B., and Wilson, B. (1989). A 32-channel time-resolved instrument for medical optical tomography. *Applied Optics*, 28(12):2331–2336.

[Pawley, 2010] Pawley, J. (2010). *Handbook of biological confocal microscopy*. Springer.

[Perelman et al., 1998] Perelman, L., Backman, V., Wallace, M., Zonis, G., Monoharan, R., Nusrat, A., Shields, S., Lima, C., Hamano, T., Itzkan, I., Dam, J. V., Crawford, J., and Feld, M. (1998). Observation of periodic fine structure in reflactance from biological tissue: a new technique for measuring nuclear size distribution. *Physical Review Letters*, 80(3):627–630.

[Pickering, 1992] Pickering, J. (1992). Optical property changes as a result of protein denature in albumen and yolk. *J. Photochem. Photobiol. B: Biol.*, (16):101–111.

[Pillonel et al., 2003] Pillonel, L., Luginbühl, W., Picque, D., Schaller, E., Tabacchi, R., and Bosset, J. (2003). Analytical methods for the determination of the geographic origin of Emmental cheese: mid- and near-infrared spectroscopy. *Eur Food Res Technol*, (216):174–178.

[Pogue et al., 2004] Pogue, B., Jiang, S., Dehghani, H., Kogel, C., Soho, S., Srinivasan, S., Song, X., Tosteson, T., Poplack, S., and Paulsen, K. (2004). Characterization of hemoglobin, water, and NIR scattering in breast tissue: analysis of intersubject variability and menstrual cycle changes. *Journal of Biomedical Optics*, 9(3):541–552.

[Prahl et al., 1989] Prahl, S., Keijzer, M., Jaques, S., and Welch, A. (1989). A Monte Carlo Model of Light Propagation in Tissue. *Dosimetry of Laser Radiation in Medicine and Biology*, IS 5:112–111.

[Proverbio et al., 2014a] Proverbio, A., Siow, B., Alexander, D., Hebden, J. C., and Gibson, A. (2014a). Combined diffuse scatter spectroscopy and diffusion nmr for quantitative characterization of microstructure. In *Biomedical Optics*, pages BT3A–40. Optical Society of America.

[Proverbio et al., 2014b] Proverbio, A., Siow, B. M., Lythgoe, M. F., Alexander, D. C., and Gibson, A. P. (2014b). Multimodality characterization of microstructure by the combination of diffusion nmr and time-domain diffuse optical data. *Physics in medicine and biology*, 59(11):2639.

[Pu et al., 2012] Pu, Y., Wang, W., Mohammad, A.-R., Gayen, S. K., and Xuc, M. (2012). Determination of optical coefficients and fractal dimensional parameters of cancerous and normal prostate tissues.

[Rabi et al., 1991] Rabi, I., Zacharias, J., Millman, S., and Kusch, P. (1991). Milestones in magnetic resonance:'a new method of measuring nuclear magnetic moment'. 1938. *Journal of magnetic resonance imaging: JMRI*, 2(2):131–133.

[Ramachandran et al., 2007] Ramachandran, J., Powers, T., Carpenter, S., Garcia-Lopez, A., Freyer, J., and J.R.Mourant (2007). Light scattering and microarchitectural differences between tumorigenic and non-tumorigenic cell models of tissue. *Optic Express*, 15(7):4039–4053.

[Ramella-Roman et al., 2007a] Ramella-Roman, J., Prahl, S., and Jaques, S. (2007a). Three Monte Carlo programs of polarized light transport into scattering media: part I. *Optics Express*, 13(12):4420–4438.

[Ramella-Roman et al., 2007b] Ramella-Roman, J., Prahl, S., and Jaques, S. (2007b). Three Monte Carlo programs of polarized light transport into scattering media: part II. *Optics Express*, 13(25):10392–10405.

[Rayleigh, 1899] Rayleigh, L. (1899). XXXIV. On the transmission of light through an atmosphere containing small particles in suspension, and on the origin of the blue of the sky. *The London, Edinburgh, and Dublin Philosophical Magazine and Journal of Science*, 47(287):375–384.

[Rehn et al., 2013] Rehn, S., Planat-Chrétien, A., Berger, M., Dinten, J.-M., Deumié, C., and Da Silva, A. (2013). Depth probing of diffuse tissues controlled with elliptically polarized light. *Journal of biomedical optics*, 18(1):016007–016007.

[Richman and Bodmer, 1988] Richman, P. I. and Bodmer, W. F. (1988). Control of differentiation in human colorectal carcinoma cell lines: epithelial—mesenchymal interactions. *The Journal of pathology*, 156(3):197–211.

[Rose et al., 2000] Rose, S., Chen, F., Chalk, J., Zelaya, Strugnell, W., Benson, M., Semple, J., and Doddrell, D. (2000). Loss of connectivity in Alzheimer's disease: an evaluation of white matter tract integrity with color coded MR diffusion tensor imaging. *J. Neurol. Neurosurg. Psychiat.*, (69):528–530.

[Rosenberg et al., 1992] Rosenberg, M., McCarthy, M., and Kauten, R. (1992). Evaluation of Eye Formation and Structural Quality of Swiss–Type Cheese by Magnetic Resonance Imaging. *Journal Dairy Science*, (75):2083–2091.

[Rosencwaig and Gersho, 1976] Rosencwaig, A. and Gersho, A. (1976). Theory of the photoacoustic effect with solids. *Journal of Applied Physics*, 47(1):64–69.

[Rotenberg et al., 1991] Rotenberg, M., Rubin, M., Bor, A., Meyuhas, D., Talmon, Y., and Lichtenberg, D. (1991). Physico-chemical characterization of intralipid emulsions. *Biochimica et Biophysica Acta (BBA)-Lipids and Lipid Metabolism*, 1086(3):265–272.

[Rust and Donnelly, 2001] Rust, I. W. M. and Donnelly, T. (2001). Particle size determination: An undergraduate lab in Mie scattering. *American Journal of Physics*, 2(69):129–136.

[Sankaran et al., 1999] Sankaran, V., Everett, M. J., Maitland, D. J., Walsh Jr, J. T., et al. (1999). Comparison of polarized-light propagation in biological tissue and phantoms. *Optics Letters*, 24(15):1044–1046.

[Schachter et al., 2000] Schachter, M., Does, M., Anderson, A., and Gore, J. (2000). Measurements of Restricted Diffusion Using an Oscillating Gradient Spin-Echo Sequence. *Journal of Magnetic Resonance*, 147(2):232–237.

[Schmidt et al., 2000] Schmidt, F., Fry, M., Hillman, E., Hebden, J., and Delpy, D. (2000). A 32-channel time-resolved instrument for medical optical tomography. *Review of Scientific Instruments*, 71(1):256–265.

[Schmitt et al., 1992] Schmitt, J., Gandjbakheche, A., and Bonner, F. (1992). Use of polarized light to discriminate short–path photons in a multiply scattering medium. *Applied Optics*, 31(30):6535–6545.

[Schmitt and Kumar, 1998] Schmitt, J. M. and Kumar, G. (1998). Modelling optical properties of soft tissue by fractal distribution of scatterers. *Applied Optics*, 37(13):2788–2797.

[Schuele et al., 2005] Schuele, G., Vitkin, E., Huie, P., O'Connell-Rodwell, C., Palanker, D., and Perelman, L. (2005). Optical spectroscopy noninvasively monitors response of organelles to cellular stress. *Journal of Biomedical Optics*, 10(5):051404/1–051404/8.

[Schweiger et al., 1995] Schweiger, M., Arridge, S., Hiraoka, M., and Delpy, D. (1995). The finite element method for the propagation of light in scattering media: boundary and source conditions. *Medical physics*, 22(11):1779–1792.

[Shemesh et al., 2009] Shemesh, N., Özarslan, E., Basser, P. J., and Cohen, Y. (2009). Measuring small compartmental dimensions with low-q angular double-PGSE NMR: The effect of experimental parameters on signal decay. *Journal of Magnetic Resonance*, 198(1):15–23.

[Shi and King, 2005] Shi, Q. and King, R. W. (2005). Chromosome nondisjunction yields tetraploid rather than aneuploid cells in human cell lines. *Nature*, 437(7061):1038–1042.

[Skaer and Whytock, 1976] Skaer, R. and Whytock, S. (1976). The fixation of nuclei and chromosomes. *Journal of cell science*, 20(1):221–231.

[Sokolov et al., 1999] Sokolov, K., Drezek, R., Gossage, K., and Richards-Kortum, R. (1999). Reflectance spectroscopy with polarized light: is it sensitive to cellular and nuclear morphology. *Optics Express*, 5(13):302–317.

[Spencer, 1982] Spencer, M. (1982). *Fundamentals of light microscopy*. Number 6. CUP Archive.

[Stanisz et al., 1997] Stanisz, G. J., Wright, G. A., Henkelman, R. M., and Szafer, A. (1997). An analytical model of restricted diffusion in bovine optic nerve. *Magnetic Resonance in Medicine*, 37(1):103–111.

[Stejskal and Tanner, 1964] Stejskal, E. and Tanner, J. (1964). Spin Diffusion Measurements: Spin Echoes in the Presence of a Time-Dependent Field Gradient. *The Journal of Chemical Physics*, 42(1):288–292.

[Stepišnik, 1993] Stepišnik, J. (1993). Time-dependent self-diffusion by nmr spin-echo. *Physica B: Condensed Matter*, 183(4):343–350.

[Stewart, 2003] Stewart, G. (2003). The kid haven science library: Microscopes.

[Subramanian et al., 2008] Subramanian, H., Pradhan, P., Liu, Y., Capoglu, I., Li, X., Rogers, J., Heifetz, A., Kunte, D., Roy, H., and Backman, V. (2008). Optical methodology for detecting hisologically unapparent nanoscale consequances of genetic alterations in biological cells. *PNAS*, 105(51):20118–20123.

[Sun et al., 2013] Sun, P., Ma, Y., Liu, W., Xu, C., and Sun, X. (2013). Experimentally determined characteristics of the degree of polarization of backscattered light from polystyrene sphere suspensions. *Journal of Optics*, 15(5):055708.

[Swartz, 1998] Swartz, B. E. (1998). The advantages of digital over analog recording techniques. *Electroencephalography and clinical neurophysiology*, 106(2):113–117.

[Tanner, 1970] Tanner, J. E. (1970). Use of the Stimulated Echo in NMR Diffusion Studies. *The Journal of Chemical Physics*, 5(2):2523–2526.

[Tarvainen, 2006] Tarvainen, T. (2006). *Computational Methods for Light Transport in Optical Tomography*. PhD thesis, University of Kuopio.

[Thormählen et al., 1985] Thormählen, I., Straub, J., and Grigull, U. (1985). Refractive index of water and its dependence on wavelength, temperature, and density. *Journal of physical and chemical reference data*, 14(4):933–945.

[Toublanc, 1996] Toublanc, D. (1996). Henyey–Greenstein and Mie phase functions in Monte Carlo radiative transfer computations. *Applied Optics*, 35(18):3270–3274.

[Vadehra and Nath, 1973] Vadehra, D. and Nath, K. (1973). Eggs as a source of protein. *CRC Critical Reviews in Food Technology*, (4):193–309.

[van Staveren et al., 1991] van Staveren, H., Moes, C., van Marie, J., Prahl, S., and van Gemert, M. (1991). Light scattering in Intralipid-10% in the wavelength range of 400–1100nm. *Applied Optics*, 30(31):4507–4514.

[van Veen et al., 2004] van Veen, R. L., Sterenborg, H., Pifferi, A., Torricelli, A., and Cubeddu, R. (2004). Determination of vis-nir absorption coefficients of mammalian fat, with time-and spatially resolved diffuse reflectance and transmission spectroscopy. In *Biomedical Topical Meeting*, page SF4. Optical Society of America.

[Vanapalli et al., 2002] Vanapalli, S. A., Palanuwech, J., and Coupland, J. N. (2002). Stability of emulsions to dispersed phase crystallization: effect of oil type, dispersed phase volume fraction, and cooling rate. *Colloids and Surfaces A: Physicochemical and Engineering Aspects*, 204(1):227–237.

[Walsh, 2004] Walsh, B. (2004). Markov Chain Monte Carlo and Gibbs Sampling.

[Wang et al., 1995] Wang, L., Jacques, S., and L. Zheng (1995). MCML – Monte Carlo modeling of light transport in multi-layered tissues. *Computer Methods and Programs in Biomedicine*, (47):131–146.

[Wang et al., 2006] Wang, X., Pogue, B. W., Jiang, S., Dehghani, H., Song, X., Srinivasan, S., Brooksby, B. A., Paulsen, K. D., Kogel, C., Poplack, S. P., et al. (2006). Image reconstruction of effective mie scattering parameters of breast tissue in vivo with near-infrared tomography. *Journal of biomedical optics*, 11(4):041106–041106.

[Wang et al., 2005] Wang, X., Pogue, B. W., Jiang, S., Song, X., Paulsen, K. D., Kogel, C., Poplack, S. P., and Wells, W. A. (2005). Approximation

of mie scattering parameters in near-infrared tomography of normal breast tissue in vivo. *Journal of biomedical optics*, 10(5):051704–051704.

[Weber, 2001] Weber, A. L. (2001). History of Head and Neck Radiology: Past, Present, and Future. *Radiology*, (218):15–24.

[Weinberg, 2013] Weinberg, R. (2013). *The biology of cancer*. Garland Science.

[Werring et al., 1999] Werring, D., Clark, C., Barker, G., Thompson, A., and Miller, D. (1999). Diffusion tensor imaging of lesions and normal-appearing white matter in multiple sclerosis. *Neurology*, 52(8).

[Whateley et al., 1984] Whateley, T. L., . Steele, G., Urwin, J., and Smail, G. A. (1984). Particle size stability of intralipid and mixed total parenteral nutrition mixtures. *Journal of Clinical and Hospital Pharmacy*, 12(9):113–126.

[Wiscombe, 1980] Wiscombe, W. (1980). Improved Mie scattering algorithms. *Applied Optics*, 19(9):1505–1509.

[Wittschieber et al., 2010] Wittschieber, D., Köllermann, J., Schlomm, T., Sauter, G., and Erbersdobler, A. (2010). Nuclear grading versus gleason grading in small samples containing prostate cancer: a tissue microarray study. *Pathology & Oncology Research*, 16(4):479–484.

[Wolf and Voshchinnikov, 2004] Wolf, S. and Voshchinnikov, N. (2004). Mie scattering by ensembles of particles with very large size parameters. *Computer Physics Communications*, 162(2):113–123.

[Workman et al., 2010] Workman, P., Aboagye, E., Balkwill, F., Balmain, A., Bruder, G., Chaplin, D., Double, J., Everitt, J., Farningham, D., Glennie, M., et al. (2010). Guidelines for the welfare and use of animals in cancer research. *British journal of cancer*, 102(11):1555–1577.

[Wright et al., 2006] Wright, S., Schweiger, M., and Arridge, S. R. (2006). Reconstruction in optical tomography using the PN approximations. *Measurement Science and Technology*, 18(78):79–86.

[W.S. Price, 1997] W.S. Price (1997). Pulsed-field gradient nuclear magnetic resonance as a tool for studying translational diffusion: Part 1. Basic theory. *Concepts on Magnetic Resonance*, (9):299–336.

[Xu et al., 2009a] Xu, J., Does, M., and Gore, J. (2009a). Quantitative characterization of tissue microstructure with temporal diffusion spectroscopy. *Journal of Magnetic Resonance*, (200):189–197.

[Xu et al., 2009b] Xu, J., Does, M., and Gore, J. (2009b). Sensitivity of MR diffusion measurements to variations in intracellular structure: Effects of nuclear size. *Magnetic Resonance in Medicine*, 61(4):828–833.

[Xu et al., 2006] Xu, M., Alrubaiee, M., and Alfano, R. R. (2006). Fractal Mechanism of Light Scattering for Tissue Optical Biopsy. *Proceeding of SPIE*, 6091.

[Yang and Liou, 1996] Yang, P. and Liou, K. (1996). Finite-difference time domain method for light scattering by small ice crystals in three-dimensional space. *JOSA A*, 13(10):2072–2085.

[Yodh and Chance, 1995] Yodh, A. and Chance, B. (1995). Spectroscopy and imaging with diffusing light. *Physics Today*, 48(3):34–41.

[Zhang et al., 2012] Zhang, H., Schneider, T., Wheeler-Kingshott, C. A., and Alexander, D. C. (2012). Noddi: Practical in vivo neurite orientation dispersion and density imaging of the human brain. *NeuroImage*, 61(4):1000 – 1016.